LUND UNIVERSITY

Transverse Momentum Spectra in pp collisions at $\sqrt{s} = 7$ TeV and $\sqrt{s} = 13$ TeV in ALICE

Andreas Stokkeland

Thesis submitted for the degree of Master of Science
Project duration: 6 months

Supervised by David Silvermyr
Co-supervised by Sumit Basu

Department of Physics
Division of Particle Physics
December 2022

Contents

Abstract

In this project particle production as a function of transverse momentum (p_{T}) in proton-proton collisions at a center-of-mass energy ($\sqrt{s}$) of 7 TeV and 13 TeV has been studied. The transverse momentum is interesting to study since it reflects momentum created in the collision (before the collision, all momentum is in the beam - going in a longitudinal direction) and therefore gives information on the collision dynamics. Firstly, (anti)pions ($\pi^{\pm}$), (anti)kaons ($\mathrm{K}^{\pm}$ and $\mathrm{K}^{0}_{\mathrm{S}}$), (anti)protons ($\mathrm{p}(\bar{\mathrm{p}})$) and (anti)lambdas ($\Lambda^0$ and $\bar{\Lambda}^0$) with their spectra dN/dp_{T} as a function of transverse momentum (p_{T}) were studied. Different functions were fitted to these spectra to see how well they could describe the data. A good fitting function is needed to extrapolate to low p_{T} where the particles can not be measured since they do not have enough momentum to reach the detectors.

To get a measure of how well the fits performed two methods were used. The first was to look at the error relative to the fitting function. The second was to look at minimizing the χ^2/NDF-value where χ^2 can be defined as a statistical measure of how good the fit was and NDF being the Number of Degrees of Freedom.

Secondly, (anti)pions ($\pi^{\pm}$), (anti)kaons ($\mathrm{K}^{\pm}$) and (anti)protons ($\mathrm{p}(\bar{\mathrm{p}})$) where studied in 10 multiplicity classes. Multiplicity is here defined as the number of particles coming out from a collision. From these data, each particle's Minimum Bias (MB) spectrum was created. It was observed that the ratio of the lowest multiplicity class over MB behaved like a e^{-x}-function while the other classes' ratio became a constant for higher p_{T}-values. Thus the lowest multiplicity class was eliminated from a combined fit involving all other classes. Different functions were tested: all with one common parameter and two adjustable parameters for each class.

Finally, so-called Lévy fits were made to each multiplicity class and a Lévy fit to the MB spectrum for each particle. Here, the exponent, $-n$, to the main p_{T}-dependent part of the Lévy function was studied. This function was motivated by the fact that the Lévy function behaves like a power law function, in this case being p_{T}^{n-1}, for high p_{T}. Thus n was the value that determined how fast the spectra went from a region dominated by particles from soft interactions to a phase dominated by particles from jets.

Popular science article

At the CERN Large Hadron Collider (LHC), we try to re-create conditions that are similar to the ones at the beginning of the Universe that we live in. To achieve this, we start by creating small bunches of particles, such as protons or lead ions. These are then accelerated. First linearly and then after they have reached a certain velocity they are put into a system of circular accelerators that takes them on a journey towards higher and higher velocities and therefore energies. These high energies are needed since we aim to de-confine the quarks and gluons in the nucleons that are collided. The state of matter that the ALICE experiments wishes to study is called Quark Gluon Plasma (QGP). This was likely what the Universe consisted of some tiny fraction of a second after its expansion had started.

In this project, we have done two main studies. We started by looking at different fit functions for transverse momentum (p_{T}) spectra. For this part we studied p_{T} spectra for (anti)pions ($\pi\pm$), (anti)kaons ($\mathrm{K}^{\pm}$ and $\mathrm{K}^{0}_{\mathrm{S}}$), (anti)protons ($\mathrm{p}(\bar{\mathrm{p}})$) and the two (anti)lambda particles Λ^0 and $\bar{\Lambda}^0$. We could conclude that the function that could describe the data best was the Lévy function. It is worth noting that this was not the function with the most parameters.

In the second part we studied (anti)pions ($\pi^{\pm}$), (anti)kaons ($\mathrm{K}^{\pm}$) and (anti)protons ($\mathrm{p}(\bar{\mathrm{p}})$) spectra for different multiplicity classes. We did this by looking at the outcomes from many collisions. Some outcomes will have a lot of particles and some will have few. These different outcomes can then be put into different classes. For each particle ((anti)pions, (anti)kaons, and (anti)protons) we had 10 classes. We found that the spectrum for the class with the lowest number of particles was quite different from the other ones and it was therefore eliminated from our next step.

This next step was to make a combined fit for all the classes at once. We did this assuming that there could be a common parameter between the classes. We both used a combined fit and Lévy function fits to help us interpret the spectra dynamics as a function of multiplicity class. Interesting results could be found for both methods.

Acknowledgements

It has been a great privilege to have David Silvermyr as my supervisor. He has always been there when I needed help and gave good feedback. He arranged for me to see CERN and all that was there, and to go to my first conferences, one at CERN and one here in Lund. The conference in Lund was organized by Peter Christiansen, for which I thank him. He should also be thanked due to his vital input to the direction of the project, introducing the multiplicity class over Minimum Bias spectra.

Sumit Basu has been co-supervising during the final stages of the project. He has been helping with navigating the direction of the project and giving useful input, for which I thank him.

I would like to thank Adrian Nassirpour for help during my introduction to the field and Omar Vazquez Rueda for great help with downloading the ROOT [1] and AliRoot [2] programs to first a computer that I borrowed from Lund University. When that did not work we got it to work on my own computer. He has also been a great role model for work ethics. For the technical support and for setting up a desk in the room with the Ph.D. students, I would like to thank Florido Paganelli.

1 Introduction

In the early days of particle physics, in the first half of the 20th century, an important tool to detect particles, often from cosmic radiation was the cloud chamber. Ionizing particles (ionizing radiation) could be observed when they had gone through the chamber. It has presumably always been important for mankind to understand and make sense of our surroundings. Ideas about the smallest parts of what constructs our Universe have probably been around for millennia. From around 500 BCE there have been ideas that could be known about today, in Greece where the term atom was coined, but also in India [3].

The positron, muon, and kaon were first detected using cloud chambers. Carl David Anderson confirmed the existence of the positron in 1932 [4]. An example of a track from a positron can be seen in Fig.1. Later the muon was confirmed to exist by J. C. Street and E. C. Stevenson in 1937 [5]. A decade later, the kaon was confirmed to exist by G. D. Rochester and C. C. Butler in 1947 [6]. This was all to say that the cloud chamber was a good tool for its time but more precise and faster detectors had to be developed to further our knowledge about the smallest parts of our Universe.

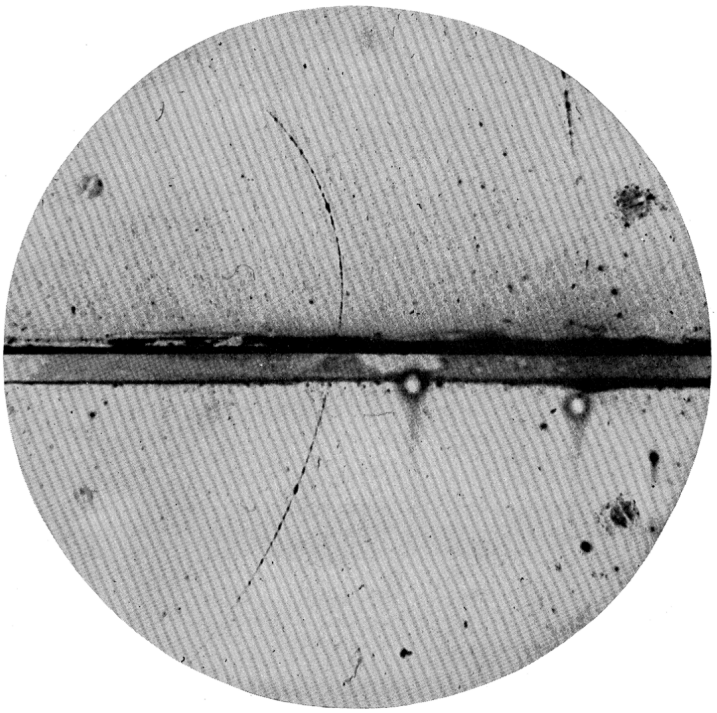

Figure 1: In this figure a track from a positron can be observed. The picture is part of the article that found a particle with the same trajectories as electrons but with the opposite bend, meaning an opposite charge. The object traversing the horizontal diagonal is a lead plate. The lead plate slowed the incoming particle down and thus the particle could be identified. [4]

Today's particle physics needs a far more complex setup of different detectors to do the precise research that is needed. Particle physics has changed from using cosmic radiation a century ago to having particles from collisions with $\sqrt{s} = 13.6$ TeV today at CERN's

Large Hadron Collider (LHC). At LHC there are four main collision points and experiments, and one of them is ALICE. At ALICE there are, among other detector systems, an Inner Tracking System (ITS) detector, a Time Projection Chamber (TPC) detector, and a Time Of Flight (TOF) detector. The ITS is needed for determining the vertex of the collision and to feed tracking data to the TPC which looks at the energy loss of particles and can identify particles by using the Bethe-Bloch formula. The Bethe-Bloch formula has the incoming particle's charge and velocity as the varying input [7]. The velocity can be rewritten like momentum over mass ($v = p/m$). An example of identification by TPC can be seen in Fig.2. The TOF detector is utilized for getting spectra where one can determine the mass of the particles (mass spectrometry) through time measurements. These detectors among others are all there to get a hold of what is going on from the moment the two accelerated bodies hit each other until the resulting particles find the detectors.

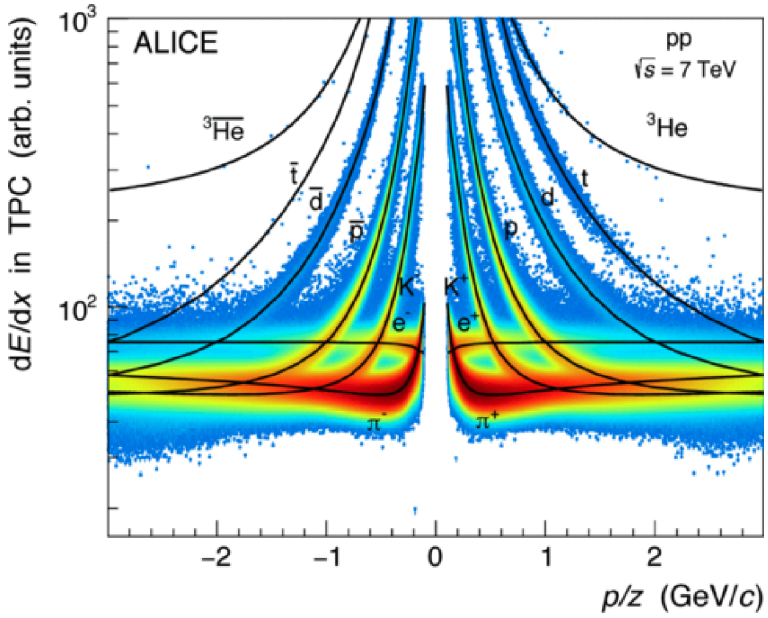

Figure 2: A plot showing the identification of particles through fitting with the Bethe-Bloch formula can be seen. [8]

The first step in this project was to study fit functions to describe transverse momentum (p_{T}) spectra, in section 3.1. Then an analysis of the range of validity for the fits, based on χ^2/NDF was done. χ^2 being a statistical way of describing the agreement between data and fit and NDF being the Number of Degrees of Freedom.

An analysis of different multiplicity classes' spectra in a ratio compared to Minimum Bias (MB) was also performed in section 3, where MB is an average of the p_{T} spectra from each multiplicity class. It was done for (anti)pions ($\pi^{\pm}$), (anti)kaons ($\mathrm{K}^{\pm}$) and (anti)protons ($\mathrm{p}(\bar{\mathrm{p}})$) at two different center-of-mass energies, $\sqrt{s}$ = (7 and 13) TeV. For all histograms, a combined fit was made at once that had a constant for all p_{T} and a part for the low p_{T} that was exponential with the exponent being inversely proportional to the p_{T}, $e^{\alpha \frac{1}{p_{\mathrm{T}}}}$. A test utilizing a Lévy fit function was also made.

2 Theory

In this chapter, the relevant theory behind the ALICE experiment will be presented, starting with the Standard Model in section 2.1. Then in section 2.2 the relativistic kinematics will be defined. After which there will be a section 2.4 about Quark Gluon Plasma (QGP). The next section 2.5 will be about the information on the detectors of the ALICE experiment that will be relevant to this work. Finally, in section 2.6 the fitting functions that were used during this work are defined and described.

2.1 The Standard Model

The Standard Model is a theory that explains all four of the known forces in our Universe except gravity, id est the electromagnetic, weak, and strong interactions. The electromagnetic interaction is mediated by the photon. The weak interaction is mediated by $W^{\pm}$ and Z gauge bosons. Lastly, the strong interaction is mediated by gluons. The particles that mediate these forces are called bosons but in addition to these, there is also the Higgs boson that gives mass to all particles. In addition to the bosons, there are the fermions that are the building blocks of all matter and through the forces interact with each other. Fermions are put into three families starting with the first family having the lowest masses and the third having the highest masses. Each fermion has its own antiparticle which has the same properties, except having the opposite charges and quantum numbers. [9]

In Fig.3, which summarizes the particles in the Standard Model, it can be seen that fermions have half-integer spin and bosons have integer spin. Further, the fermions are divided into two groups, leptons, and quarks. Both leptons and quarks are constituted by three families. As previously described the lowest family has the lowest masses while the second and third have increasing masses when it comes to quarks and leptons except for the neutrinos. Neutrinos are not necessarily massless but it is currently not known what their specific values are. Although there are upper limits for the neutrinos masses that can be seen in Fig.3.

2.2 Relativistic Kinematics

In this section I will shortly introduce the rapidity, y, the pseudo rapidity, η, and the transverse momentum, p_{T}. The rapidity is defined as follows.

$$y = \frac{1}{2} \ln \frac{E + p_z}{E - p_z} \tag{1}$$

where E is the energy and p_z is the momentum along the axis (z) at which the beams are traveling. The rapidity is frequently used since it is Lorentz invariant; it stays the same independently on the inertial frame. There is also the pseudo rapidity which is defined as follows. [11]

$$\eta = -\ln[\tan(\theta/2)] \tag{2}$$

where θ is the angle from the axis where the beams travel. [11]

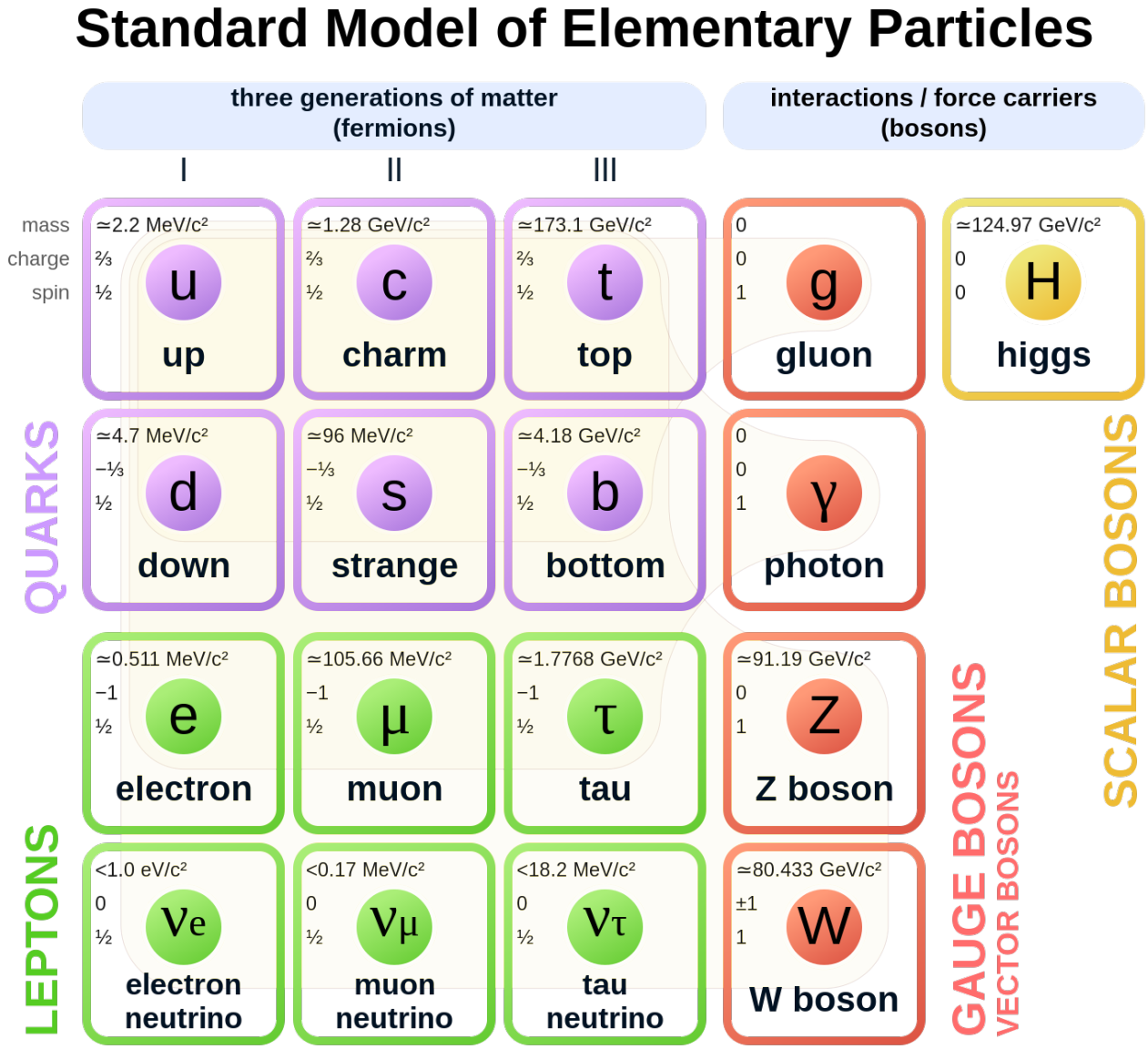

Figure 3: The Standard Model is presented here. Each fermion and boson is shown with their respective mass, charge, and spin. [10]

In a transverse momentum, p_{T}, spectrum there will be p_{T} on the x-axis. Transverse momentum is a parameter that describes the momentum that is created in the plane that is transverse to the axis where the beams before the collision are traveling. Thus it is a momentum that is created in the collision. The transverse momentum, p_{T}, is defined as follows knowing that the momentum that is carried by the colliding particles is (mainly) in the z-axis:

$$p_{\mathrm{T}} = \sqrt{p_x^2 + p_y^2} \tag{3}$$

where p_x and p_y are the momentum component values on the x- and y-axis that span the plane that is transverse to the z-axis. There is also the transverse mass, m_T, which is defined as follows:

$$m_{\mathrm{T}} = \sqrt{m^2 + p_{\mathrm{T}}^2} \tag{4}$$

where m is the mass of the particle and p_{T} is the transverse momentum. [11]

2.3 Chi-squared (χ^2)

The χ^2-value will be defined below in Eq.(5)

$$\chi^2 = \sum_{i=1}^{N} \left[\frac{y_i - F(x_i)}{\sigma_i} \right]^2 \tag{5}$$

where y_i are the data points for each x_i and $F(x_i)$ is the fit function that is tested. σ_i is the uncertainty in the value y_i. χ^2/NDF is used as a criterion of fit quality, where NDF is the Number of Degrees of Freedom. NDF $= N - n$, where N is the number of data points and n is the number of parameters in the fit function. The χ^2/NDF-value is used to measure how good a fit is. Optimally its value should be around 1. For χ^2/NDF > 1 the fit is worse for higher χ^2/NDF-values. For χ^2/NDF < 1 it is only known that the fit is good.

2.4 Quark Gluon Plasma, QGP

When the Universe that we know came to exist at the Big Bang it is expected that the quark-hadron phase transition happened at $\sim$10 μs after the Big Bang [12]. The Quark Gluon Plasma, QGP, is a phase that is expected to be present in high-energy collisions between nuclei with atomic numbers in the range of 10 - 100. For example, one can look at data from Pb-Pb collisions, where Pb has an atomic number of 82. There are also data sets where Cu has been used in collisions with an atomic number of 29. In these nuclear collisions, it is expected that there would be a phase of QGP.

Taking the process step by step from the collision to the freeze-out when the hadrons do not interact with each other anymore, would look something like this; pre-equilibrium of partons – partons being quarks and gluons – then a QGP phase followed by maybe a mixed state between hadrons and partons while the hadronization is in action. Then a state of hadrons (hadronic state) followed by the freeze-out. The hadronic state starts with a chemical freeze-out and stops with a kinetic freeze-out. [13]

One important suggested trait that can be seen when QGP is produced is strangeness enhancement. Strangeness enhancement is the presumption that if QGP has been produced then the resulting particles will have more strange quarks. Meaning that the total number of strange quarks produced from the event will be higher than what it would be if the collision did not produce QGP. [14]

2.5 The ALICE experiment

In ALICE Inner Tracking System (ITS), Time Projection Chamber (TPC), and Time Of Flight (TOF) detectors are used to identify particles. These detector systems can be seen in Fig.4. The overall goal is then to determine the properties of QGP. The ALICE experiment needs particles to collide which are accelerated in different stages. As they enter the stages that contain circular accelerators different magnets are used to steer and focus the bunches of particles that are needed in the collisions. The description of the detector system below refers to how they were when the RUN 2 data, used in this project was collected.

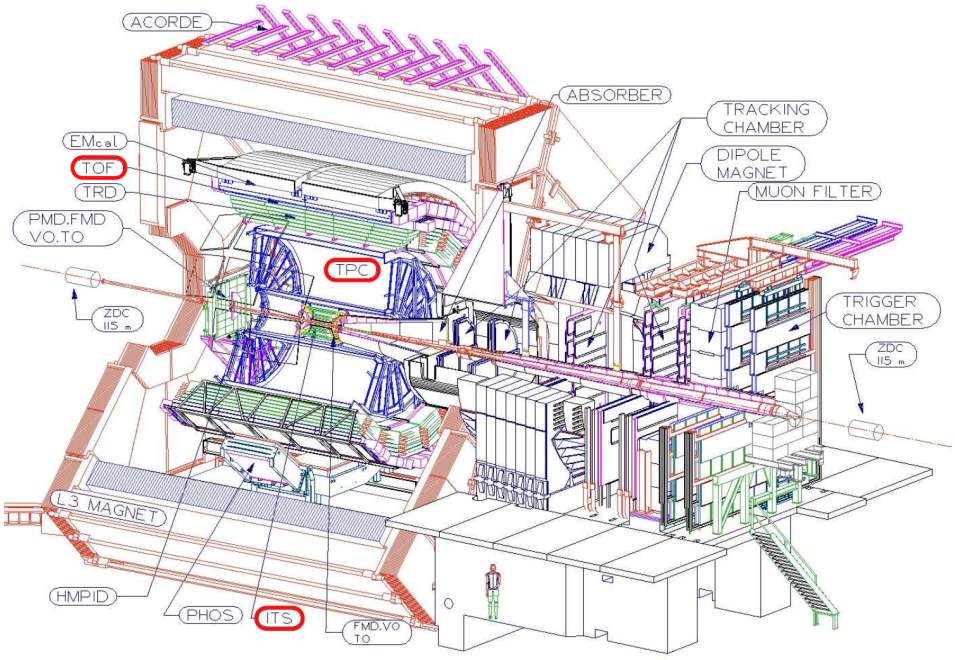

Figure 4: In this figure the ALICE experiment can be seen. The parts relevant to this work are marked around with red. These are the Inner Tracking System (ITS) 2.5.1, the Time Projection Chamber (TPC) 2.5.2, and the Time Of Flight detector (TOF) 2.5.3. [15]

2.5.1 Inner Tracking System (ITS)

The Inner Tracking System (ITS) has 6 layers that are made of silicon detectors. The first is located at a radius of 4 cm and the last one is located at a radius of 43 cm. The detector as a whole cover rapidities of $|\eta| < 0.9$. This is though only for collisions that happen within $\pm$ 5.3 cm from $z = 0$ along the beam axis. The detector layers have spatial resolutions around the order of 10 μm and a relative momentum resolution of 2% for (anti)pions in the range of 100 MeV/c to 3 GeV/c of transverse momentum. [15]

The two innermost layers are Silicon Pixel Detectors (SPD). These are constructed to determine where the vertex is and to detect potential secondary vertices. Here the track density could go up to 50 tracks/cm^2. The two intermediate layers are Silicon Drift Detectors (SDD). Here the charged particle density is expected to be 7 /cm^2. The outer two layers are Silicon Strip Detectors (SSD). These give information to the TPC for the matching of

particles between the two detector systems. It also assembles dE/dx information that is used for low-momentum particle identification. [15]

2.5.2 Time Projection Chamber (TPC)

The Time Projection Chamber (TPC) is designed to handle charged particle multiplicities around $dN/dy = 8000$ and have an energy loss resolution of 5-7 % and to have a spatial resolution of 300 μm in the bend and drift directions respectively.

The shape of the detector is a cylinder. There are four relevant cylinders all with the beamline in their respective centers ($r = 0$). Two of them define where the drift volume is and two of them give electrical insulation to the system. The cylinders that define the drift volume are called inner and outer field cage vessels. These two cylinders are each respectively put at the radius 0.85 m and 2.47 m. Both cylinders have a length along the beam line of 5 m. The two cylinders that provide the insulation are put with a gap of 15 cm to the inner and outer field cage vessel. [16]

The center of the drift volume ($z = 0$) has an electrode (cathode and anode) that is operated with a voltage of 100 kV. This will give a drift field that gives the charged particles a push in the direction of the axis at which the incoming beams are traveling (the z-axis). The drift field is adjusted by using aluminized mylar strips placed for a drift field of 400 V/cm to be provided throughout the hole volume. The drift volume is filled with a Ne-CO_2 gas which for a drift field of 400 V/m has a speed of 2.8 cm/μs which gives a maximum drift time of $\sim$89 μs. [16]

2.5.3 Time Of Flight detector (TOF)

The Time Of Flight detector (TOF) is built up of multigap resistive plate chambers (MRPCs) which have 250 μm gaps with gas in them. The resistive plates are 400 µm thick for the inner plates and 550 µm thick for the outer plates. The resistive plates are made of glass of the same kind that is used in windows, which is also called "soda-lime" glass and the specific spacing between the plates is due to the usage of fishing line [17]. [15]

The setup has an intrinsic time resolution below 40 ps and is nearly fully efficient. Due to the low cost, the detectors can cover the full barrel region and has an area of 140 m^2. The detector can detect (anti)pions and (anti)kaons up to p_T-values around 2.5 GeV/c and p_T-values around 4 GeV/c for (anti)protons. The TOF works with the TPC and ITS for particle identification up to 1 GeV/c. [15]

2.6 Physics motivated fits

This section will describe the utilized fits [18][19]. First, the functions will be defined that have been used here, where p_T is the transverse momentum, Eq.(3). These functions will be fitted to different p_T spectra with the intent of studying the applicability of the fits. The fits are interesting since below some p_T-value the detectors at the ALICE experiment will not be able to detect the particles. For example, a particle with $p_T = 0$ GeV/c will not be able to reach a part of the ALICE detector. Therefore, a way to estimate what is happening in this region of low p_T-values is needed. The solution is to make good fits and to let the fitted

function take values down to $p_{\mathrm{T}} \approx 0$ GeV/c. This could be called yield extrapolation, the act of estimating yields where data is missing. Yield is the number of particles for a specific constraint, say the number of particles between $p_{\mathrm{T}} = (0.1$ and $0.2)$ GeV/c. Below the fit functions will be defined.

- PtExp:

  (See GetPTExpdNdptTimesPt in [19])

$$dN/dp_{\mathrm{T}} = \frac{norm * p_{\mathrm{T}}}{\exp(p_{\mathrm{T}}/T)}\,, \tag{6}$$

in this equation, there is a normalization constant, $norm$, and T which is the inverse slope parameter also called the effective temperature.

- Fermi-Dirac:

  (See GetFermiDiracdNdptTimesPt in [19])

$$dN/dp_{\mathrm{T}} = \frac{norm \cdot p_{\mathrm{T}}}{\exp\left(\sqrt{p_{\mathrm{T}}^2 + m^2}/T\right) + 1}\,, \tag{7}$$

in this equation, there is a normalization constant, $norm$, and T which is the inverse slope parameter also called the effective temperature. There is also m which is the mass of the particle that the p_{T} spectrum that is fitted describe.

- Bose-Einstein:

  (See GetBoseEinsteindNdptTimesPt in [19])

$$dN/dp_{\mathrm{T}} = \frac{norm \cdot p_{\mathrm{T}}}{\exp\left(\sqrt{p_{\mathrm{T}}^2 + m^2}/T\right) - 1}\,, \tag{8}$$

in this equation, the outputs and input are defined the same way as in Eq.(7).

- Boltzmann:

  (See GetBoltzmanndNdptTimesPt in [19])

$$dN/dp_{\mathrm{T}} = \frac{norm * p_{\mathrm{T}} * \sqrt{p_{\mathrm{T}}^2 + m^2}}{\exp\left(\frac{\sqrt{p_{\mathrm{T}}^2+m^2}}{T}\right)}\,, \tag{9}$$

in this equation, the outputs and input are defined the same way as in Eq.(7).

The Boltzmann, Bose-Einstein, Fermi-Dirac, and PtExp functions are all versions of the PtExp function, Eq.(6), which has an exponential part with $-p_{\mathrm{T}}/T$ in the exponent. Meaning that in a logarithmic plot, this function would show as a straight line. In the following equation, Eq.(10), the logarithm of the PtExp function will be shown.

$$\ln(dN/dp_{\mathrm{T}}) = \ln(norm \cdot p_{\mathrm{T}}) - p_{\mathrm{T}}/T\,. \tag{10}$$

Thus the logarithm of the PtExp function, Eq.10, consists of a straight line decreasing for higher p_{T}-values for positive T with a deviation depending on the *norm*-value. The spectra that will be analyzed will have a line-like start and then converge towards $dN/dp_{\mathrm{T}} = 0$ GeV^{-1} for higher p_{T}. Thus for higher p_{T} with a non-zero yield, the fit will not work as well. It can thus be said that the fit works well for low p_{T} (since that is where the fits are started) where the data is mainly from soft collisions.

- BGBW, Boltzmann-Gibbs blast-wave:

  (See GetBGBWdNdptTimesPt in [19] for the coded version used in the fits)

$$\frac{d^2N}{dp_{\mathrm{T}}dy} \mid_{y=0} = D \int_0^{R_0} r dr K_1 \left(\frac{m_T \cosh \rho}{T_{\mathrm{th}}} \right) I_0 \left(\frac{p_{\mathrm{T}} \sinh \rho}{T_{\mathrm{th}}} \right) , \tag{11}$$

where D is a normalization constant, R_0 is the maximum radius of the expanding source (being the QGP) at freeze-out, K_1 and I_0 are Bessel functions, m_T is the transverse mass defined in Eq.(4) and T_{th} is the true freeze-out temperature. $\rho = \tanh^{-1} \beta$ where $\beta = \beta_{\mathrm{s}}(r/R_0)^n$ is the radial flow, β_{s} is the maximum surface velocity, r is the radius and n is a parameter that describes the velocity profile (how β and β_{s} relate to each other). The average transverse velocity is defined as follows:

$$\langle \beta \rangle = \frac{2}{2+n} \beta_{\mathrm{s}} \, . \tag{12}$$

In the referred article, [20], it can be seen that the Boltzmann-Gibbs blast-wave (BGBW) can be used for simulating the QGP. The BGBW fit, Eq.(11), can give the true freeze-out temperature, the effective temperature, and the maximum surface velocity of the QGP together with the parameter n that determines the velocity profile (how β and β_{s} relate to each other) [20]. The BGBW fit has 4 parameters as output and the mass of the particle in question as input. Although the form of the function is not perfectly suited for the full p_{T} spectra, having this many parameters gives it an advantage in describing a larger range of the p_{T} spectra values than the exponential fits.

- Lévy:

  (See GetLevidNdptTimesPt in [19])

$$dN/dp_{\mathrm{T}} = \left[\frac{p_{\mathrm{T}} * \frac{dN}{dy} * (n-1) * (n-2)}{n * T * \{n * T + \mathrm{m} * (n-2)\}} \right] * \left[(1 + (\sqrt{\mathrm{m}^2 + p_{\mathrm{T}}^2} - \mathrm{m})/(n * T)) \right]^{-n} , \tag{13}$$

where dN/dy is a normalization constant that describes the multiplicity of the spectra and y is the rapidity, T is the inverse slope parameter also called the effective temperature, n is a value that determines the tail of the function for high p_{T}-values, $p_{\mathrm{T}} >> m$, and m is the mass of the particle that the p_{T} spectra describes.

This is the last of the fit functions we consider. This function does not have as many parameters as the BGBW function. It has 3 parameters as output and the mass of the particle in question as input. What is so special about the Lévy function is that it behaves like a function proportional to p_{T} for low p_{T} (especially $p_{\mathrm{T}} < m$) and a function proportional to $p_{\mathrm{T}}^{1-\mathrm{n}}$ for higher p_{T}. This gives it an advantage in describing the tail of the p_{T} spectra (high

p_{T}) since that is what the n-value specifically determines. For a mathematical description of the Lévy function see [21].

3 Results and analysis

In this section, results and analysis will be presented together with a background. Firstly it could be noted that C++ coding was used together with the programs ROOT and AliRoot throughout the project. In the beginning, I exercised creating uncorrected transverse momentum spectra from raw data. The results that will be presented here were achieved by using corrected particle spectra that Omar Vazquez Rueda [22] and Oliver Matonoha [23] have been making using data from RUN 2 at $\sqrt{s} = 13$ TeV. These spectra were used for the first part of the work where fits for p_{T} spectra were tested. Examples of these fits can be seen for the p_{T}-exponential fit, Eq.(6), and Lévy fit, Eq.(13), in Fig.6 and Fig.7 respectively. The protons were chosen since they gave the best fit for the p_{T}-exponential function while the p_{T}-exponential fits to other p_{T} spectra included only 3 or 4 bins.

The low part of the p_{T} spectra have particles with low transverse momentum which translates to low transverse velocity. These particles are interesting for Quark Gluon Plasma (QGP) studies, although what we study here are pp collisions. The higher part of the p_{T} spectrum have particles with high transverse momentum (transverse velocity) which are likely from jets. From what can be seen in the spectra the particles with high p_{T} are few and the particles from low p_{T} are many. This is the reason for having longer p_{T}-intervals for the bins in the high p_{T} domain and small p_{T}-intervals for the bins in the low p_{T} domain. To get good statistics a certain number of particles are needed in the chosen interval.

In the Appendix, fits to p_{T} spectra for $\pi^{\pm}$ (6.1), $\mathrm{K}^{\pm}$ (6.2), $\mathrm{K}^{0}_{\mathrm{S}}$ (6.3), $\mathrm{p}(\bar{\mathrm{p}})$ (6.4), Λ^0 (6.5) and $\bar{\Lambda}^0$ (6.6) are shown. For the fits to $\pi^{\pm}$, $\mathrm{K}^{\pm}$ and $\mathrm{p}(\bar{\mathrm{p}})$ there were statistics for p_{T} between (0 and 1) GeV/c. This gave an opportunity to fit below 1 GeV/c which meant that a lower limit was needed. From Omar Vazquez Rueda's Ph.D. thesis we found that 0.3 GeV/c could be used as the lower limit for mesons (in this case $\pi^{\pm}$ and $\mathrm{K}^{\pm}$) and 0.4 GeV/c as the lower limit for baryons (in this case $\mathrm{p}(\bar{\mathrm{p}})$) [22].

For the second part firstly a combined fit for multiple multiplicity over Minimum Bias (MB) spectra was tested. p_{T} spectra were derived from data with multiplicity classes that had invariant yield, $(1/N_{\mathrm{events}}) \cdot (d^2N/dydp_{\mathrm{T}})$, as a function of p_{T}, see Fig.5. From the p_{T} spectra, each with their own multiplicity, each particles' MB spectrum was derived. This was done by summing up the yield for each bin and then dividing by 10, since there were 10 multiplicity classes. The ratio between the multiplicity spectra and their MB spectrum was then analyzed, section 3.2. The data that was used for these histograms were taken from HEPData [24]. The data was from RUN 1 at $\sqrt{s} = 7$ TeV [25][26] and from RUN 2 at $\sqrt{s} = 13$ [27][28] TeV for $\pi^{\pm}$, $\mathrm{K}^{\pm}$, and $\mathrm{p}(\bar{\mathrm{p}})$, see Fig5. The code for both center-of-mass energies, $\sqrt{s}$, concerning fits to multiplicity spectra, MB spectra and fits to their ratios can be found on my GitHub page [29]. For the combined fit the soft, low p_{T}, and hard, high p_{T}, parameters were plotted in Fig.13 using the function $f(p_{\mathrm{T}}) = C_{\mathrm{Hard}} + C_{\mathrm{Soft}} \cdot e^{p_{\mathrm{T}}^{-k}}$. The k-value for each particle divided by their mass has been plotted in Fig.14. The fits to the multiplicity over MB spectra have been plotted in Fig.10, Fig.11, and Fig.12, together with the spectra.

Secondly, Lévy fits for each multiplicity spectrum and for each MB spectrum was made.

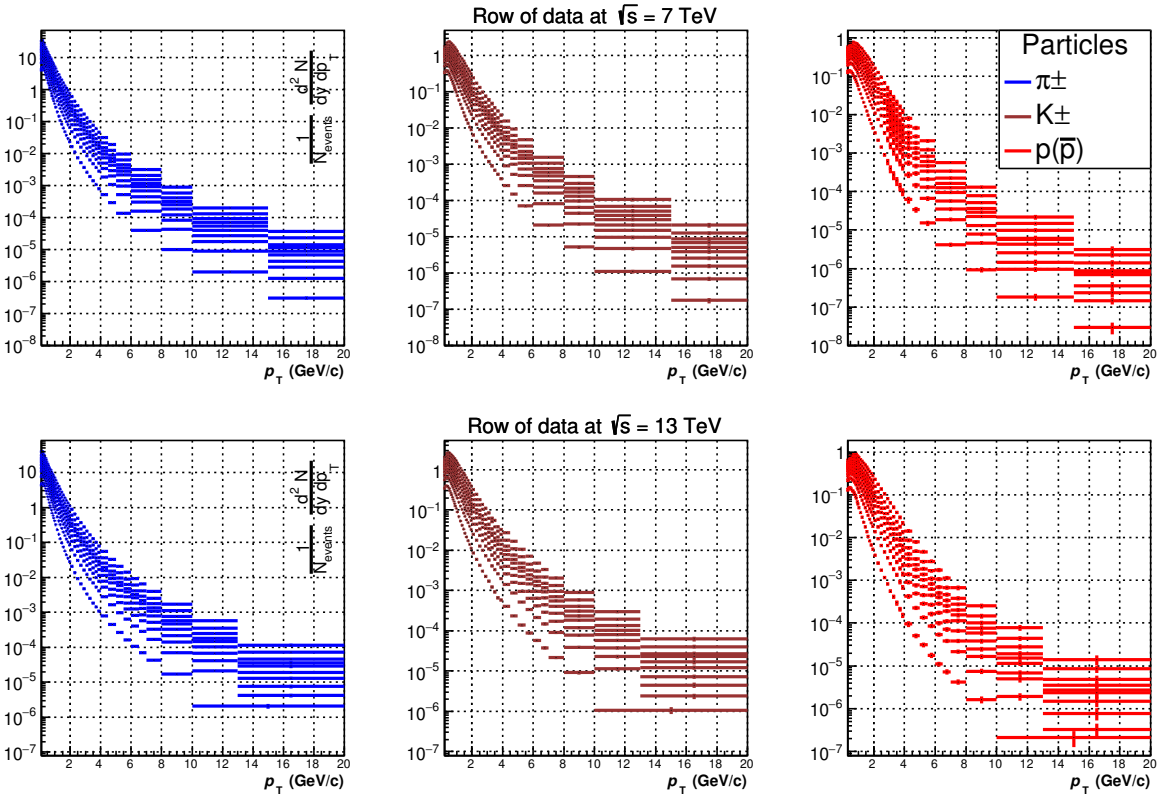

Figure 5: In this figure each multiplicity class for $\pi^{\pm}$, $\mathrm{K}^{\pm}$ and $\mathrm{p}(\bar{\mathrm{p}})$ respectively at $\sqrt{s}$ = (7 (upper row) and 13 (lower row)) TeV can be seen.

The Lévy fit function had a part with the main p_{T} dependency in the base and a unitless value in the exponent, $-n$. This exponent for the multiplicity spectra will be called n1 and the exponent for the fit to the MB spectra will be called n2. The n1- and n2-values will be studied separately in Fig.16 and the (n2 - n1)-values will be studied in Fig.17. The (n2 - n1)-value will be looked at to see that n2 is an average of the n1-values. The ratios between the Lévy fit to the multiplicity class spectrum and the Lévy fit to their MB spectrum have been plotted in Fig.15.

The multiplicity classes that can be seen in Tab.1 were based on the charged particle multiplicity from the event. Where a rapidity range of $|y| < 0.5$ has been used for both center-of-mass energies. More particles are produced at central collisions and less at less central collisions. The total number of particles that comes out from a collision is called multiplicity, N. The number of particles for a specific constraint is called a yield. However, the first section below will describe the multiplicity over Minimum Bias (MB) spectra and start with an analysis of them. Secondly fits to p_{T} spectra was studied, 3.1. The goal was to see which function could describe the p_{T} spectra best. This was done since there was a need to know which fit function could best approximate what happens at very low p_{T}-values since these particles can not reach the detectors. Fits to multiple spectra at once with a common parameter, combined fit, will be presented in section 3.3.

Table showing the multiplicity classes and their $\sigma/\sigma_{\mathrm{INEL}>0}$ and $\langle dN_{\mathrm{ch}}/d\eta\rangle$ for $\sqrt{s}$ = 7 TeV

Multiplicity class	I	II	III	IV	V
$\sigma/\sigma_{\mathrm{INEL}>0}$	(0–0.95) %	(0.95–4.7) %	(4.7–9.5) %	(9.5–14) %	(14–19) %
$\langle dN_{\mathrm{ch}}/d\eta\rangle$	21.3 ± 0.6	16.5 ± 0.5	13.5 ± 0.4	11.5 ± 0.3	10.1 ± 0.3

Multiplicity class	VI	VII	VIII	IX	X
$\sigma/\sigma_{\mathrm{INEL}>0}$	(19–28) %	(28–38) %	(38–48) %	(48–68) %	(68–100) %
$\langle dN_{\mathrm{ch}}/d\eta\rangle$	8.45 ± 0.25	6.72 ± 0.21	5.40 ± 0.17	3.90 ± 0.14	2.26 ± 0.12

Table showing the multiplicity classes and their $\sigma/\sigma_{\mathrm{INEL}>0}$ and $\langle dN_{\mathrm{ch}}/d\eta\rangle$ for $\sqrt{s}$ = 13 TeV

Multiplicity class	I	II	III	IV	V
$\sigma/\sigma_{\mathrm{INEL}>0}$	(0–0.92) %	(0.92–4.6) %	(4.6–9.2) %	(9.2–13.8) %	(13.8–18.4) %
$\langle dN_{\mathrm{ch}}/d\eta\rangle$	26.02 ± 0.35	20.02 ± 0.27	16.17 ± 0.22	13.77 ± 0.19	12.04 ± 0.17

Multiplicity class	VI	VII	VIII	IX	X
$\sigma/\sigma_{\mathrm{INEL}>0}$	(18.4–27.6) %	(27.6–36.8) %	(36.8–46.0) %	(46.0–64.5) %	(64.5–100) %
$\langle dN_{\mathrm{ch}}/d\eta\rangle$	10.02 ± 0.14	7.95 ± 0.11	6.32 ± 0.09	4.50 ± 0.07	2.55 ± 0.04

Table 1: What can be seen in these two tables is that there is a slight difference in the classification, $\sigma/\sigma_{\mathrm{INEL}>0}$, of the multiplicity classes for the different $\sqrt{s}$ energies. $\langle dN_{\mathrm{ch}}/d\eta\rangle$ is the mean charged-particle multiplicity density, simply put a measure of the multiplicity for the events in that class. It can be seen that their values are lower for $\sqrt{s} = 7$ TeV compared to the same values at $\sqrt{s} = 13$ TeV. Meaning that higher available energy, $\sqrt{s}$, for particles to be produced increases the number of particles produced. A rapidity range of $|y| < 0.5$ has been used for both center-of-mass energies. [26] [28]

3.1 The comparison of fits to p_{T} spectra

The process of finding good fits to p_{T} spectra for $\pi^{\pm}$, $\mathrm{K}^{\pm}$, $\mathrm{K}^{0}_{\mathrm{S}}$, $\mathrm{p}(\bar{\mathrm{p}})$, Λ^{0} and $\bar{\Lambda}^{0}$ will be presented here. Examples can be found in Fig.6 and Fig.7 and the rest can be found in the Appendix 6. The fit functions that were used have been defined in the Theory section, 2.6. When the first set of fits had been made the question became: Up to what value is the fit applicable? The first solution was to look at ratio plots where the y-axis had (data−fit)/fit values. From this, it could be determined that the fit for the whole interval was good up to a certain value. 1 on the y-axis was decided to be a reasonable limit for the range of applicability. At this value, the fit was half the data value. Although practical and straightforward, issues could be observed with this approach. Assume that a new limit was put into the fit. Then making a new iteration would produce a new limit. This would be due to the number of bins used in the fit (the amount of data that the fit took into account when producing the fit) being changed. Thus there had to be another way of doing it that might be more complex but could provide a more definite limit that could be used as an input to the fit.

It was established what value could reliably be put as the start of the fit depending on whether it was a meson or baryon from the Ph.D. work done by Omar Vazquez Rueda [22]. Thus these values were used for the start of the fit for $\pi^{\pm}$, $\mathrm{K}^{\pm}$, and $\mathrm{p}(\bar{\mathrm{p}})$. This was due to these spectra being the ones that had transverse momenta below 1 GeV/c. It was then determined that studying χ^2/NDF would be a reasonable way of determining the validity of the fit. χ^2 being defined in Eq.(5) and NDF being Number of Degrees of Freedom. A loop varying the end of the fit that took the χ^2/NDF for each fit was then made. The upper value in the range was determined in such a way that for each iteration the fit got a new bin into the range of the fit. Thus we produced plots with χ^2/NDF on the y-axis and bin numbers on the x-axis, seen in the middle of Fig.6 and Fig.7. In the end, there still had to be a judgment call made to decide where to put the upper limit. Though there was an advantage in knowing that the fit produced the same or equivalent χ^2/NDF. In general, the best description of the data was obtained with the Lévy function.

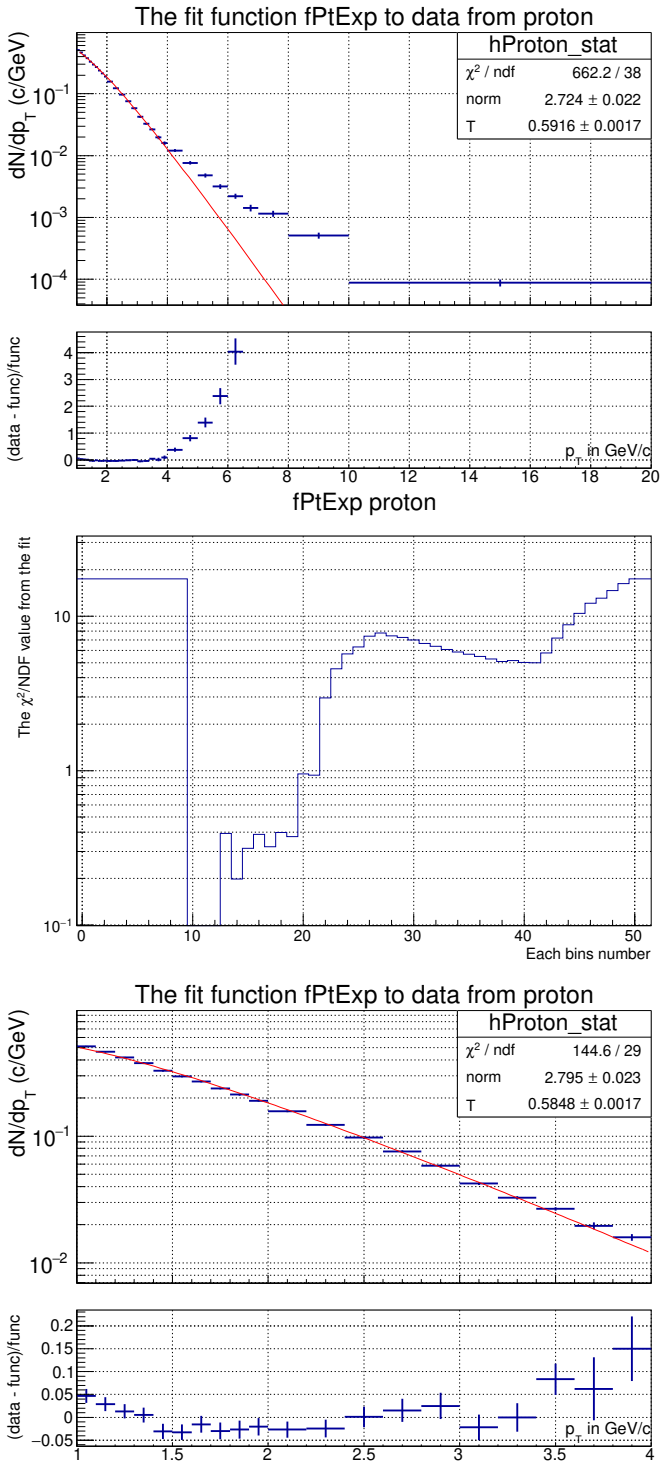

Figure 6: The upper histogram with its p_{T}-exponential fit shows the spectra for the full range. The figure in the middle shows a plot with the number of the upper bin included in a p_{T}-exponential fit, on the x-axis and the χ^2/NDF-value from the p_{T}-exponential fit on the y-axis. The lower histogram shows the histogram for the range in which the fit could be deemed valid from the middle figure.

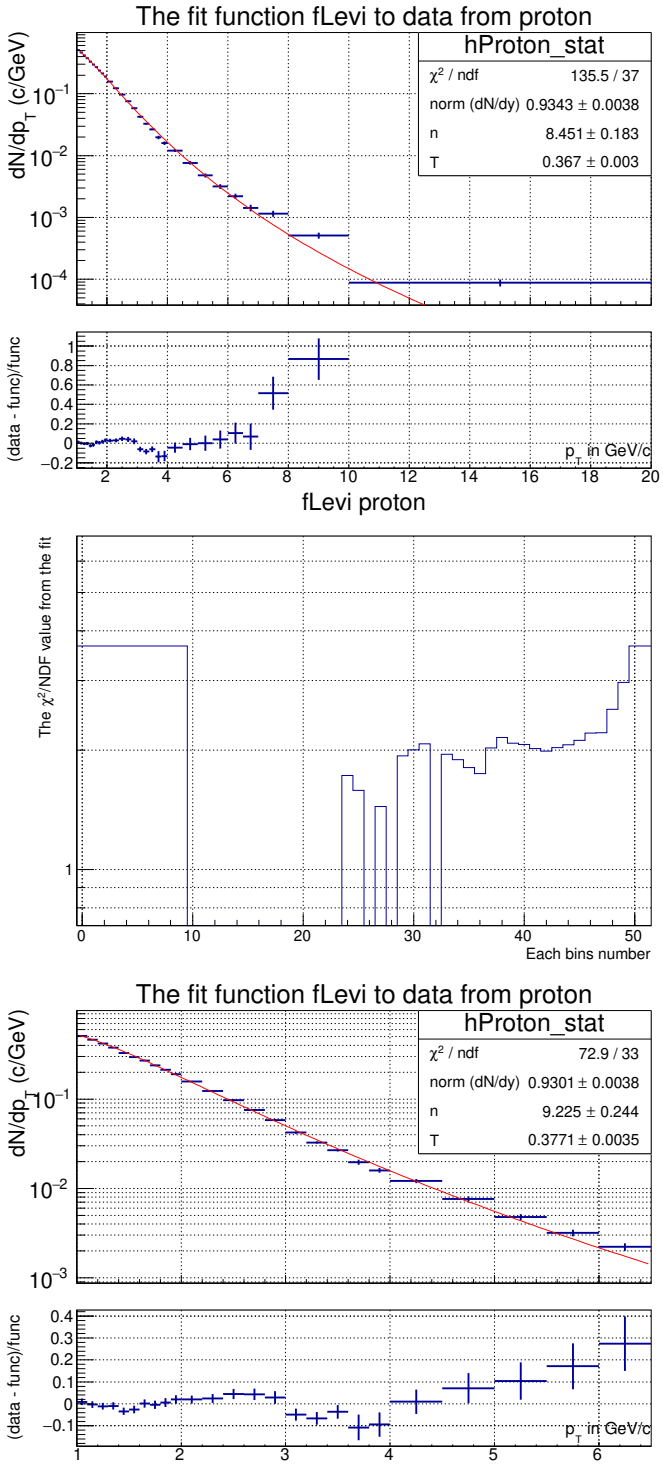

Figure 7: The upper histogram with its Lévy fit shows the spectra for the full range. The figure in the middle shows a plot with the number of the upper bin included in a Lévy fit, on the x-axis and the χ^2/NDF-value from the Lévy fit on the y-axis. The lower histogram shows the histogram for the range in which the fit could be deemed valid from the middle figure.

3.2 Multiplicity class over Minimum Bias (MB) spectra

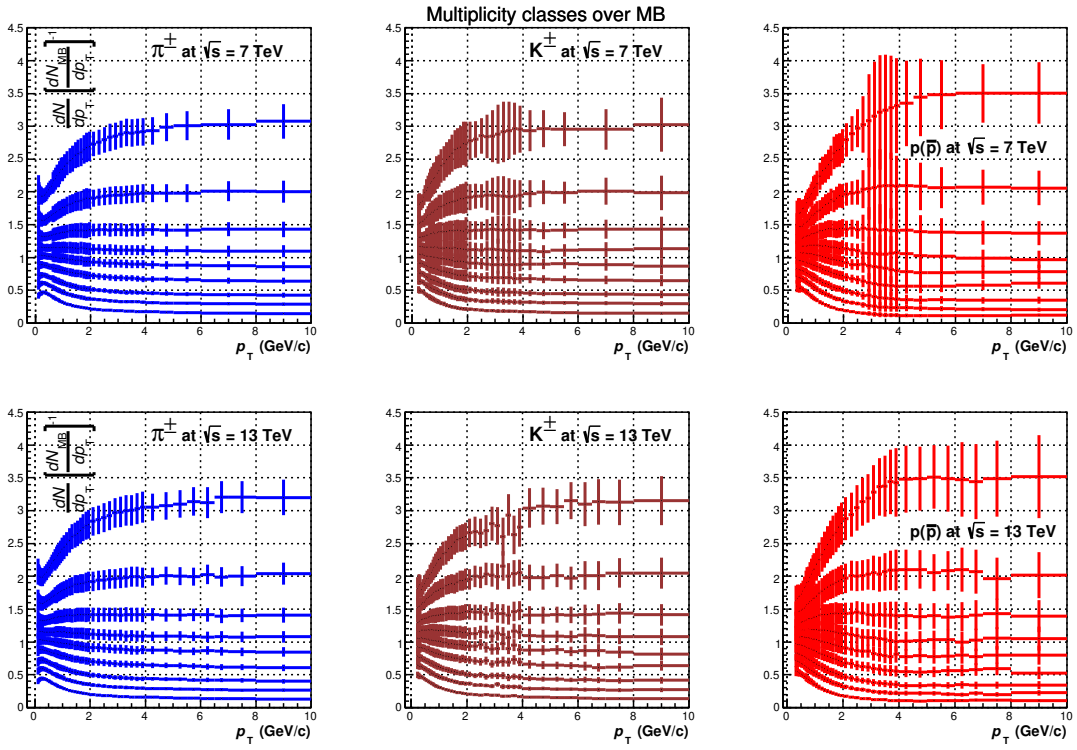

Figure 8: In this figure each multiplicity class over MB spectra is shown for $\pi^{\pm}$, $K^{\pm}$ and p($\bar{p}$) respectively at $\sqrt{s}$ = (7 (upper row) and 13 (lower row)) TeV.

The spectra that were produced through the ratio between multiplicity classes and Minimum Bias (MB) could be observed to be different between the two center-of-mass energies and between the particles. Here follows a description of the spectra that can be seen in Fig.8. Where it will first be noted that all the multiplicity class spectra converged towards the MB for low p_{T}. This suggests a common production mechanism from soft interactions for the low p_{T} region for all multiplicity classes. It could be observed that all multiplicity over MB spectra, except for the lowest multiplicity converged to a constant for high p_{T}. One reason for the highest multiplicity class (with the lowest multiplicity) not to converge would be due to its jet production not being equivalent to the production of jets for other multiplicity classes since the lowest multiplicity is the least central and therefore is not as likely to produce jets. If the p_{T}-spectrum is thought of as a spectrum of velocities then there would be a cut-off at a certain velocity for particles produced by soft interactions. After this limit, mostly jets would be left. What could be seen at $\sqrt{s}$ = (7 and 13) TeV for the (anti)pions and (anti)kaons was that they converge to a constant around 4 GeV/c and for the (anti)protons around 5 GeV/c. If we were to use the language from an expanding Quark Gluon Plasma (QGP) with a certain surface velocity, which may well not be applicable here in the case of pp collisions, this can be translated to velocities through:

$$p_{\mathrm{T}} = \gamma p_0 \,, \tag{14}$$

where p_{T} is the momenta measured by the detector, γ is the gamma factor that for the particles right at the edge of the QGP phase would be a function of β_S being the surface velocity of the QGP phase over the speed of light, c, and p_0 is the momentum carried by the particle. $p_0 = m_0 v$ where m_0 is the rest mass of the particle and at the surface of the QGP phase $v = \beta_S \mathrm{c}$. Thus Eq.14 can be rewritten as follows.

$$p_{\mathrm{T}} = \gamma(\beta) m_0 \mathrm{c}\beta \Longleftrightarrow \beta = \pm \frac{1}{\sqrt{\left(\frac{m_0 \mathrm{c}}{p_{\mathrm{T}}}\right)^2 + 1}} \ . \tag{15}$$

Only positive β_S are of interest. For an (anti)pion ($m_0 \approx 0.1396$ GeV/c^2), $p_{\mathrm{T}} = 4$ GeV/c would correspond to $\beta_S \approx 0.9994$. For an (anti)kaon ($m_0 \approx 0.4937$ GeV/c^2), $p_{\mathrm{T}} = 4$ GeV/c would correspond to $\beta_S \approx 0.9925$. For an (anti)proton ($m_0 \approx 0.9383$ GeV/c^2), $p_{\mathrm{T}} = 5$ GeV/c would correspond to $\beta_S \approx 0.9828$. In this approximate analysis of surface velocities, it could be noted that their values decreased for increasing mass, although if an equal p_{T}-value was to be put into Eq.(15) for each of the particles, a decrease would still be observed due to the masses. For a decrease not to be observed, the p_{T}-value at which the multiplicity over MB spectra converged to a constant for the spectra with lower mass, would have to be scaled with a value above $m_{\mathrm{higher}}/m_{\mathrm{lower}}$. Below a detailed description of the spectra will be found.

For $\sqrt{s} = 7$ TeV the 4 lowest multiplicity classes (with the highest multiplicities) were above the MB. While for $\sqrt{s} = 13$ TeV the 4th lowest multiplicity class was right at or just above the MB. All multiplicity classes over MB ratios started above, at, or below the MB.

For (anti)pions at $\sqrt{s} = 7$ TeV the ratios started at $\sim$0.4 for the 2nd highest multiplicity class and $\sim$2 for the lowest multiplicity class. For (anti)kaons at $\sqrt{s} = 7$ TeV the ratios started at $\sim$0.5 for the 2nd highest multiplicity class and $\sim$1.8 for the lowest multiplicity class. For (anti)protons at $\sqrt{s} = 7$ TeV the ratios started at $\sim$0.6 for the 2nd highest multiplicity class and $\sim$1.6 for the lowest multiplicity class. The histograms then in a region of transverse momenta up to $\sim$4 GeV/c converged to a constant value. For (anti)pions and (anti)kaons at $\sqrt{s} = 7$ TeV the ratios converged to a value of $\sim$0.2 for the 2nd highest multiplicity class and $\sim$3 for the lowest multiplicity class. For (anti)protons at $\sqrt{s} = 7$ TeV the ratios converged to a value of $\sim$0.1 for the 2nd highest multiplicity class and $\sim$3.5 (with error bars spanning between 3 and 4) for the lowest multiplicity class. For (anti)protons at $\sqrt{s} = 7$ TeV the error bars between each multiplicity class were overlapping for bins with transverse momenta between (3 and 4) GeV/c.

For (anti)pions at $\sqrt{s} = 13$ TeV the ratios started at $\sim$0.4 for the 2nd highest multiplicity class and $\sim$2 for the lowest multiplicity class. For (anti)kaons at $\sqrt{s} = 13$ TeV the ratios started at $\sim$0.5 for the 2nd highest multiplicity class and $\sim$1.8 for the lowest multiplicity class. For (anti)protons at $\sqrt{s} = 13$ TeV the ratios started at $\sim$0.6 for the 2nd highest multiplicity class and $\sim$1.6 for the lowest multiplicity class. The histograms then in a region of transverse momenta up to $\sim$4 GeV/c converged to a constant value. For (anti)pions and (anti)kaons at $\sqrt{s} = 13$ TeV the ratios converged to a value of $\sim$0.1 for the 2nd highest multiplicity class and $\sim$3.2 for the lowest multiplicity class. For (anti)protons at $\sqrt{s} = 13$ TeV the ratios converged to a value of $\sim$0.1 for the 2nd highest multiplicity class and $\sim$3.5 (with error bars spanning between 3 and 4, although slightly less than for $\sqrt{s} = 7$ TeV) for the lowest multiplicity class.

3.3 Combined fit and Lévy

A combined fit can be defined as a fit of multiple histograms done at once. In this case, one parameter was constant for all spectra and two parameters were determined for each spectrum. The first step was to make a code that could fit multiple histograms at once. We started with a ROOT example which was originally made for fitting two histograms together. In our case, 10 multiplicity classes' spectra were sought to be fitted. The data for these classes were taken from HEPData, RUN 1 at $\sqrt{s} = 7$ TeV [25][26] and RUN 2 at $\sqrt{s} = 13$ [27][28] TeV for $\pi^{\pm}$, $K^{\pm}$ and $p(\bar{p})$, see Fig.5. The first step was to construct histograms from the data. From there the Minimum Bias (MB) could be constructed. The MB in this case was defined as the histogram that was constructed by summing each bin for all the 10 histograms. For the lowest multiplicity class, there was a different binning between (10 to 20) GeV/c. Thus only transverse momenta going up to 10 GeV/c were analyzed. The bins that were summed up were now divided by 10, the number of multiplicity classes. This was now our MB spectra. Then each multiplicity class was divided by its MB. This then resulted in 10 histograms that if they were summed up would have been a constant value of 10, which divided by the number of multiplicity classes would be 1. This constant 1 could then also be called the MB since a ratio between the MB and itself would be 1.

These ratios between the multiplicity classes and their MB could then be used for the combined fits. The first fit function that was tested was the following.

$$f(p_{\mathrm{T}}) = C_{\mathrm{Hard}} + C_{\mathrm{Soft}} \cdot \mathrm{e}^{k/p_{\mathrm{T}}} \quad , \tag{16}$$

where C_{Hard} is a hard parameter and C_{Soft} is a soft parameter. C_{Hard} and C_{Soft} are varied for each histogram and k is the same for all histograms for a certain particle. An example fit is shown in Fig.9.

It could be seen from Eq.(16) that the parameter k being constant for all multiplicity classes for the same particle had units of GeV/c since this was the unit for p_T used here. C_{Hard} and C_{Soft} were varied for each histogram. First, for the lowest histogram, it was seen that it did not converge to a constant value between transverse momenta of (4 and 10) GeV/c. 10 GeV/c was the upper limit for the used data. The fit functions (including the later ones) were constructed to fit histograms that went out like a constant for p_{T} in that interval. Thus the class with the lowest multiplicity was taken away since it would give parameters that were not relevant.

The fit with Eq.16 provided soft and hard parameters that changed sign after the third highest multiplicity. The full result can be seen in the Appendix section 5. The hard parameters went down for increasing multiplicity classes. The soft parameters went up for increasing multiplicity classes. The results were unstable but values for k could be found where their value over mass decreased for increasing mass. The change between the k/mass-values where the highest for $\sqrt{s} = 7$ TeV. The issue with the other fits were that the k/mass-value for $K^{\pm}$ was lower than the value for $\pi^{\pm}$ and $p(\bar{p})$. In the spectra for $\sqrt{s} = 7$ TeV the fit to the lowest multiplicity class missed the error bars for that histogram for transverse momenta from (2-5) GeV/c to 10 GeV/c for (anti)kaons and (anti)protons. The opposite was observed for $\sqrt{s} =$ 13 TeV.

All the soft and hard parameters here were quite random. If sufficiently few multiplicity classes are studied then a pattern can be seen for that region of multiplicity classes. Therefore

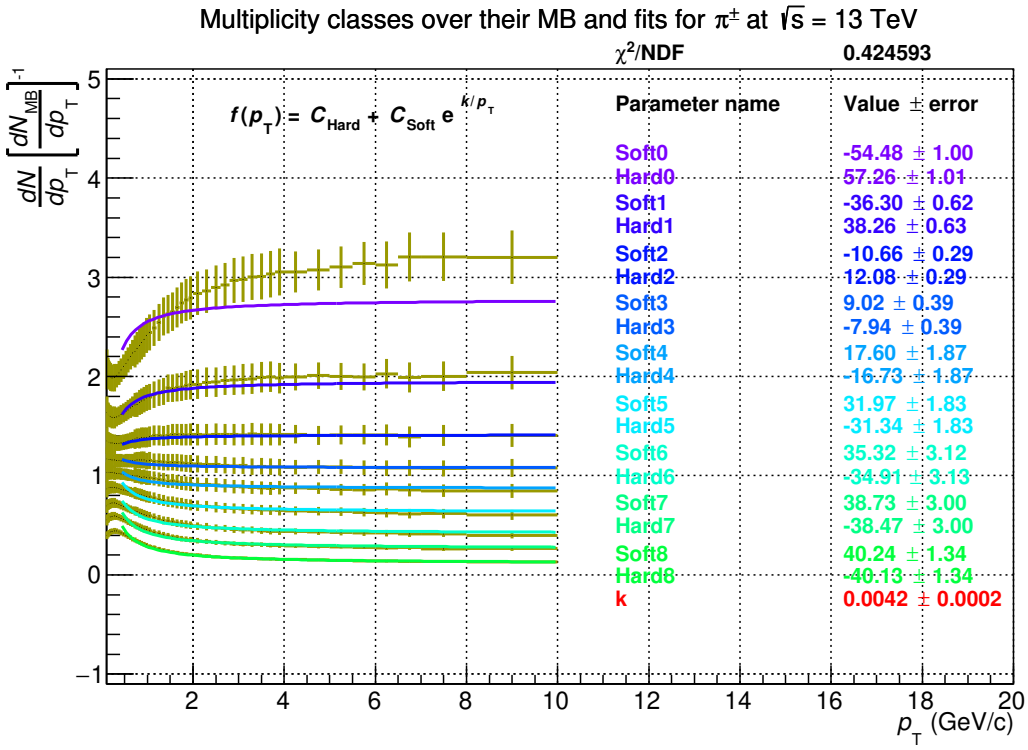

Figure 9: For (anti)pions, $\pi^{\pm}$, at $\sqrt{s} = 13$ TeV the combined fit for all multiplicity classes excluding the lowest multiplicity can be seen in this figure. The function $f(p_{\mathrm{T}}) = C_{\mathrm{Hard}} + C_{\mathrm{Soft}} \cdot \mathrm{e}^{k/p_{\mathrm{T}}}$ was used for these fits.

no overall pattern could be seen. It was good that the k-value could be limited for the k/mass-value to have a linear or exponential dependency on mass. The problem then for this fit was that the soft and hard parameters did not follow any pattern.

Letting the hard part be fitted in a high p_{T} region and the soft part be fitted in a low p_{T} region was studied through the hard parameter being non-zero in the high p_{T} region and the soft parameter being non-zero in the low p_{T} region. This created a function for which the fitter did not know what was happening in the high p_{T} region together with the low p_{T} region. Thus it fitted a constant in the high p_{T} region. The soft part of the function was constructed to converge to 0 for high p_{T} for positive k in Eq.(16). By using a negative soft parameter with a positive k, the fitter could create a soft function that was at the negative part of the y-axis, where there were no bins to fit. The fitter could put k to a negative value which would create a function that starts at the origin and then converge to C_{Soft}. This would work if the ratios started at 0 but since they are ratios relative to MB they start just above, at, and just below 1. The fitter could use a negative soft parameter which would again result in a function on the negative side of the y-axis.

There could be multiple ways of fixing this. One could be to construct a function like the following,

$$f(p_{\mathrm{T}}) = H_{\mathrm{O/I}}(C_{\mathrm{Hard}} - 1) + S_{\mathrm{O/I}}(C_{\mathrm{Soft}} \cdot \mathrm{e}^{k/p_{\mathrm{T}}} + 1) \quad , \tag{17}$$

The k-values and their error for Eq.(18) at $\sqrt{s} = 7$ TeV

Particle	Value	Error
(anti)pion	0.881753	0.0622373
(anti)kaon	1.06985	0.099653
(anti)proton	0.94242	0.0497478

The k-values and their error for Eq.(18) at $\sqrt{s} = 13$ TeV

Particle	Value	Error	$\mathrm{n2}_{\mathrm{max\,or\,min}}$
(anti)pion	0.849036	0.0489723	
(anti)kaon	0.842577	0.0586732	
(anti)proton	0.97959	0.0462442	

Table 2: The k-values from a fit with $f(p_{\mathrm{T}}) = C_{\mathrm{Hard}} + C_{\mathrm{Soft}} \cdot \mathrm{e}^{-(p_{\mathrm{T}})^k}$ are presented here. For $\sqrt{s} = 7$ TeV the values are seemingly random while for $\sqrt{s} = 13$ TeV the values for (anti)pions and (anti)kaons are equivalent and the value for (anti)protons is slightly higher.

where C_{Hard}, C_{Soft}, and k are defined as in (16). $H_{\mathrm{O/I}}$ and $S_{\mathrm{O/I}}$ would turn on and off the two parts of the function in different regions. For this solution, k would have to be negative. In the end, further studying this was not pursued since the fit functions were working sufficiently.

The following function that we tried gave great fits and interesting parameters and is therefore discussed further below:

$$f(p_{\mathrm{T}}) = C_{\mathrm{Hard}} + C_{\mathrm{Soft}} \cdot \mathrm{e}^{-(p_{\mathrm{T}})^k} \quad , \tag{18}$$

where C_{Hard} is a hard parameter and C_{Soft} is a soft parameter, both being untiless. C_{Hard} and C_{Soft} are varied for each histogram and k is constant for all histograms for a certain particle. The results are shown in figures 10-14. For this function, good fits were provided. It could be noted that, unless the p_T-value was to be divided by a constant that was defined to be 1 GeV/c there would be a weird unit on k. Therefore the plots of k/mass did not have an explicit unit on the y-axis.

The ratios and their fit can be found in Fig.10, Fig.11 and Fig.12. The soft and hard parameters from these fits can be found in Fig.13. The constant k-value can be found in Fig.14, where since the x-axis does not have a scale, the values have been divided by their mass.

At $\sqrt{s} = 7$ TeV the fits for (anti)pions and (anti)kaons were right at the values of the multiplicity class over MB spectra for all p_{T}. At $\sqrt{s} = 7$ TeV the fit for (anti)protons for high p_{T} at the lowest multiplicity class (with the highest multiplicity) was at the bottom of the error bars, for the rest of the multiplicity classes the fits were varying within the errors of the values. At $\sqrt{s} = 7$ TeV the fit for (anti)protons for low p_{T} was mostly right at the values.

At $\sqrt{s} = 13$ TeV the fits for all particles and all multiplicities were right at the values for all p_{T}. Except for a few particles and multiplicities for which there was a p_{T} region where the fit deviated from the data by approximately half the error.

Let us discuss the result seen in Fig.13. For both center-of-mass energies all the hard parameters were positive and decreasing for increasing multiplicity classes and ranged from

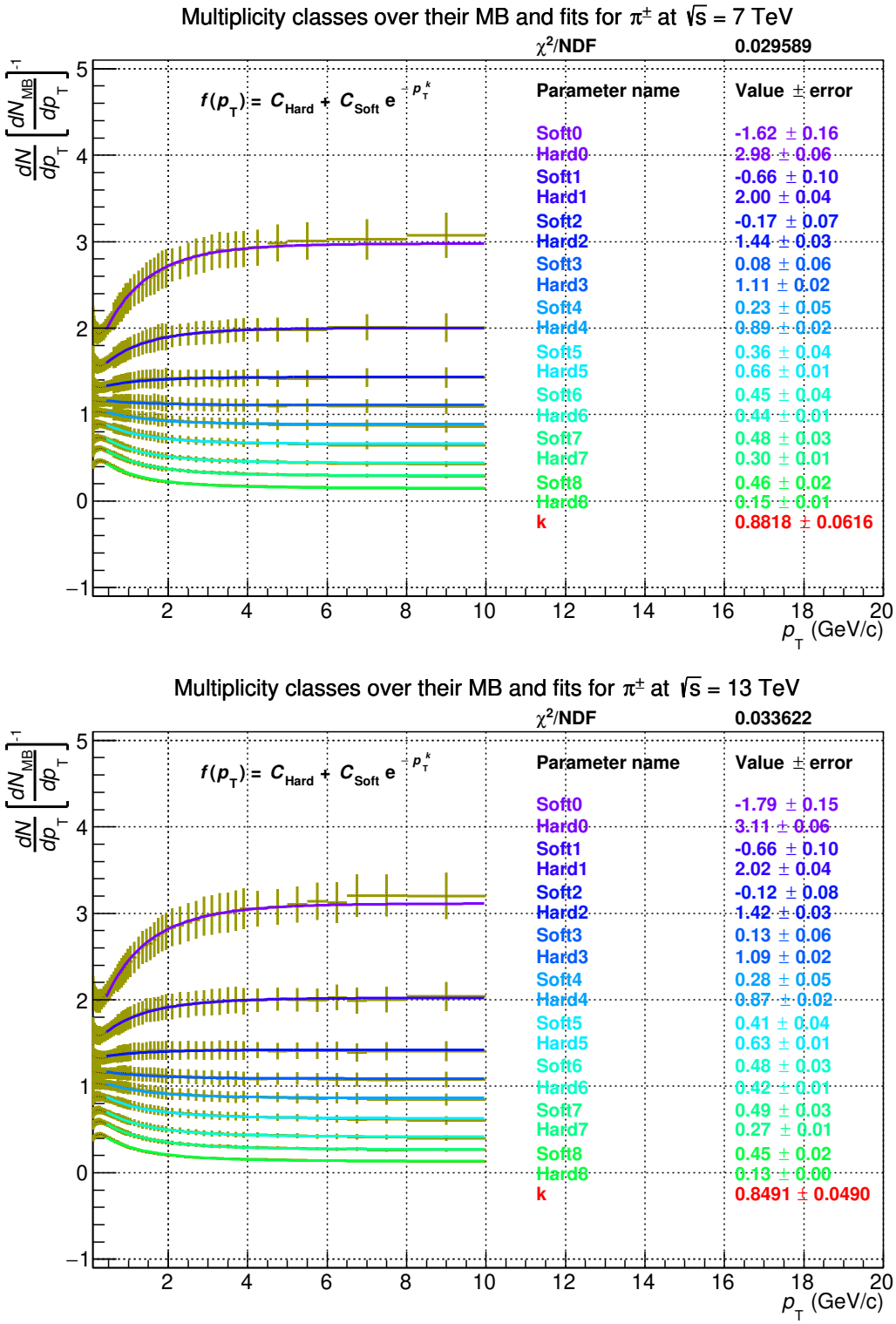

Figure 10: For (anti)pions, $\pi^{\pm}$, at $\sqrt{s}$ = (7 (upper) and 13 (lower)) TeV the combined fit for all multiplicity classes excluding the lowest multiplicity can be seen in this figure. The function $f(p_{\mathrm{T}}) = C_{\mathrm{Hard}} + C_{\mathrm{Soft}} \cdot \mathrm{e}^{-p_{\mathrm{T}}^{k}}$ was used for these fits.

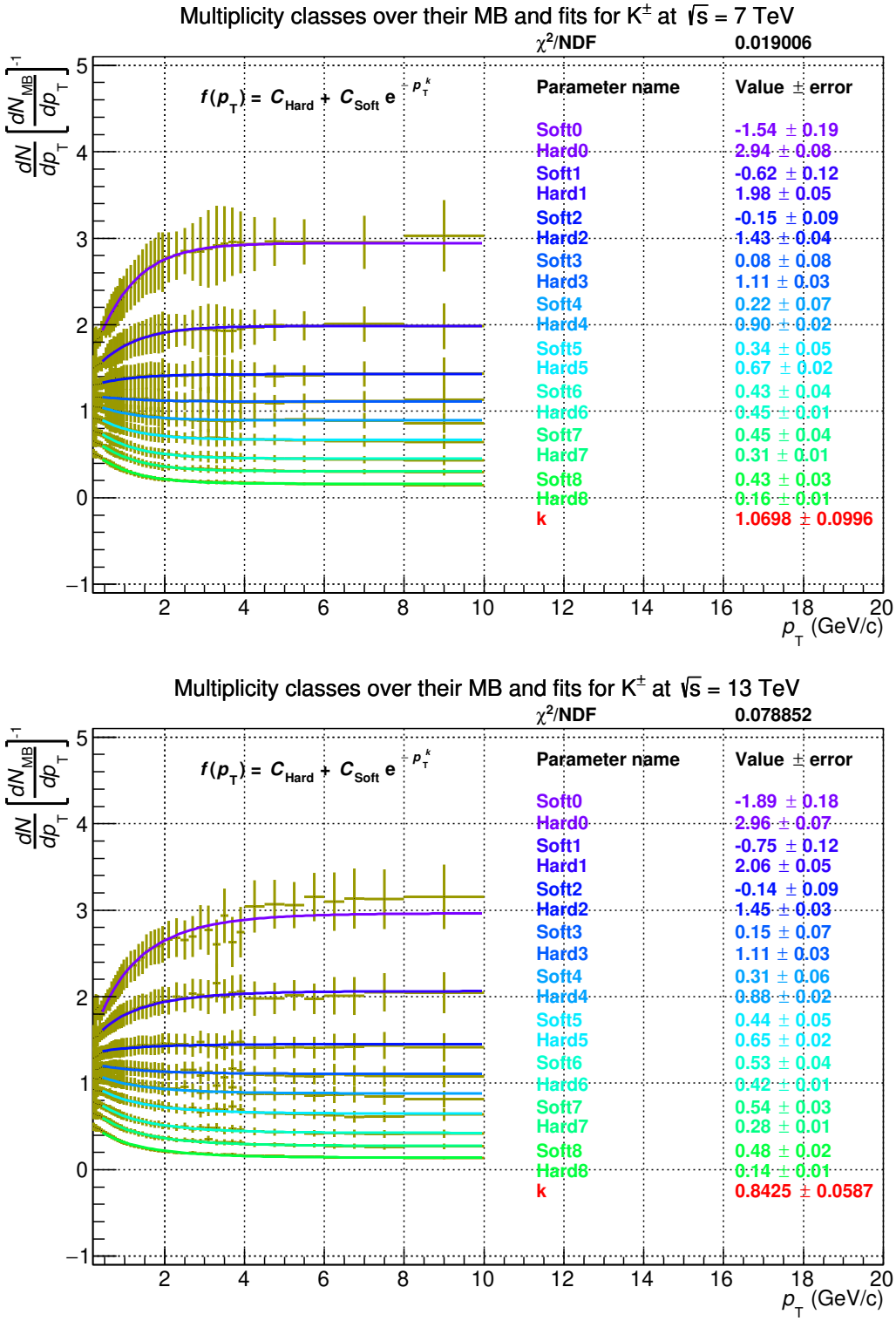

Figure 11: For (anti)kaons, $\mathrm{K}^{\pm}$, at $\sqrt{s}$ = (7 (upper) and 13 (lower)) TeV the combined fit for all multiplicity classes excluding the lowest multiplicity can be seen in this figure. The function $f(p_{\mathrm{T}}) = C_{\mathrm{Hard}} + C_{\mathrm{Soft}} \cdot \mathrm{e}^{-p_{\mathrm{T}}^{k}}$ was used for these fits.

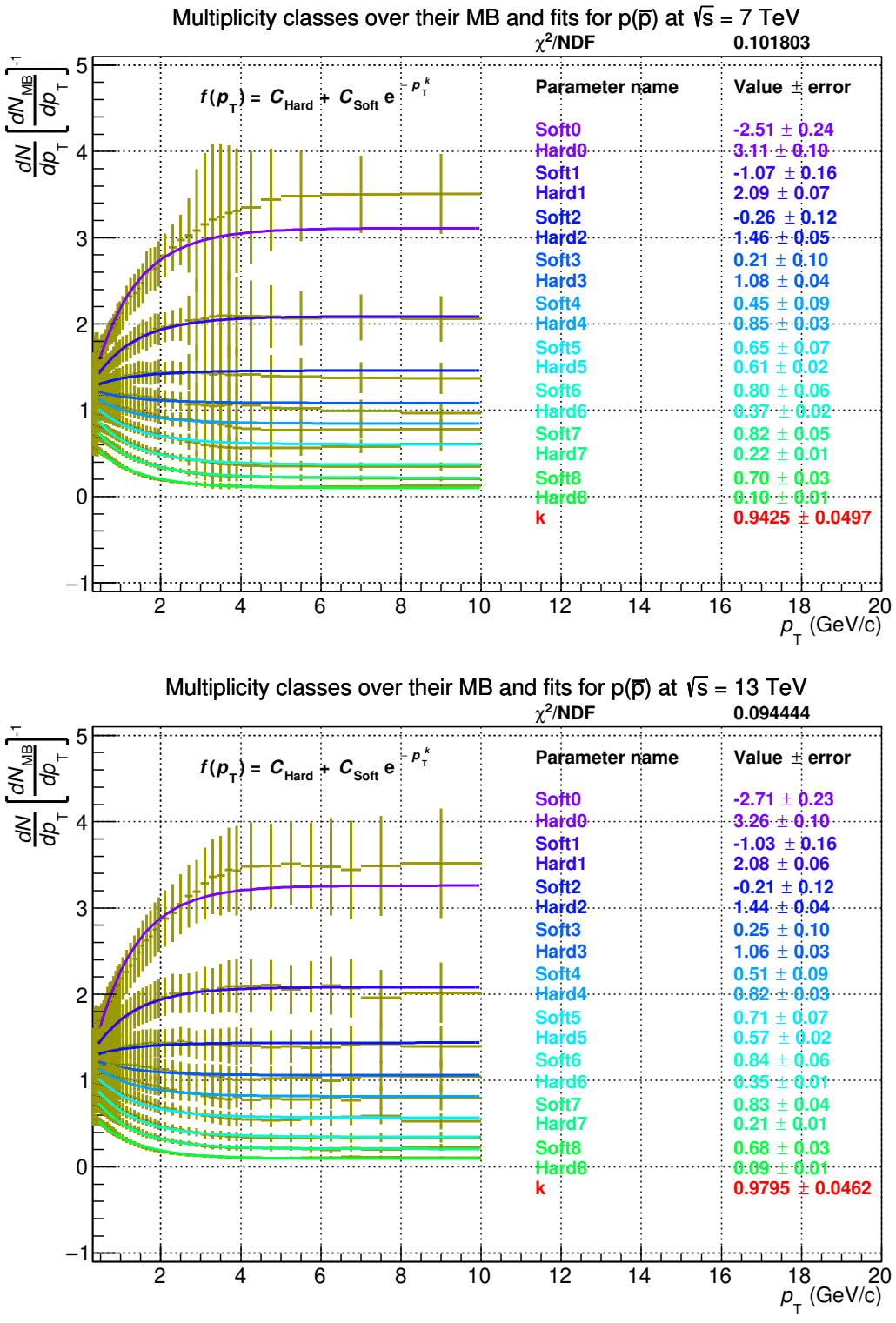

Figure 12: For (anti)protons, p($\bar{\text{p}}$), at $\sqrt{s}$ = (7 (upper) and 13 (lower)) TeV the combined fit for all multiplicity classes excluding the lowest multiplicity can be seen in this figure. The function $f(p_{\text{T}}) = C_{\text{Hard}} + C_{\text{Soft}} \cdot \text{e}^{-p_{\text{T}}^{k}}$ was used for these fits.

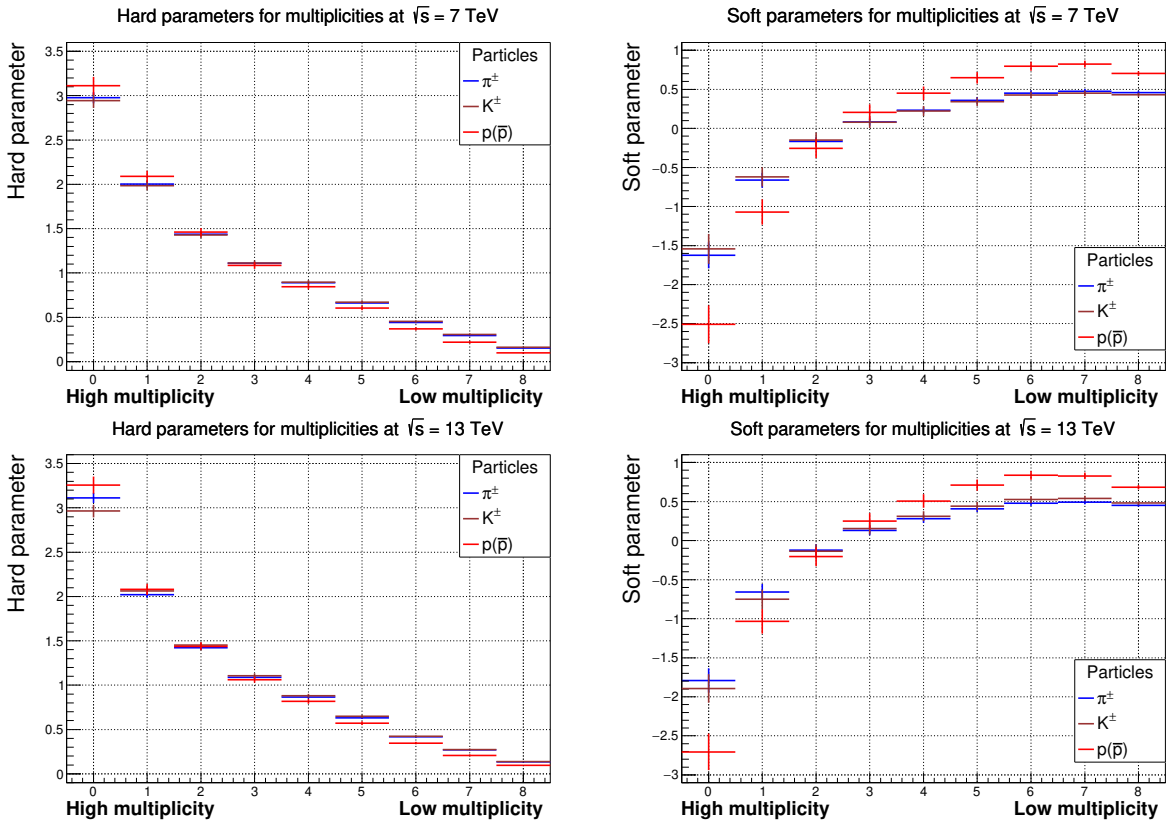

Figure 13: In the left column of figures the hard parameters for each multiplicity class and how their values fall towards higher multiplicity classes (with lower multiplicities) can be seen. In the right column of figures, the soft parameters for each multiplicity class and how their values increase towards higher multiplicity classes can be seen. Both of the figures in the upper row are from data at $\sqrt{s} = 7$ TeV and both of the figures in the lower row are from data at $\sqrt{s} = 13$ TeV.

$\sim$0.1 to $\sim$3.4. At $\sqrt{s} = 7$ TeV for the 3 lowest multiplicity classes the hard parameter for (anti)protons had the highest value followed by the (anti)pion and then the (anti)kaon. At $\sqrt{s}$ = 7 TeV for the 4th and higher multiplicity classes the (anti)kaons' hard parameter was the highest followed by (anti)pions and then (anti)protons. At $\sqrt{s} = 7$ TeV the hard parameters were overlapping a lot except for (anti)protons at the 6th lowest and higher multiplicity classes.

At $\sqrt{s} = 13$ TeV for the 3 lowest multiplicity classes the hard parameter for (anti)protons, (anti)pions, and (anti)kaon followed each other in all possible combinations. At $\sqrt{s} = 13$ TeV, like for $\sqrt{s} = 7$ TeV, for the 4th and higher multiplicity classes the (anti)kaons' hard parameter was the highest followed by (anti)pions and then (anti)protons. At $\sqrt{s} = 13$ TeV the hard parameters were overlapping a lot except for (anti)protons at the 4th lowest and higher multiplicity classes and (anti)kaons, which had the lowest hard parameter, at the lowest multiplicity class.

At $\sqrt{s} = 7$ TeV the soft parameters had a maximum at the 8th lowest multiplicity class. At $\sqrt{s} = 13$ TeV the soft parameters for (anti)pions and (anti)kaons had a maximum at the

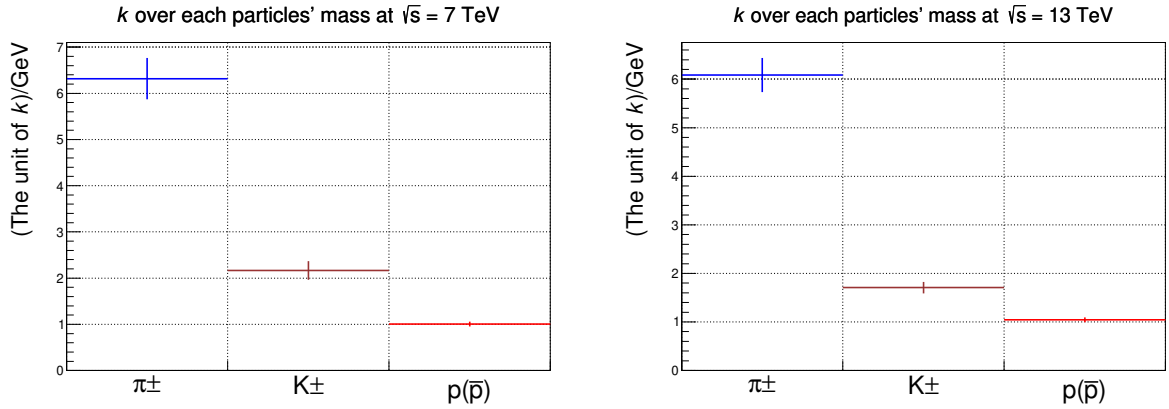

Figure 14: In these two figures the k-value for each particle ($\pi^{\pm}$, $K^{\pm}$ and $p(\bar{p})$) over their respective masses at $\sqrt{s}$ = (7 (left) and 13 (right)) TeV. It can be seen that there is a decreasing trend for the k/mass-value as the particles' masses increase. The k-values on there own can be seen in Tab.2.

8th lowest multiplicity class while the soft parameters for (anti)protons had a maximum at the 7th lowest multiplicity class. This is maybe not a significant difference since it could be noted that for both center-of-mass energies and all the particles the error bars were overlapping for the 7th and 8th lowest multiplicity class. For both center-of-mass energies, the soft parameter for (anti)pions and (anti)kaons were overlapping for all multiplicity classes while the soft parameters for (anti)protons were overlapping with the others only for the 3rd and 4th highest multiplicity. For both center-of-mass energies and all particles the soft parameters changed sign after the third lowest multiplicity class. For both center-of-mass energies and for all multiplicity classes the (anti)kaons' soft parameters were closest to 0, the second closest were the (anti)pions' soft parameters and then the (anti)protons were the furthest away.

When k was limited to be between 0.1 and 5, fits could be found for which the k/mass-values went down for increasing mass. For (anti)pions the k/mass-value was higher at $\sqrt{s}$ = 7 TeV than at $\sqrt{s}$ = 13 TeV, although they were overlapping. For (anti)kaons the k/mass-value was higher at $\sqrt{s}$ = 7 TeV than at $\sqrt{s}$ = 13 TeV by a factor ∼1.4. For (anti)protons the k/mass-value was lower at $\sqrt{s}$ = 7 TeV than at $\sqrt{s}$ = 13 TeV, although they were overlapping.

It was interesting to see that the k-value could be limited for the k/mass-value to have a linear or exponential dependency on mass. We could also observe that the soft and hard parameters followed some patterns. The problem with the soft and hard parameters were that they did not follow patterns that were dependent on mass. It could be observed that the soft parameters for (anti)pions and (anti)kaons are around half the value for (anti)protons. If we were to study more particles we could perhaps tell if this difference is partially from baryon (3 quarks) vs meson (quark + anti-quark) differences. The soft parameter in itself determines how fast the spectra should converge to the region dominated by particles from jets. In that process, the soft parameters are dependent on the value of k which adjusts the function in the low p_{T} domain. The hard parameters could likely have a good correlation to the values at which the spectra converged for high p_{T}.

It was found in an earlier section 3.1 that the Lévy fit was the optimal fitting function of the functions that we explored. Therefore a Lévy fit to each multiplicity spectrum and their MB spectrum was made. The ratio between the fit to each multiplicity spectrum over the fit to the MB spectrum was defined. This ratio was then compared to the corresponding multiplicity over MB data in Fig.15 for $\pi^{\pm}$, $K^{\pm}$, and $p(\bar{p})$. The exponent to the main p_T dependent part for the fit to multiplicity classes will be called n1. The exponent to the main p_T dependent part for the fit to the MB will be called n2. n determines how fast the Lévy function converges to $\sim$0 for $p_T > m$, m being the mass of the particle. Higher n gives a faster conversion.

It could be observed that the n1-values did not change sign, were positive and had a straight linear correlation to the multiplicity classes, see Fig.16. The n1-values had decreasing values for decreasing multiplicities. The n1-values were generally higher for $\sqrt{s} = 13$ TeV. The n2/mass-values decreased for increasing mass, Fig.16. The n2/mass-values did not change significantly between $\sqrt{s} =$ (7 and 13) TeV. The n2/mass-values from a fit can be seen in Tab.3.

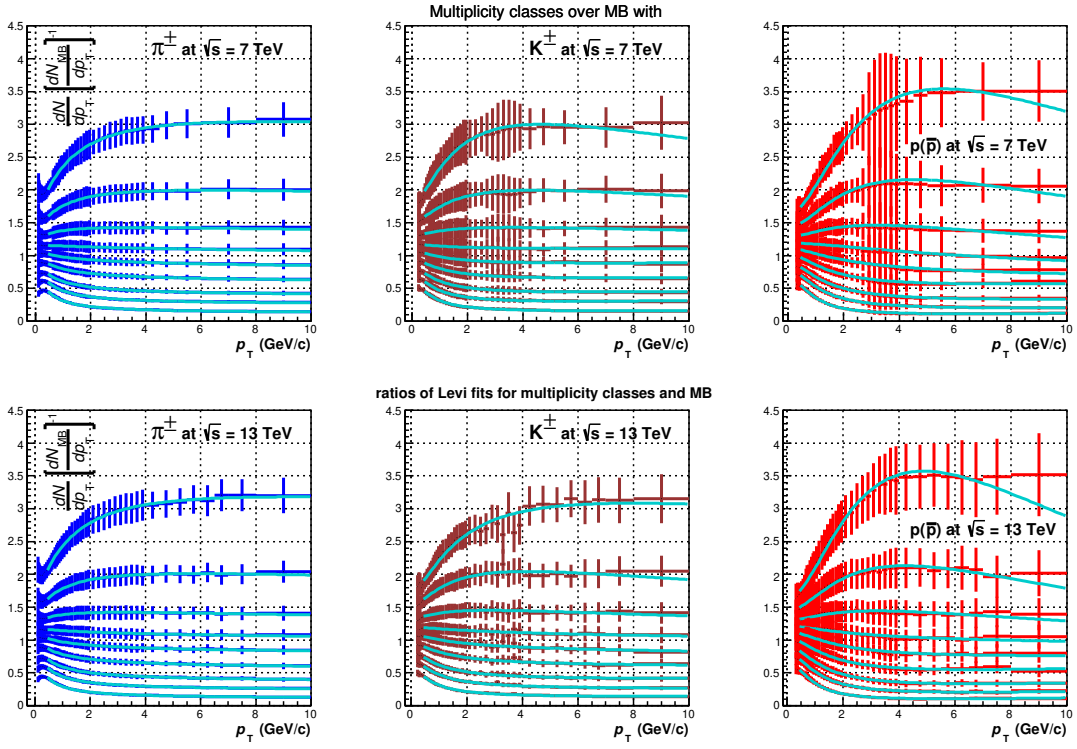

Figure 15: For $\pi^{\pm}$, $K^{\pm}$, and $p(\bar{p})$ (from left to right) at $\sqrt{s} =$ (7 (upper) and 13 (lower)) TeV the Levi fits for each multiplicity class excluding the highest multiplicity class (with the lowest multiplicity) over the Levi fit for the MB together with their corresponding histogram can be seen in this figure.

For (anti)pions and (anti)kaons, it could be observed for both center-of-mass energies respectively that their n2-values were approximately equal. This would mean that they both converged to $\sim$0 at equal speeds. Although the convergence to $\sim$0 is rather the convergence to the part of the spectra where jets dominate. Thus it is how fast the spectra converge from

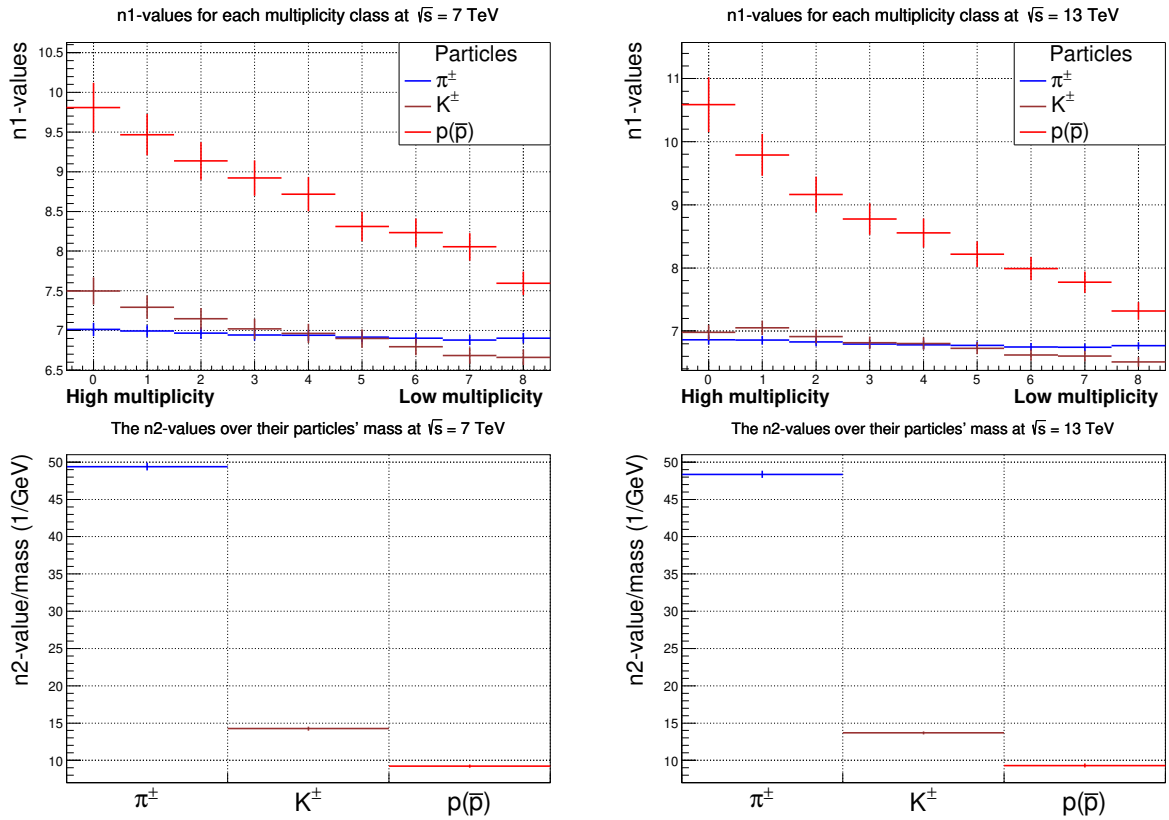

Figure 16: In the upper row of figures the n1 value for each multiplicity class and how their values fall towards lower multiplicity classes can be seen. In the lower row of figures the n2 value can be seen (coming from the fit to the MB) over the mass for each of the particles: $\pi^{\pm}$, $K^{\pm}$, and $p(\bar{p})$ at $\sqrt{s}$ = (7 (left column) and 13 (right column)) TeV. It could be seen for the (anti)pions' n1-values that the lowest bin and the highest bin had overlapping error bars for both energies. For the two energies it is not clear if their n2-values overlap for each particle. Thus for a fit n2-values are presented in Tab.3.

being dominated by particles produced from soft interactions to being dominated by particles from jets. The (anti)protons n2-values for both center-of-mass energies were significantly higher, and thus their spectra converged to the part of the spectrum dominated by jets fastest. For (anti)pions the n1-values went down for increasing multiplicity classes although their error bars were overlapping. Therefore it could be that their spectra converged faster in the region dominated by jets or it could be that they all equally converged in that region. Between (anti)pions and (anti)kaons it could be observed only for the two highest and the 2nd and 3rd lowest multiplicities that their soft parameters were separate at $\sqrt{s} = 7$ TeV. While at $\sqrt{s} = 13$ TeV the (anti)pions' and (anti)kaons' were separate at the 2nd highest and 2nd lowest multiplicity.

Through the understanding that the Lévy fit was working another function was tested for the combined fit, presented below.

$$f(p_{\mathrm{T}}) = C_{\mathrm{Hard}} + C_{\mathrm{Soft}} \cdot p_{\mathrm{T}}^{-k} \quad , \tag{19}$$

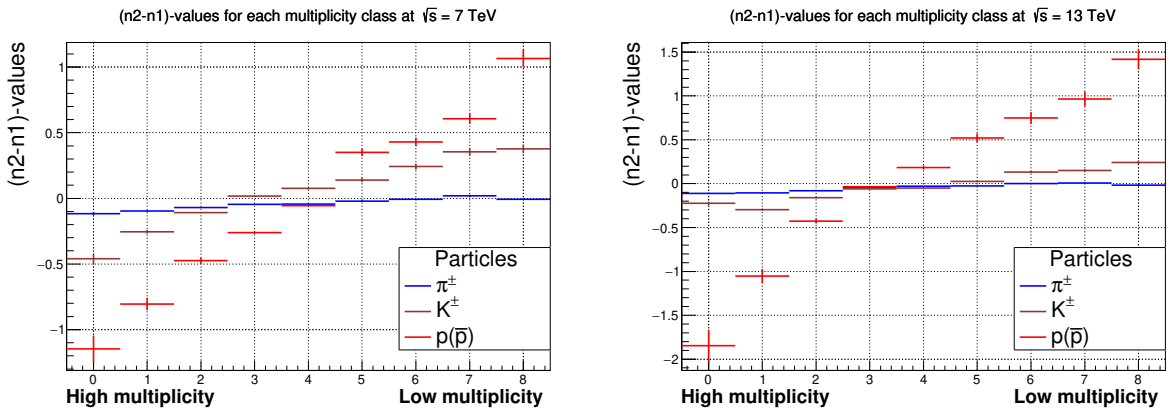

Figure 17: The (n1 - n2)-value for each multiplicity class at $\sqrt{s} =$ (7 (left) and 13 (right)) TeV can be seen in these two figures. This value is important since a Levi fit for each multiplicity class over a Levi fit for the MB will be made. This will result in a function where the part that has the main dependency on p_{T} will have this value as its exponent.

where C_{Hard} and C_{Soft} are varied for each histogram and k is the same for all histograms for a certain particle. The results are shown in figures 18-22. This function was tested since p_{T}^{-k} is a power law and the Lévy function also behaves like a power law for high p_{T}, $p_{\mathrm{T}} > m$. A close to equal analysis could be made for these fits as the one for Eq.18. Although for this fit it was not equally clear that the (anti)protons' soft parameters had twice the values that the (anti)pions and (anti)kaons had. At both center-of-mass energies, the (anti)protons' hard parameter changed sign for the 2nd highest multiplicity class (with the 2nd lowest multiplicity).

The n2-values and their error at $\sqrt{s} = 7$ TeV

Particle	Value	Error	$n2_{\text{max or min}}$
(anti)pion	6.89638	0.0726514	$n2_{min} \approx 6.82373$
(anti)kaon	6.66087	0.0994362	$n2_{max} \approx 6.76031$
(anti)proton	8.66068	0.212894	$n2_{max} \approx 8.87357$

The n2-values and their error at $\sqrt{s} = 13$ TeV

Particle	Value	Error	$n2_{\text{max or min}}$
(anti)pion	6.75034	0.0669974	$n2_{max} \approx 6.81734$
(anti)kaon	6.75384	0.102037	$n2_{min} \approx 6.65180$
(anti)proton	8.73898	0.253617	$n2_{min} \approx 8.48536$

Table 3: The n2-values from a fit are presented here. For the (anti)pions in this case the values are sufficiently far away from each other. Although the difference is in the order of 10^{-3} compared to the value at 10^{0}. For the (anti)kaons and (anti)protons, the values are overlapping.

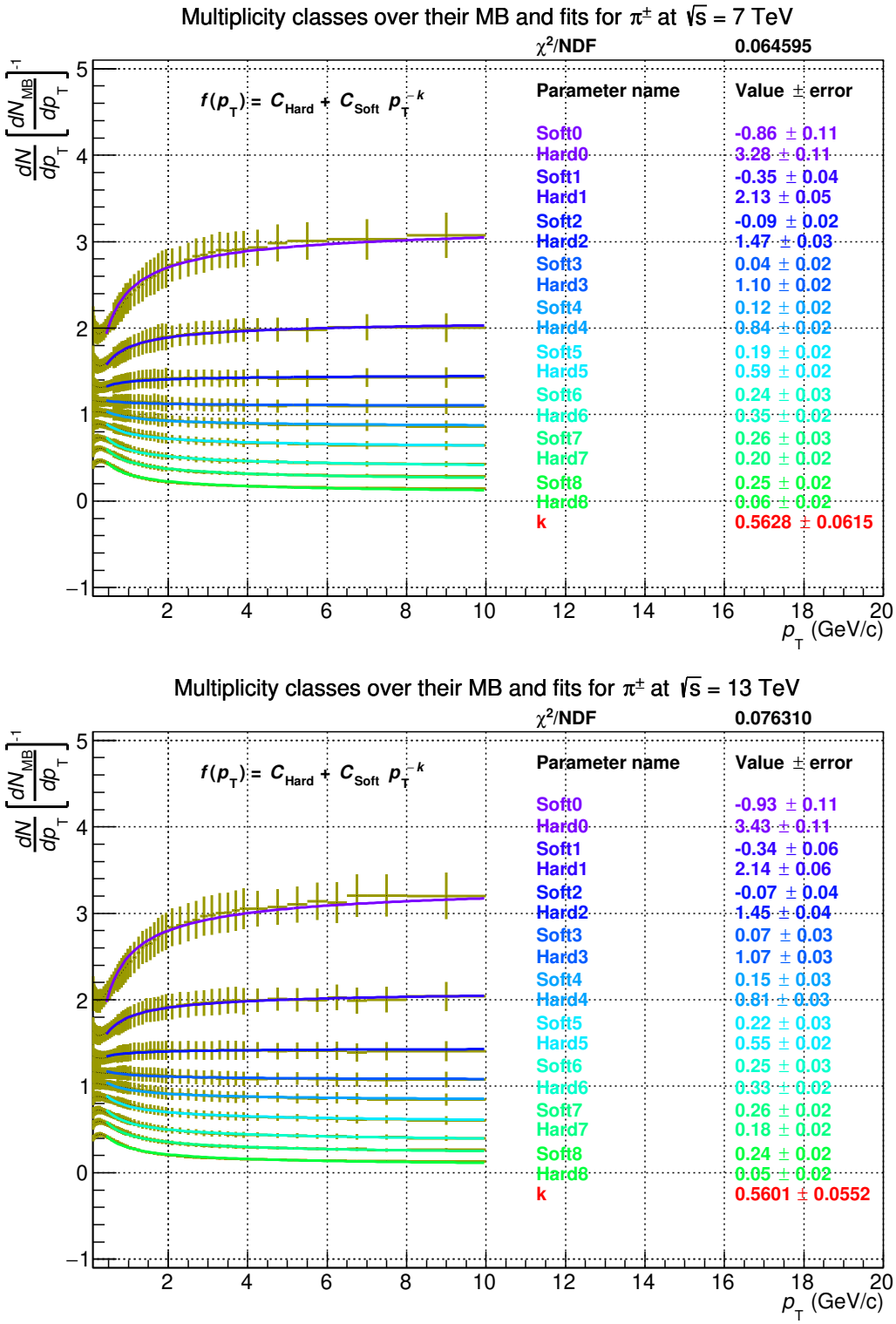

Figure 18: For (anti)pions, $\pi^{\pm}$, at $\sqrt{s}$ = (7 (upper) and 13 (lower)) TeV the combined fit for all multiplicity classes excluding the lowest multiplicity can be seen in this figure. The function $f(p_{\mathrm{T}}) = C_{\mathrm{Hard}} + C_{\mathrm{Soft}} \cdot p_{\mathrm{T}}^{-k}$ was used for these fits.

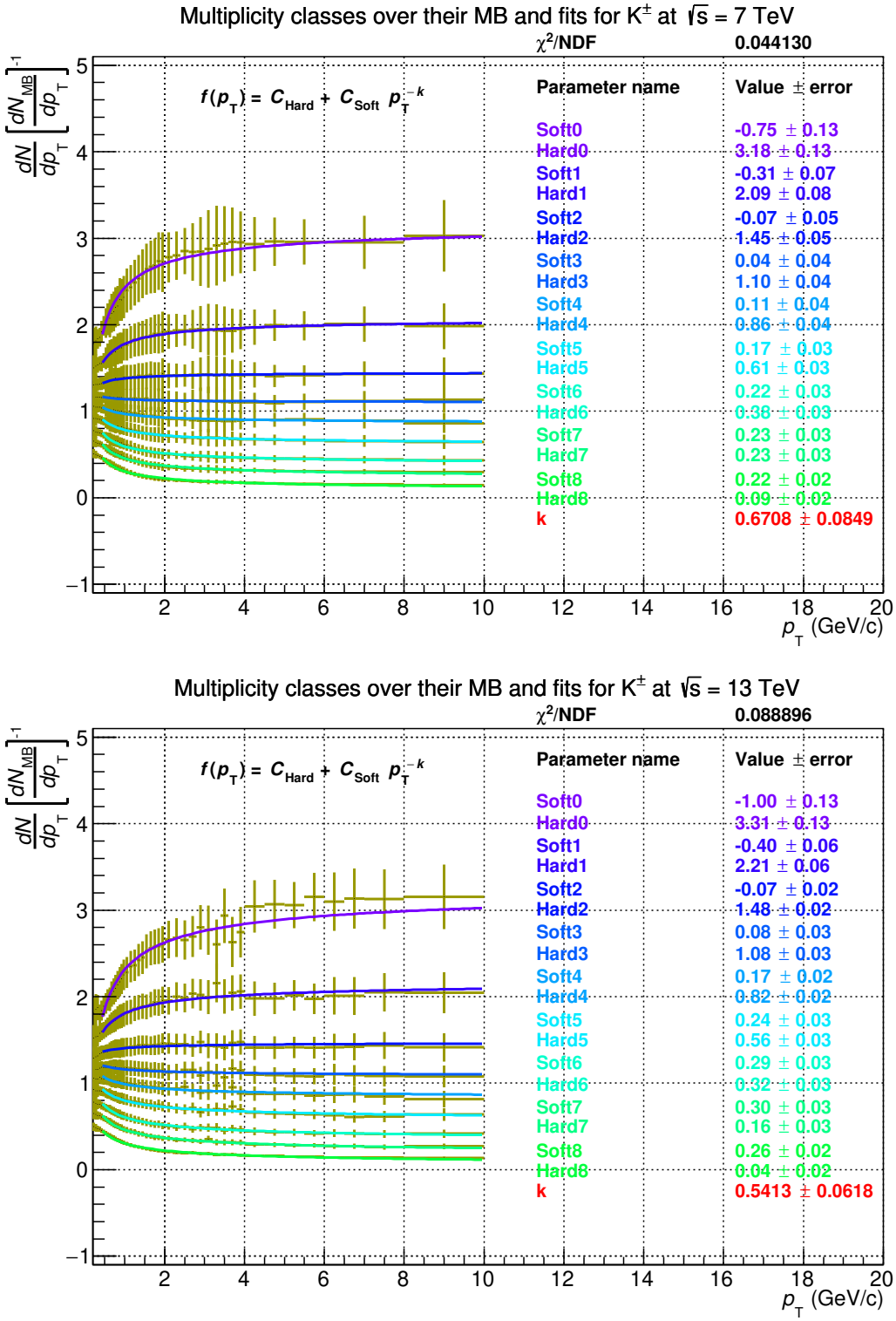

Figure 19: For (anti)kaons, $K^{\pm}$, at $\sqrt{s}$ = (7 (upper) and 13 (lower)) TeV the combined fit for all multiplicity classes excluding the lowest multiplicity can be seen in this figure. The function $f(p_T) = C_{\mathrm{Hard}} + C_{\mathrm{Soft}} \cdot p_T^{-k}$ was used for these fits.

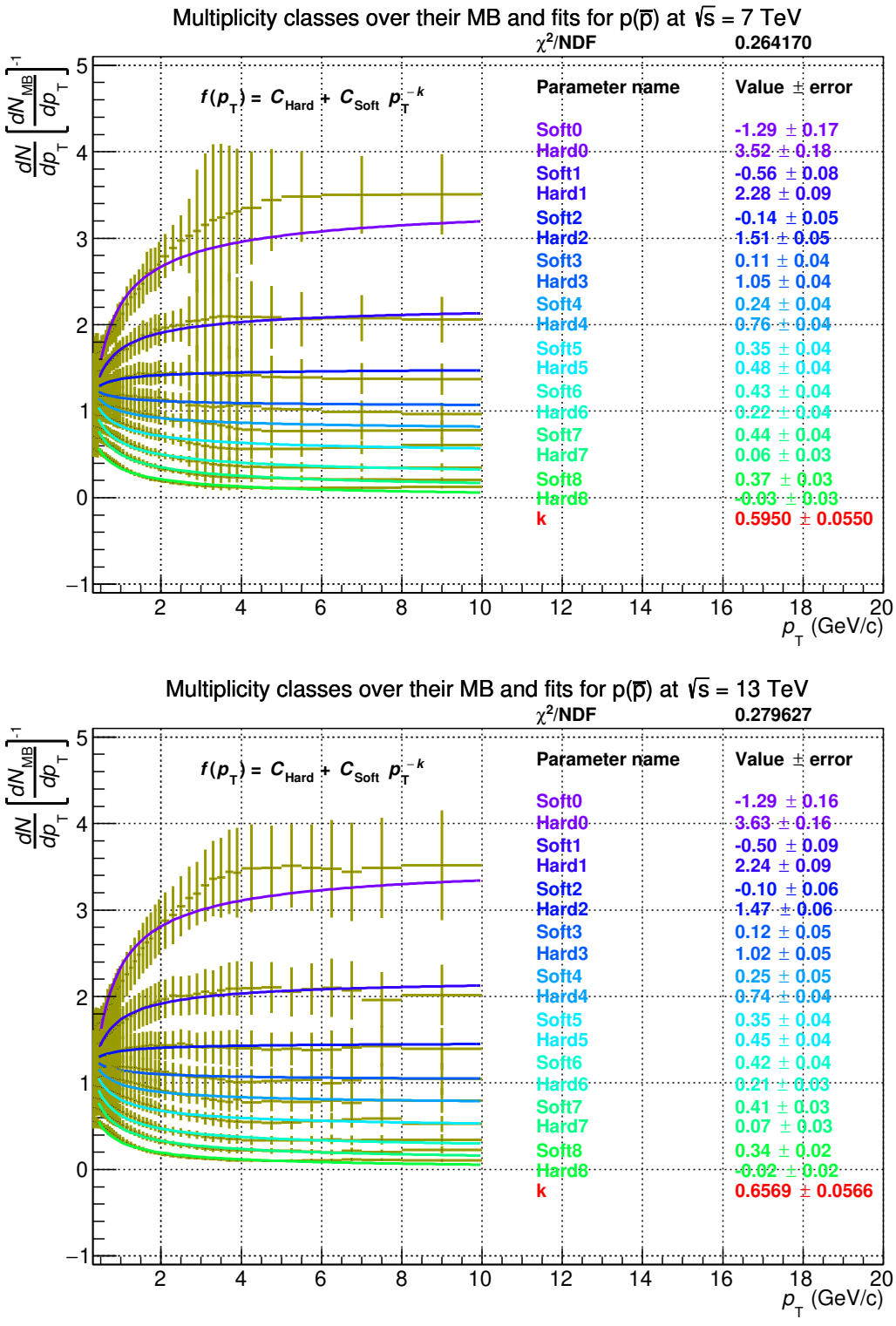

Figure 20: For (anti)protons, p($\bar{\text{p}}$), at $\sqrt{s}$ = (7 (upper) and 13 (lower)) TeV the combined fit for all multiplicity classes excluding the lowest multiplicity can be seen in this figure. The function $f(p_{\mathrm{T}}) = C_{\mathrm{Hard}} + C_{\mathrm{Soft}} \cdot p_{\mathrm{T}}^{-k}$ was used for these fits.

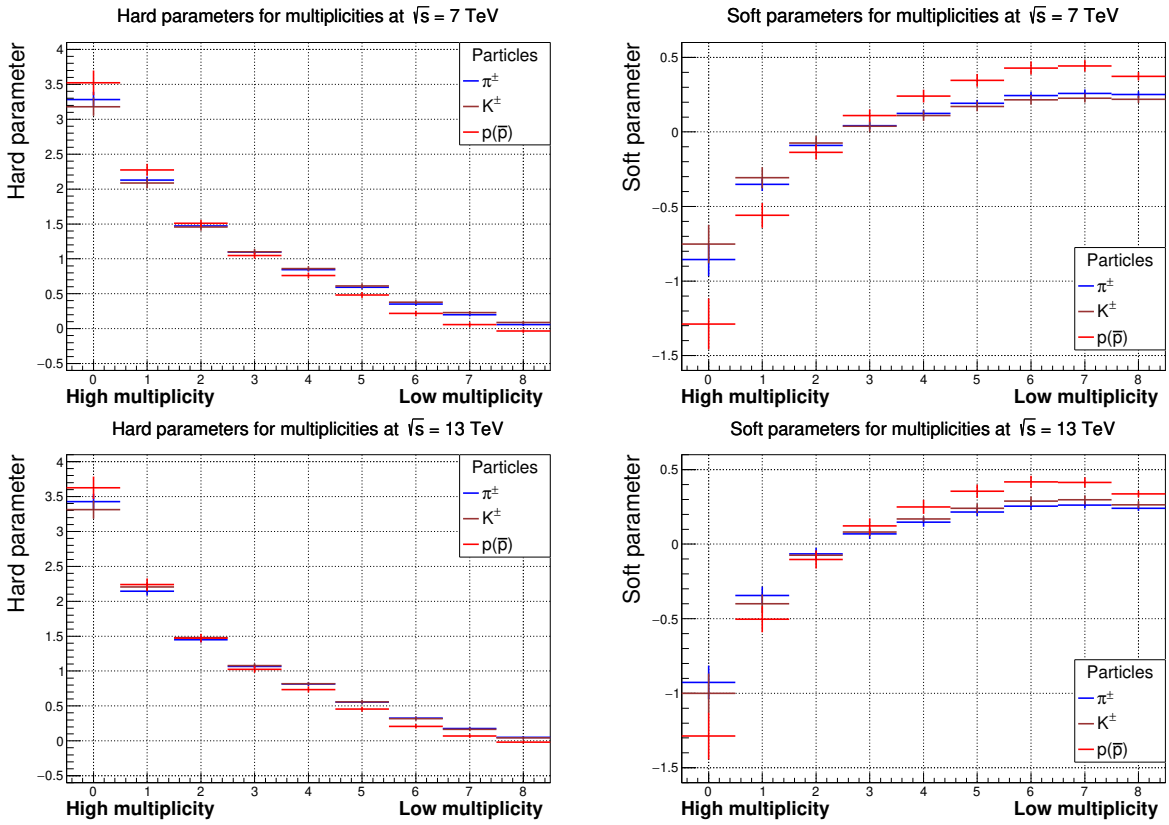

Figure 21: In the left column of figures the hard parameters for each multiplicity class and how their values fall towards higher multiplicity classes (with lower multiplicities) can be seen. In the right column of figures, the soft parameters for each multiplicity class and how their values increase towards higher multiplicity classes can be seen. Both of the figures in the upper row are from data at $\sqrt{s} = 7$ TeV and both of the figures in the lower row are from data at $\sqrt{s} = 13$ TeV.

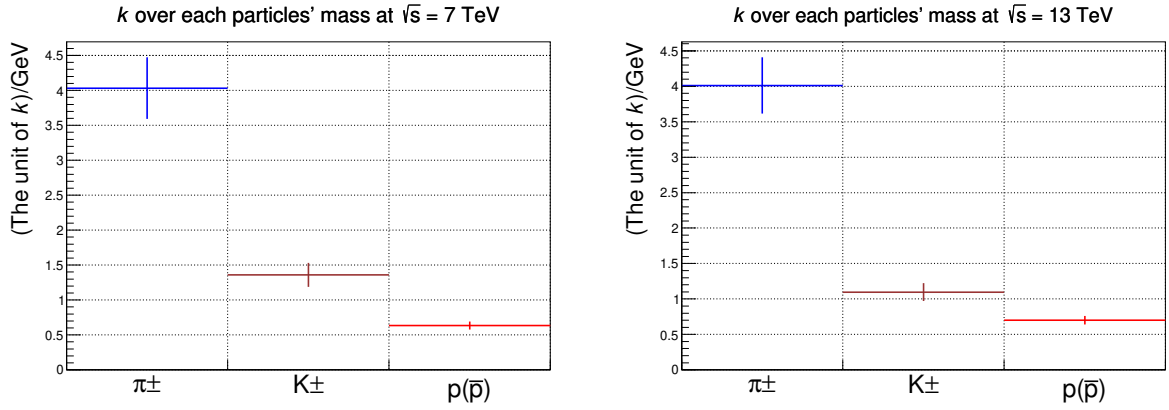

Figure 22: In these two figures the k-value for each particle ($\pi^{\pm}$, $K^{\pm}$ and $p(\bar{p})$) over their respective masses at $\sqrt{s} = (7$ (left) and 13 (right)) TeV. It can be seen that there is a decreasing trend for the k/mass-value as the particles' masses increase.

4 Conclusion and Outlook

In summary, p_{T} spectra were used in two steps. The first was to analyze what fit function could best describe the data among a selection. This was done since there has been an interest in being able to estimate the yields in p_{T} spectra for low p_{T}. It could be seen that the Lévy fit was the best partly because of the form of the function, having a parameter n that adjusts the tail of the function for high p_{T} and partly because of the number of parameters that are included in the formula. Although it was the best at fitting to high p_{T} it was the best for low p_{T} too. The Lévy function has a linear proportionality to p_{T} for low p_{T} and then around $p_{\mathrm{T}} = m$ it changes into a power law function, p_{T}^{1-n}. This approximately described the spectra and was why it could be found to be the best fit function.

From 10 multiplicity classes, 9 spectra were derived, together with the Minimum Bias (MB) spectrum. Ratios between the 9 spectra and the MB spectrum were then derived. A combined fit was made to these ratios and a set of Lévy fits were made to each multiplicity spectrum and MB spectrum. Throughout this work, the exponent of the main p_{T} dependent part of the Lévy fit to multiplicity classes' spectra has been called n1. The exponent of the main p_{T} dependent part of the Lévy fit to MB spectra has been called n2.

What could be seen in the Lévy fits for the energies $\sqrt{s}$ = (7 and 13) TeV was that the n2/mass-values for (anti)kaons and (anti)protons seemed to be slightly higher for 7 TeV than for 13 TeV while the value for (anti)pions is noticeably higher for 7 TeV. Though when looking at the n2-values and their errors it could be seen that they for (anti)kaons and (anti)protons overlap, while for (anti)pions the n2-values barely did not overlap. Although it could have been likely that a fit could have been found where the n2-values for (anti)pions overlap since the n2-value was in the order of 10^0 while the difference between the closest possible value for (7 and 13) TeV respectively was in the order of 10^{-3}.

Generally, for both (7 and 13) TeV it could be seen that the n2-values went down for increasing masses, all the n1-values seemed to increase with the energy and the n1-values goes down for increasing multiplicity classes. Although for (anti)pions the n1-values at both energies $\sqrt{s}$ = (7 and 13) TeV respectively, the lowest bin and the highest bin had overlapping error bars. Thus indicating a trend that the n1-values went down for increasing multiplicity classes for (anti)pions. It could also be noted that the decrease of the n1-values was the lowest for (anti)pions, higher for (anti)kaons, and highest for (anti)protons. It was also seen that the slope in n1-values for increasing multiplicity classes was the lowest for (anti)pions, slightly higher for (anti)kaons and the highest for (anti)protons.

High p_{T} is $p_{\mathrm{T}} > m$ according to the Lévy function, where m is the mass of the particle that the spectra have data from. The largest mass is the protons mass at $\sim$0.93 GeV/c^2 and the spectra are in the order of $p_{\mathrm{T}} = 1$ GeV/c. In the Lévy function, natural units are used and thus most of the spectra will be determined by n. We could observe that the spectra were dominated by jets from 4 GeV/c for (anti)pions (mass; $\sim$0.14 GeV/c) and (anti)kaons (mass; $\sim$0.49) and from 5 GeV/c for (anti)protons. Thus n determined mostly the transition between the part of the spectra affected by soft interactions and the part affected by jets.

For the combined fit it could be seen generally that the hard parameters went down and the soft parameters went up for increasing multiplicity classes. Including that the k/mass decreased for higher mass.

Overall it could be observed that the production of (anti)protons compared to the pro-

duction of (anti)pions and (anti)kaons was different, see Fig8. It could be noted from the n1-values and n2-values being close together for all multiplicity classes and all energies for (anti)pions and (anti)kaons while the n1-values and n2-values were significantly higher for (anti)protons. At $\sqrt{s} = 13$ TeV from the fit with Eq.18 an equal pattern could be noted where (anti)pions' and (anti)kaons' k-value were equivalent while the k-value for (anti)protons was higher. It could also be noted, for Eq.18, that the soft parameter for (anti)protons (two (anti)up quarks) had twice the value of the (anti)pions' and (anti)kaons' (one (anti)up quark) soft parameter for all multiplicity classes and all energies. The soft parameter has properties like the ones for n where it determines how fast the spectra should converge to the part of the spectra dominated by jets. The soft parameter was in turn dependent on the value of k, being constant for all multiplicity classes. k was only relevant for low p_{T} which is the region of interest for particles from QGP.

New studies to get more data that could solidify the results and trends that could be seen here should be done. Further studying the n1- and n2-values should be done. For other center-of-mass energies to observe whether their (anti)pions and (anti)kaons follow the same trends, different from the (anti)protons standing out like here. It would also be interesting to analyze other particles to study how their n-values behave.

There are plenty of things to try, among them, one could look at other fitting functions, especially for the combined fit. One could look at more energies to observe if the trends for n1- and n2-values for increasing energies hold. Other particles could be looked at to see if the seemingly increasing slope for increasing mass that could be seen for the n1-values also holds for other particles. One could also look at other particles to see if the n2-values are the same for bosons (here (anti)pions and (anti)kaons) and higher for fermions (here (anti)protons). Finally, other collisions than pp collisions should also be looked at to see if the same patterns hold, for instance in PbPb collisions.

References

[1] Rene Brun and Fons Rademakers. "ROOT — An object oriented data analysis framework". In: *Nuclear Instruments and Methods in Physics Research Section A: Accelerators, Spectrometers, Detectors and Associated Equipment* 389.1 (1997). New Computing Techniques in Physics Research V, pp. 81–86. ISSN: 0168-9002. DOI: https://doi.org/10.1016/S0168-9002(97)00048-X. URL: https://www.sciencedirect.com/science/article/pii/S016890029700048X.

[2] R. Brun et al. "Computing in ALICE". In: *Nuclear Instruments and Methods in Physics Research Section A: Accelerators, Spectrometers, Detectors and Associated Equipment* 502.2 (2003). Proceedings of the VIII International Workshop on Advanced Computing and Analysis Techniques in Physics Research, pp. 339–346. ISSN: 0168-9002. DOI: https://doi.org/10.1016/S0168-9002(03)00440-6. URL: https://www.sciencedirect.com/science/article/pii/S0168900203004406.

[3] Stanford Encyclopedia of Philosophy. *Ancient Atomism*. Last visited 2022-12-15. URL: https://plato.stanford.edu/entries/atomism-ancient/#LegaAnciAtom.

[4] Carl D. Anderson. "The Positive Electron". In: *Phys. Rev.* 43 (6 Mar. 1933), pp. 491–494. DOI: 10.1103/PhysRev.43.491. URL: https://link.aps.org/doi/10.1103/PhysRev.43.491.

[5] J. C. Street and E. C. Stevenson. "New Evidence for the Existence of a Particle of Mass Intermediate Between the Proton and Electron". In: *Phys. Rev.* 52 (9 Nov. 1937), pp. 1003–1004. DOI: 10.1103/PhysRev.52.1003. URL: https://link.aps.org/doi/10.1103/PhysRev.52.1003.

[6] G. D. ROCHESTERDr. and C. C. BUTLERDr. "Evidence for the Existence of New Unstable Elementary Particles". In: *Nature* 160.4077 (1947), pp. 855–857. DOI: https://doi.org/10.1038/160855a0.

[7] Ilya Obodovskiy. "Chapter 5 - Passing of Charged Particles Through Matter". In: *Radiation*. Ed. by Ilya Obodovskiy. Elsevier, 2019, pp. 103–136. ISBN: 978-0-444-63979-0. DOI: https://doi.org/10.1016/B978-0-444-63979-0.00005-7. URL: https://www.sciencedirect.com/science/article/pii/B9780444639790000057.

[8] J. Adam et al. "Production of light nuclei and anti-nuclei in *pp* and Pb-Pb collisions at energies available at the CERN Large Hadron Collider". In: *Phys. Rev. C* 93 (2 Feb. 2016), p. 024917. DOI: 10.1103/PhysRevC.93.024917. URL: https://link.aps.org/doi/10.1103/PhysRevC.93.024917.

[9] Leif Jönsson. *Lectures in Particle physics*. Lund University, 2017.

[10] *Standard Model of Elementary Particles*. Last visited 2022-12-15. URL: https://en.wikipedia.org/wiki/File:Standard_Model_of_Elementary_Particles.svg.

[11] Raghunath Sahoo. "Relativistic Kinematics". In: (2016). DOI: 10.48550/ARXIV.1604.02651. URL: https://arxiv.org/abs/1604.02651.

[12] David d'Enterria. "Quark–gluon matter". In: *Journal of Physics G: Nuclear and Particle Physics* 34.7 (May 2007), S53–S81. DOI: 10.1088/0954-3899/34/7/s04. URL: https://iopscience.iop.org/article/10.1088/0954-3899/34/7/S04.

[13] K. Adcox et al. "Formation of dense partonic matter in relativistic nucleus–nucleus collisions at RHIC: Experimental evaluation by the PHENIX Collaboration". In: *Nuclear Physics A* 757.1 (2005). First Three Years of Operation of RHIC, pp. 184–283. ISSN: 0375-9474. DOI: https://doi.org/10.1016/j.nuclphysa.2005.03.086. URL: https://www.sciencedirect.com/science/article/pii/S0375947405005300.

[14] J. Adam et al. "Enhanced production of multi-strange hadrons in high-multiplicity proton–proton collisions". In: *Nature Physics* 13 (6 June 2017), pp. 535–539. DOI: 10.1038/nphys4111. URL: https://doi.org/10.1038/nphys4111.

[15] The ALICE Collaboration et al. "The ALICE experiment at the CERN LHC". In: *Journal of Instrumentation* 3.08 (Aug. 2008), S08002. DOI: 10.1088/1748-0221/3/08/S08002. URL: https://dx.doi.org/10.1088/1748-0221/3/08/S08002.

[16] C. Garabatos. "The ALICE TPC". In: *Nuclear Instruments and Methods in Physics Research Section A: Accelerators, Spectrometers, Detectors and Associated Equipment* 535 (1 Jan. 2004), pp. 197–200. DOI: 10.1016/j.nima.2004.07.127. URL: https://doi.org/10.1016/j.nima.2004.07.127.

[17] CERN Courier. *ALICE revolutionizes TOF systems*. Last visited 2022-12-15. 25 October 2011. URL: https://cerncourier.com/a/alice-revolutionizes-tof-systems/.

[18] CERN M. Floris. *AliPWGFunc.h*. URL: http://alidoc.cern.ch/AliPhysics/vAN-20181002/_ali_p_w_g_func_8h_source.html.

[19] CERN M. Floris. *AliPWGFunc.cxx*. URL: http://alidoc.cern.ch/AliPhysics/vAN-20181002/_ali_p_w_g_func_8cxx_source.html.

[20] Mariana Frank et al. "Event Shape and Multiplicity Dependence of Freeze-Out Scenario and System Thermodynamics in Proton+Proton Collisions at $\sqrt{s} = 13$ TeV Using PYTHIA8". In: *Advances in High Energy Physics* 2021 (Feb. 2021). DOI: 10.1088/0954-3899/34/7/s04. URL: https://iopscience.iop.org/article/10.1088/0954-3899/34/7/S04.

[21] Pushpa Rathie and Sergio Da Silva. "Shannon, Lévy, and Tsallis: A Note". In: *Applied Mathematical Sciences (Ruse)* 2 (Jan. 2008). URL: https://www.researchgate.net/publication/255591659.

[22] Omar Vazquez Rueda. "Study of the production of π, K and p in pp collisions at $\sqrt{s} = 13$ TeV as a function of the Transverse Spherocity and the Relative Transverse Activity". English. PhD thesis. Faculty of Science, 2022. ISBN: 978-91-8039-281-5.

[23] Oliver Matonoha. URL: https://moriond.in2p3.fr/QCD/2021/FridayMorning/Matonoha.pdf.

[24] *HEPData*. URL: https://www.hepdata.net/.

[25] *HEPData 7 TeV*. Last visited 2022-12-15. RUN 1. URL: https://www.hepdata.net/record/ins1684320.

[26] S. Acharya et al. "Multiplicity dependence of light-flavor hadron production in pp collisions at $\sqrt{s} = 7\,\text{TeV}$". In: *Phys. Rev. C* 99 (2 Feb. 2019), p. 024906. DOI: 10.1103/PhysRevC.99.024906. URL: https://link.aps.org/doi/10.1103/PhysRevC.99.024906.

[27] *HEPData 13 TeV*. Last visited 2022-12-15. RUN 2. URL: https://www.hepdata.net/record/ins1784041.

[28] S. Acharya et al. "Multiplicity dependence of π, K, and p production in pp collisions at $\sqrt{s} = 13$ TeV". In: *The European Physical Journal C* 80 (8 Aug. 2020), p. 693. DOI: 10.1140/epjc/s10052-020-8125-1. URL: https://doi.org/10.1140/epjc/s10052-020-8125-1.

[29] Andreas Stokkeland. *The Code for fits to different multiplicity classes.* URL: https://github.com/andreasstokkeland/FitsAt7and13TeV.git.

5 Appendix, Combined fits

5.1 $f(p_{\mathrm{T}}) = C_{\mathrm{Hard}} + C_{\mathrm{Soft}} \mathrm{e}^{k/p_{\mathrm{T}}}$

In this section, the results from a combined fit using the function $f(p_{\mathrm{T}}) = C_{\mathrm{Hard}} + C_{\mathrm{Soft}} \mathrm{e}^{k/p_{\mathrm{T}}}$ will be presented. Starting with the spectra and their fits, Fig.23, Fig.24, and Fig.25, and then the parameters from the fit, Fig.26 and Fig.27.

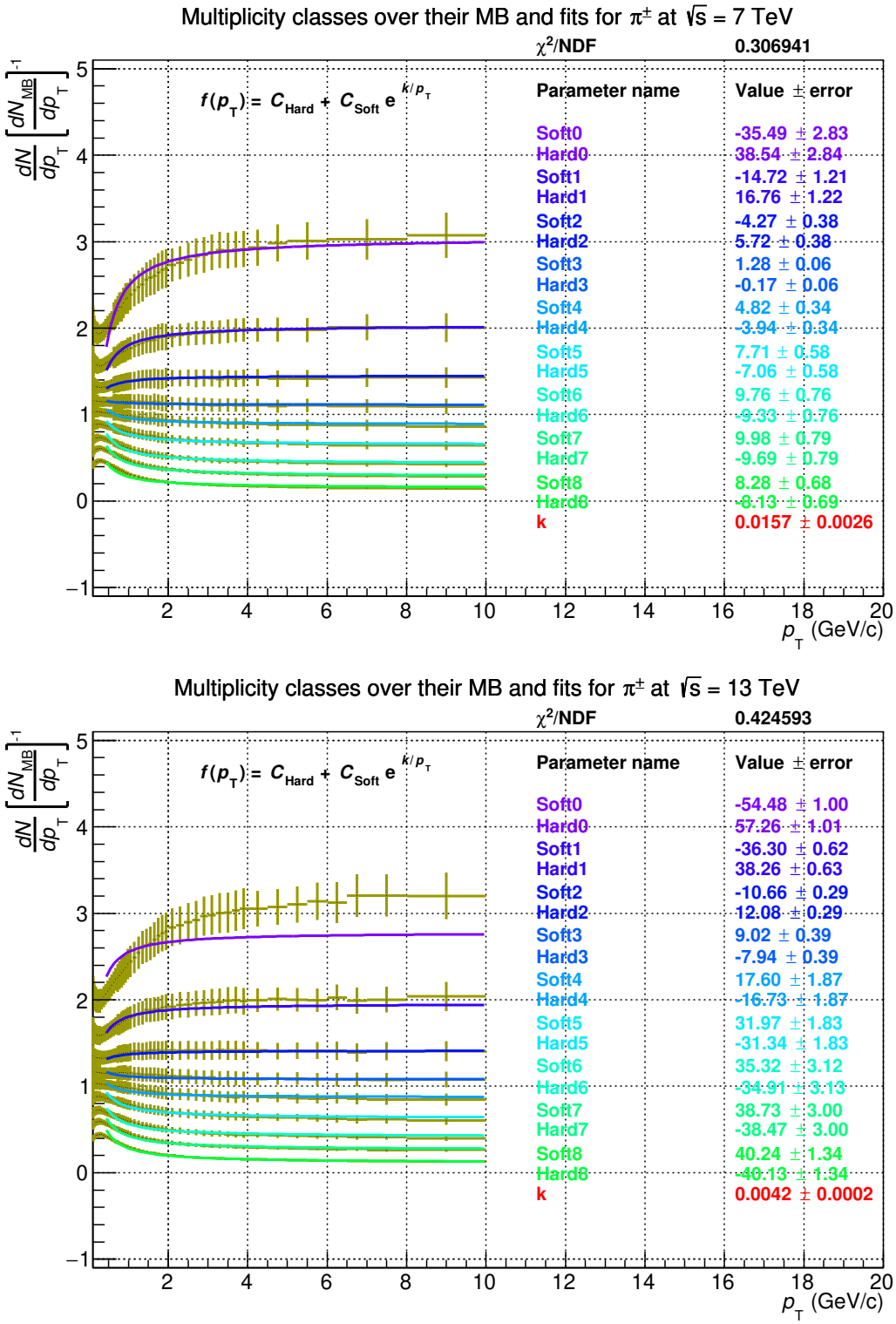

Figure 23: For (anti)pions, $\pi^{\pm}$, at $\sqrt{s}$ = (7 (upper) and 13 (lower)) TeV the combined fit for all multiplicity classes excluding the lowest multiplicity can be seen in this figure. The function $f(p_{\mathrm{T}}) = C_{\mathrm{Hard}} + C_{\mathrm{Soft}} \mathrm{e}^{k/p_{\mathrm{T}}}$ was used for these fits.

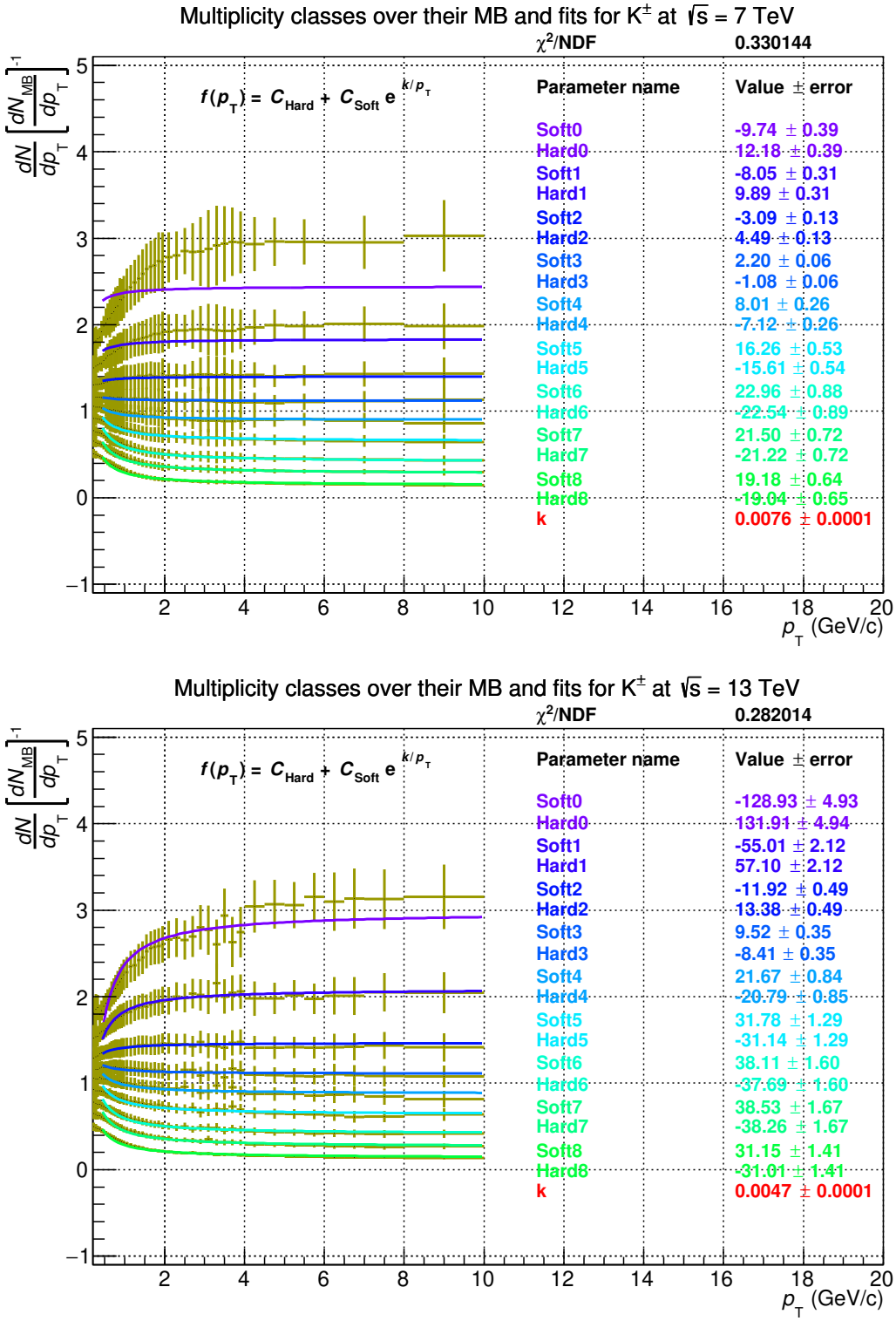

Figure 24: For (anti)kaons, $K^{\pm}$, at $\sqrt{s}$ = (7 (upper) and 13 (lower)) TeV the combined fit for all multiplicity classes excluding the lowest multiplicity can be seen in this figure. The function $f(p_T) = C_{\mathrm{Hard}} + C_{\mathrm{Soft}} e^{k/p_T}$ was used for these fits.

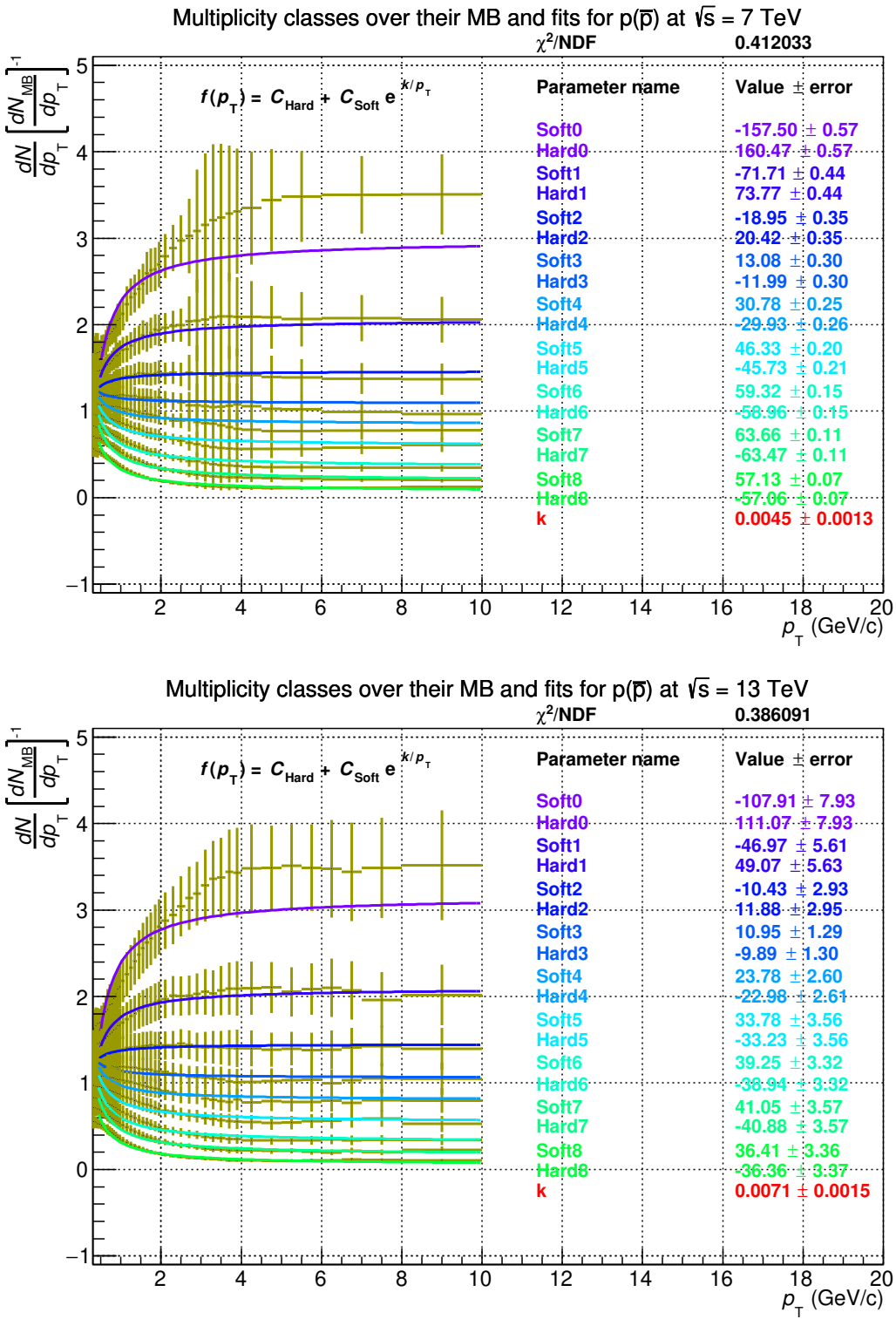

Figure 25: For (anti)protons, p($\bar{\text{p}}$), at $\sqrt{s}$ = (7 (upper) and 13 (lower)) TeV the combined fit for all multiplicity classes excluding the lowest multiplicity can be seen in this figure. The function $f(p_{\text{T}}) = C_{\text{Hard}} + C_{\text{Soft}} \text{e}^{k/p_{\text{T}}}$ was used for these fits.

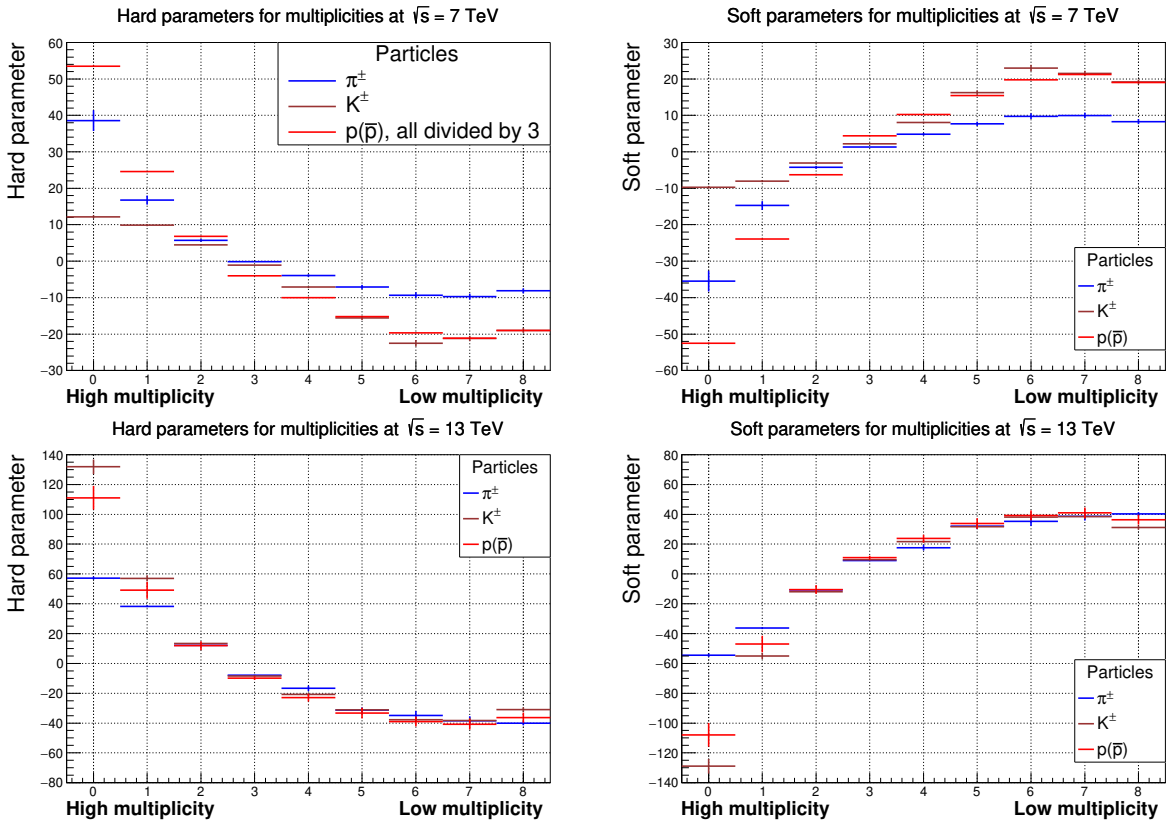

Figure 26: In the left column of figures the hard parameters for each multiplicity class and how their values fall towards higher multiplicity classes (with lower multiplicities) can be seen. In the right column of figures, the soft parameters for each multiplicity class and how their values increase towards higher multiplicity classes can be seen. Both of the figures in the upper row are from data at $\sqrt{s} = 7$ TeV and both of the figures in the lower row are from data at $\sqrt{s} = 13$ TeV.

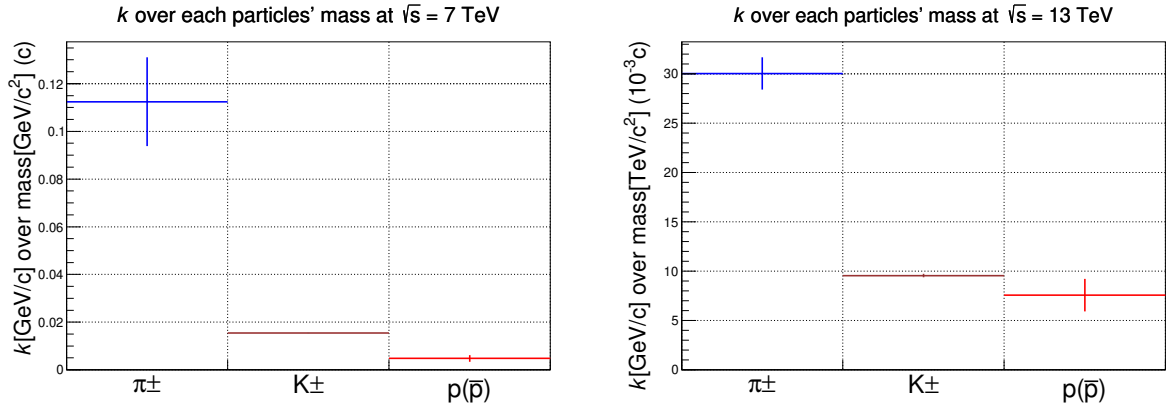

Figure 27: In these two figures the k-value for each particle ($\pi^{\pm}$, $K^{\pm}$ and $p(\bar{p})$) over their respective masses at $\sqrt{s} = (7$ (left) and 13 (right)) TeV. It can be seen that there is a decreasing trend for the k/mass-value as the particles' masses increase.

6 Appendix, the comparison of fits to p_{T} spectra

6.1 (Anti)pions ($\pi^{\pm}$)

In this section (Fig.28, Fig.29, Fig.30, Fig.31, Fig.32, Fig.33) the fitted fit functions presented in section 2.6 to p_{T}-spectra with data from (anti)pions ($\pi^{\pm}$) are presented.

6.2 (Anti)kaons ($\mathrm{K}^{\pm}$)

In this section (Fig.34, Fig.35, Fig.36, Fig.37, Fig.38, Fig.39) the fitted fit functions presented in section 2.6 to p_{T}-spectra with data from (anti)kaons ($\mathrm{K}^{\pm}$) are presented.

6.3 Kaon short ($\mathrm{K}^{0}_{\mathrm{S}}$)

In this section (Fig.40, Fig.41, Fig.42, Fig.43, Fig.44, Fig.45) the fitted fit functions presented in section 2.6 to p_{T}-spectra with data from kaon short ($\mathrm{K}^{0}_{\mathrm{S}}$) are presented.

6.4 (Anti)protons ($\mathrm{p}(\bar{\mathrm{p}})$)

In this section (Fig.46, Fig.47, Fig.48, Fig.49, Fig.50, Fig.51) the fitted fit functions presented in section 2.6 to p_{T}-spectra with data from (anti)protons ($\mathrm{p}\bar{\mathrm{p}}$) are presented.

6.5 Lambdas (Λ^{0})

In this section (Fig.52, Fig.53, Fig.54, Fig.55, Fig.56, Fig.57) the fitted fit functions presented in section 2.6 to p_{T}-spectra with data from lambdas (Λ^{0}) are presented.

6.6 Antilambdas ($\bar{\Lambda}^{0}$)

In this section (Fig.58, Fig.59, Fig.60, Fig.61, Fig.62, Fig.63) the fitted fit functions presented in section 2.6 to p_{T}-spectra with data from antilambdas ($\bar{\Lambda}^{0}$) are presented.

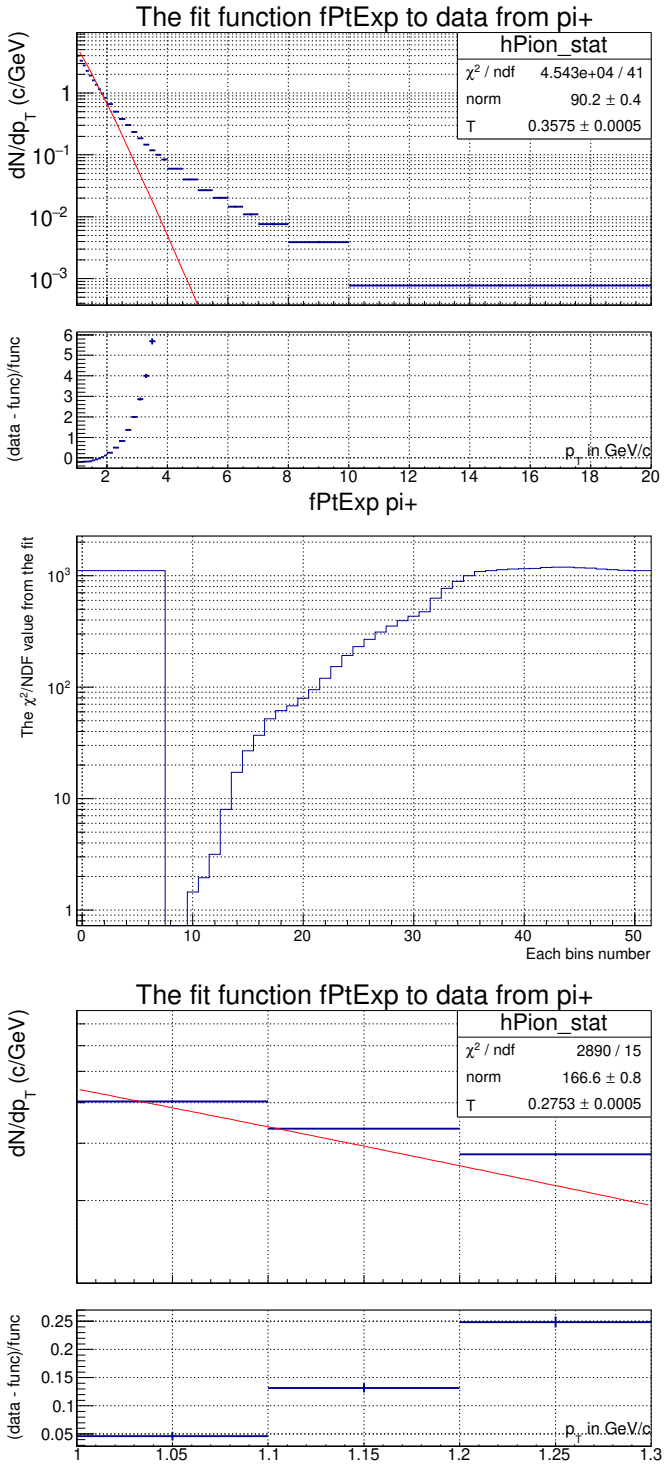

Figure 28: The upper histogram with its fit shows the spectra for the full range. The figure in the middle shows a plot with the number of the upper bin included in a fit, on the x-axis and the χ^2/NDF-value from the fit on the y-axis. The lower histogram shows the histogram for the range in which the fit could be deemed valid from the middle figure.

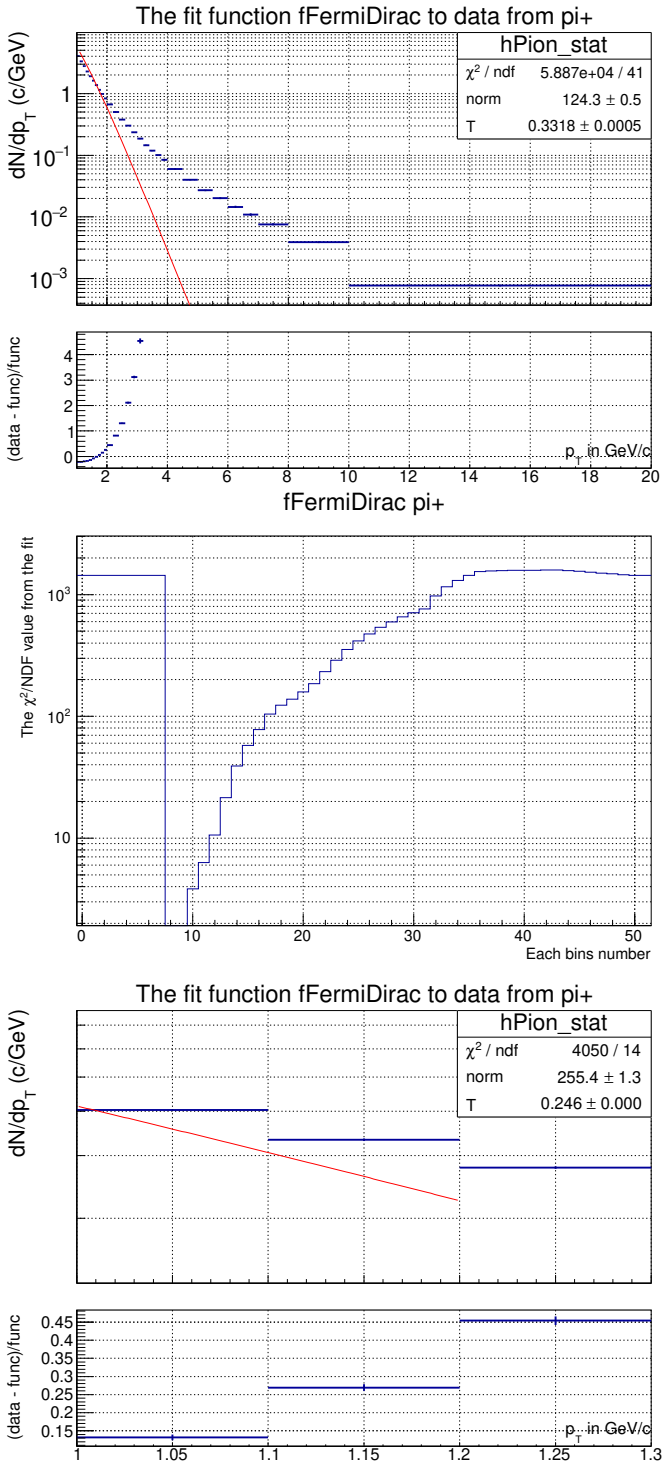

Figure 29: The upper histogram with its fit shows the spectra for the full range. The figure in the middle shows a plot with the number of the upper bin included in a fit, on the x-axis and the χ^2/NDF-value from the fit on the y-axis. The lower histogram shows the histogram for the range in which the fit could be deemed valid from the middle figure.

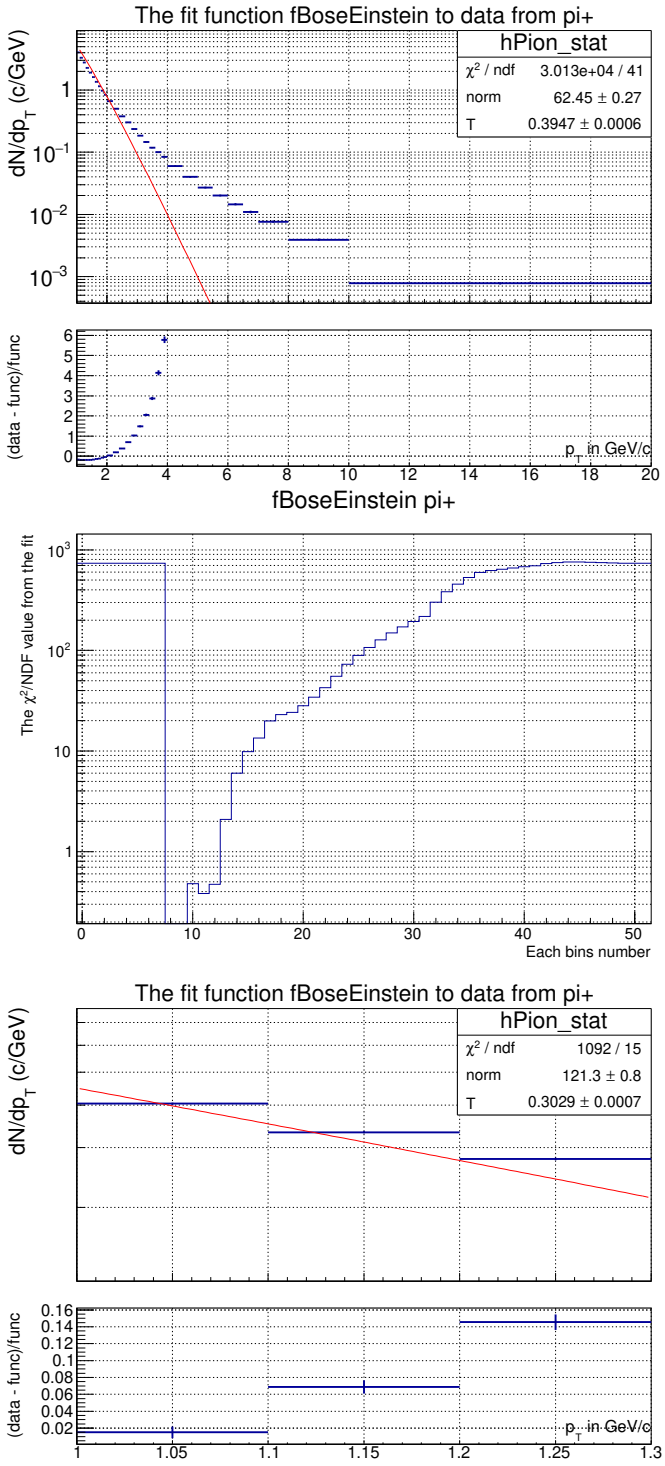

Figure 30: The upper histogram with its fit shows the spectra for the full range. The figure in the middle shows a plot with the number of the upper bin included in a fit, on the x-axis and the χ^2/NDF-value from the fit on the y-axis. The lower histogram shows the histogram for the range in which the fit could be deemed valid from the middle figure.

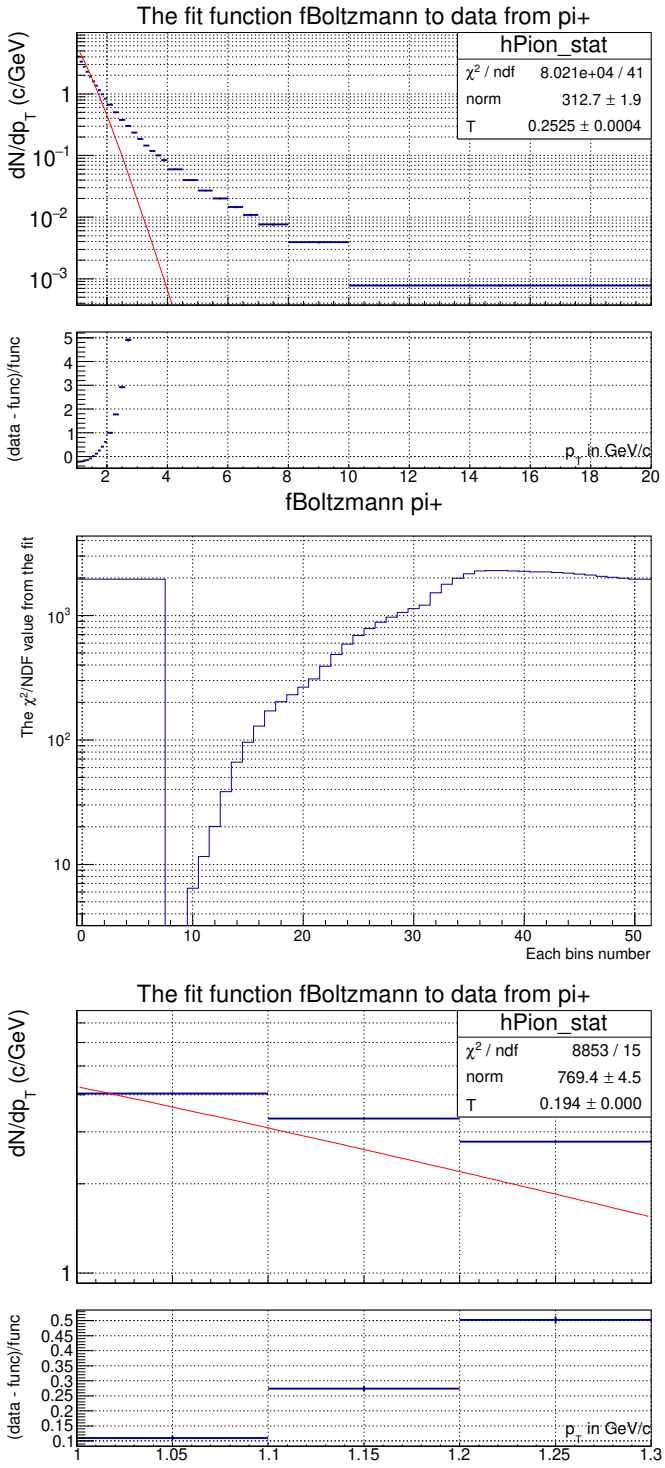

Figure 31: The upper histogram with its fit shows the spectra for the full range. The figure in the middle shows a plot with the number of the upper bin included in a fit, on the x-axis and the χ^2/NDF-value from the fit on the y-axis. The lower histogram shows the histogram for the range in which the fit could be deemed valid from the middle figure.

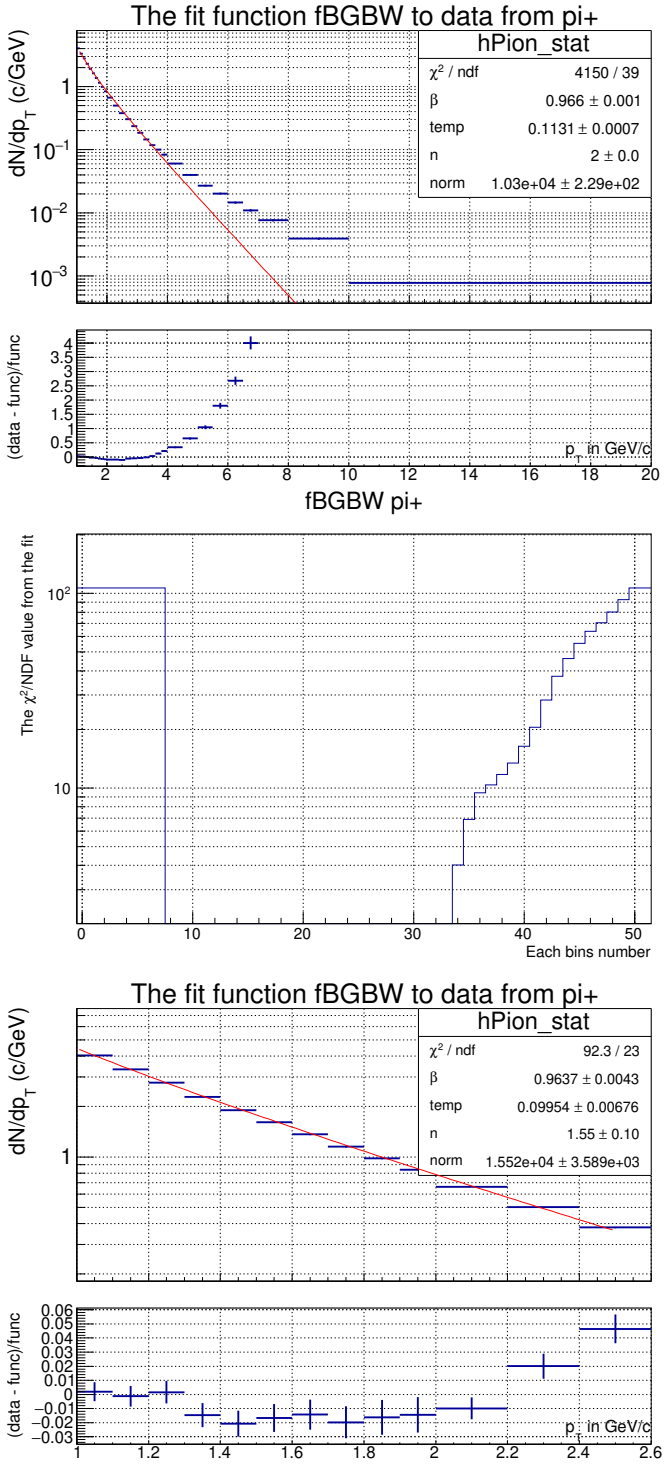

Figure 32: The upper histogram with its fit shows the spectra for the full range. The figure in the middle shows a plot with the number of the upper bin included in a fit, on the x-axis and the χ^2/NDF-value from the fit on the y-axis. The lower histogram shows the histogram for the range in which the fit could be deemed valid from the middle figure.

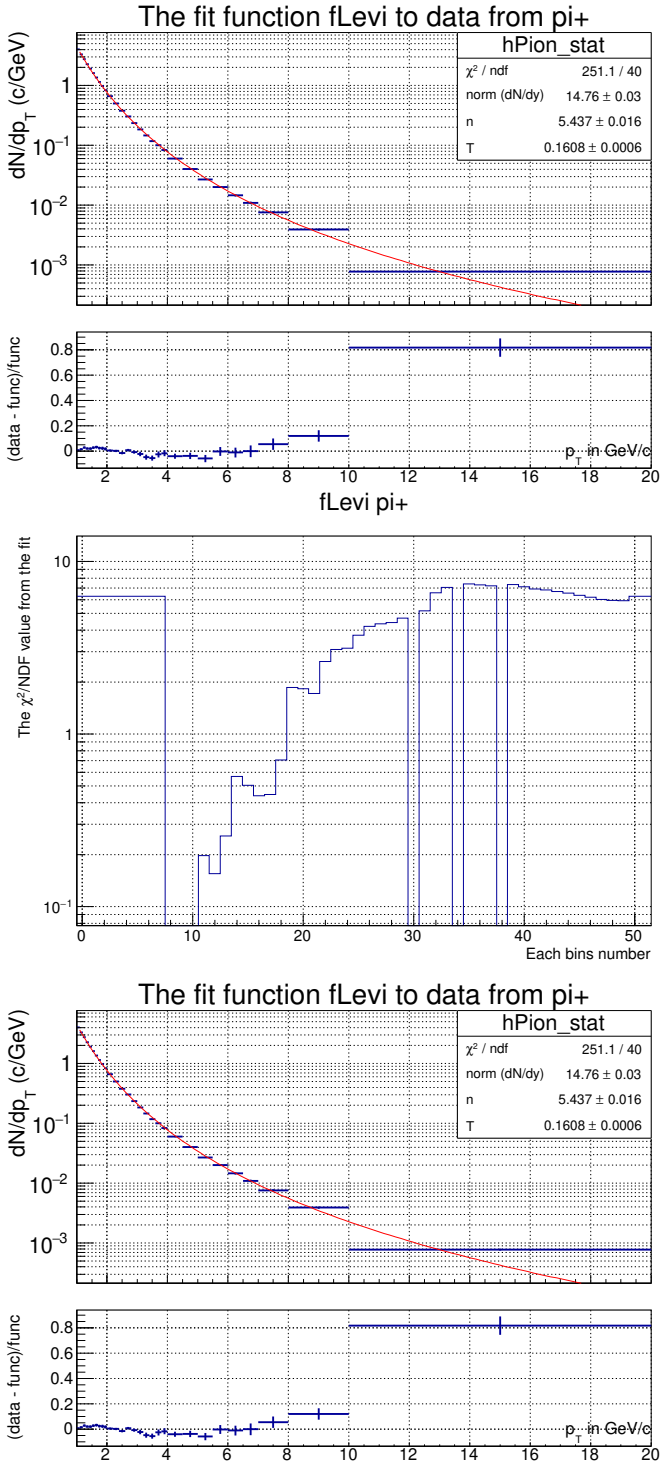

Figure 33: The upper histogram with its fit shows the spectra for the full range. The figure in the middle shows a plot with the number of the upper bin included in a fit, on the x-axis and the χ^2/NDF-value from the fit on the y-axis. The lower histogram shows the histogram for the range in which the fit could be deemed valid from the middle figure.

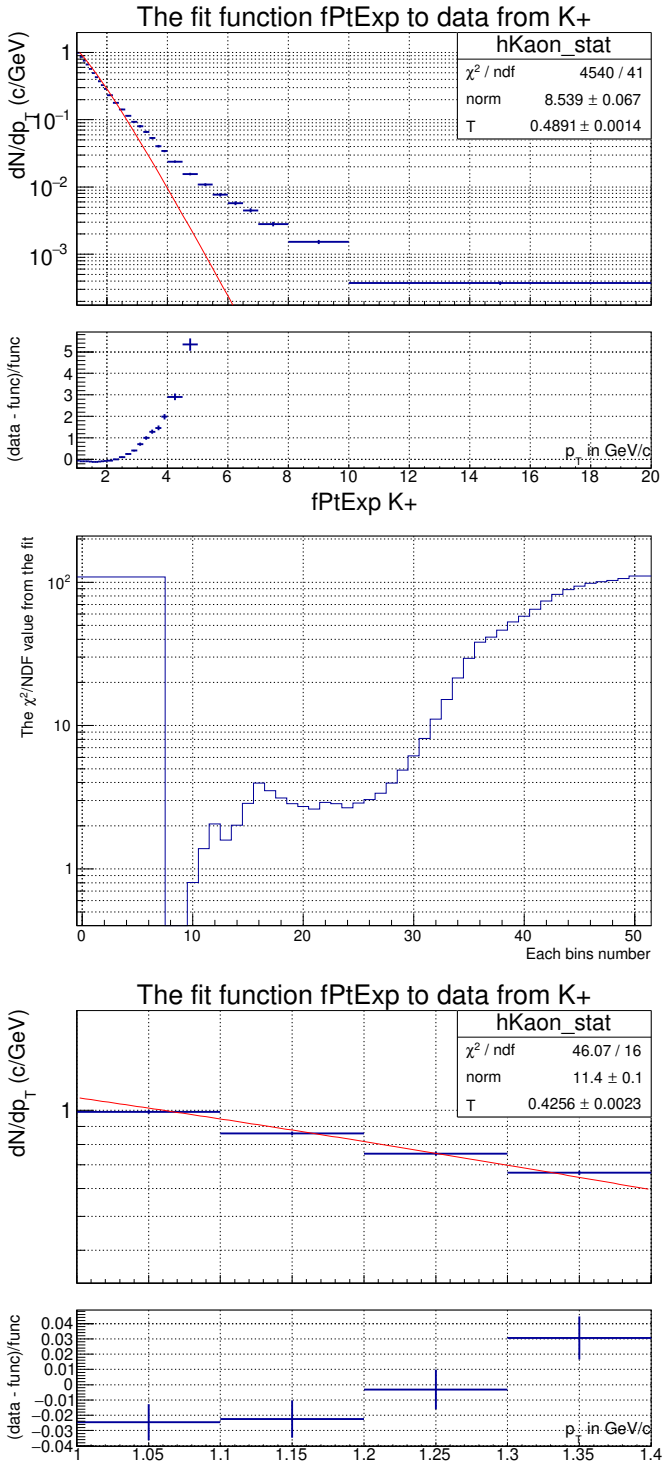

Figure 34: The upper histogram with its fit shows the spectra for the full range. The figure in the middle shows a plot with the number of the upper bin included in a fit, on the x-axis and the χ^2/NDF-value from the fit on the y-axis. The lower histogram shows the histogram for the range in which the fit could be deemed valid from the middle figure.

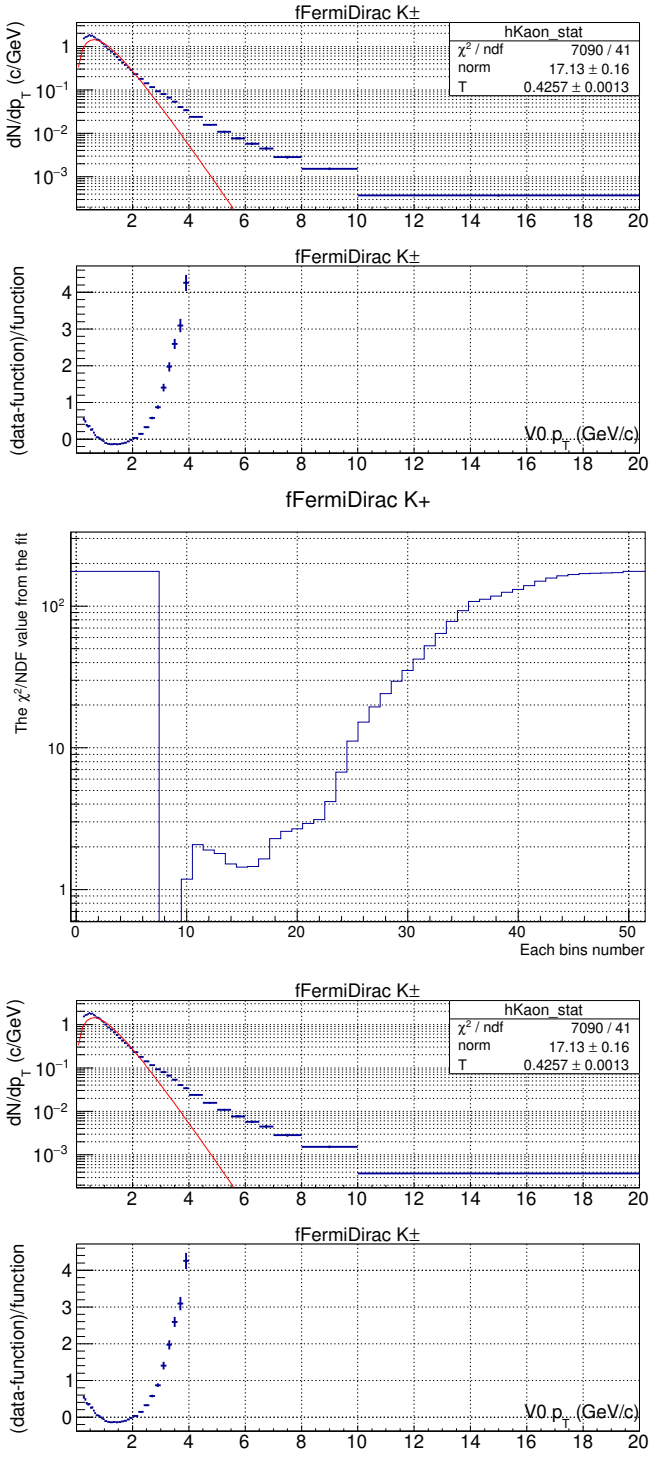

Figure 35: The upper histogram with its fit shows the spectra for the full range. The figure in the middle shows a plot with the number of the upper bin included in a fit, on the x-axis and the χ^2/NDF-value from the fit on the y-axis. The lower histogram shows the histogram for the range in which the fit could be deemed valid from the middle figure.

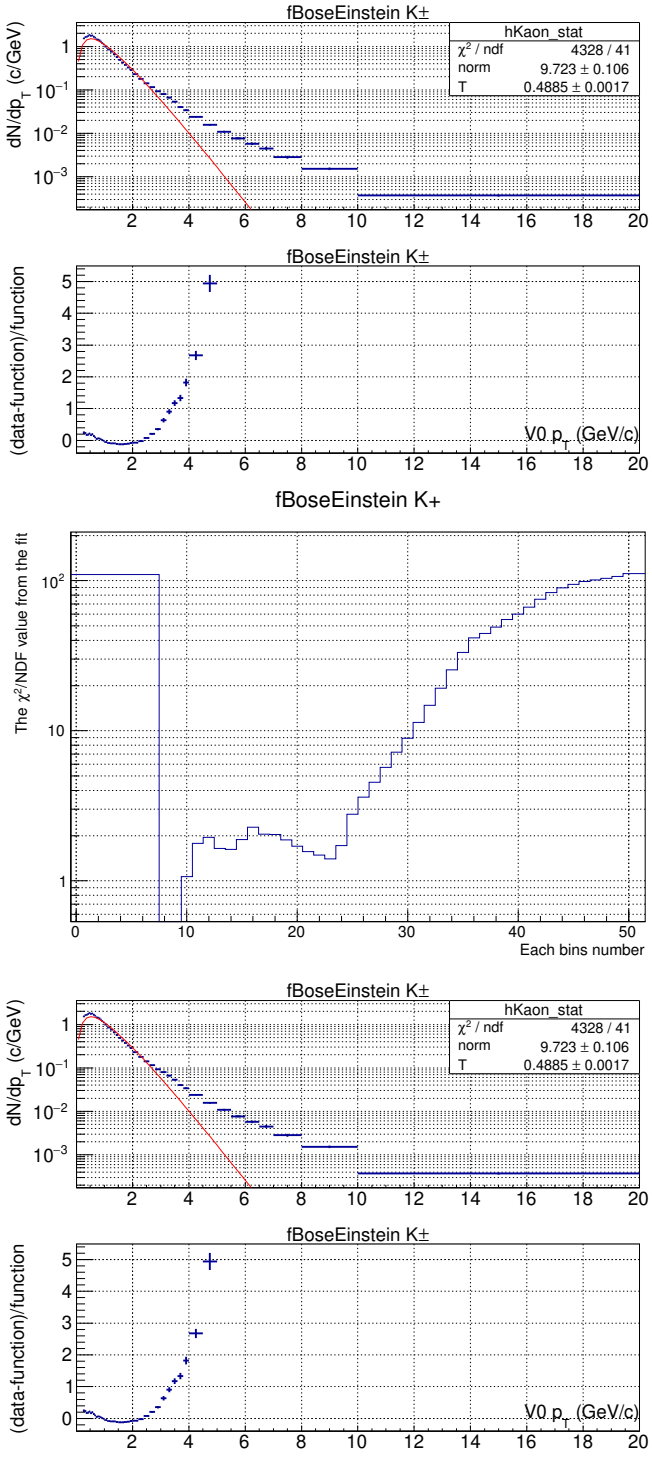

Figure 36: The upper histogram with its fit shows the spectra for the full range. The figure in the middle shows a plot with the number of the upper bin included in a fit, on the x-axis and the χ^2/NDF-value from the fit on the y-axis. The lower histogram shows the histogram for the range in which the fit could be deemed valid from the middle figure.

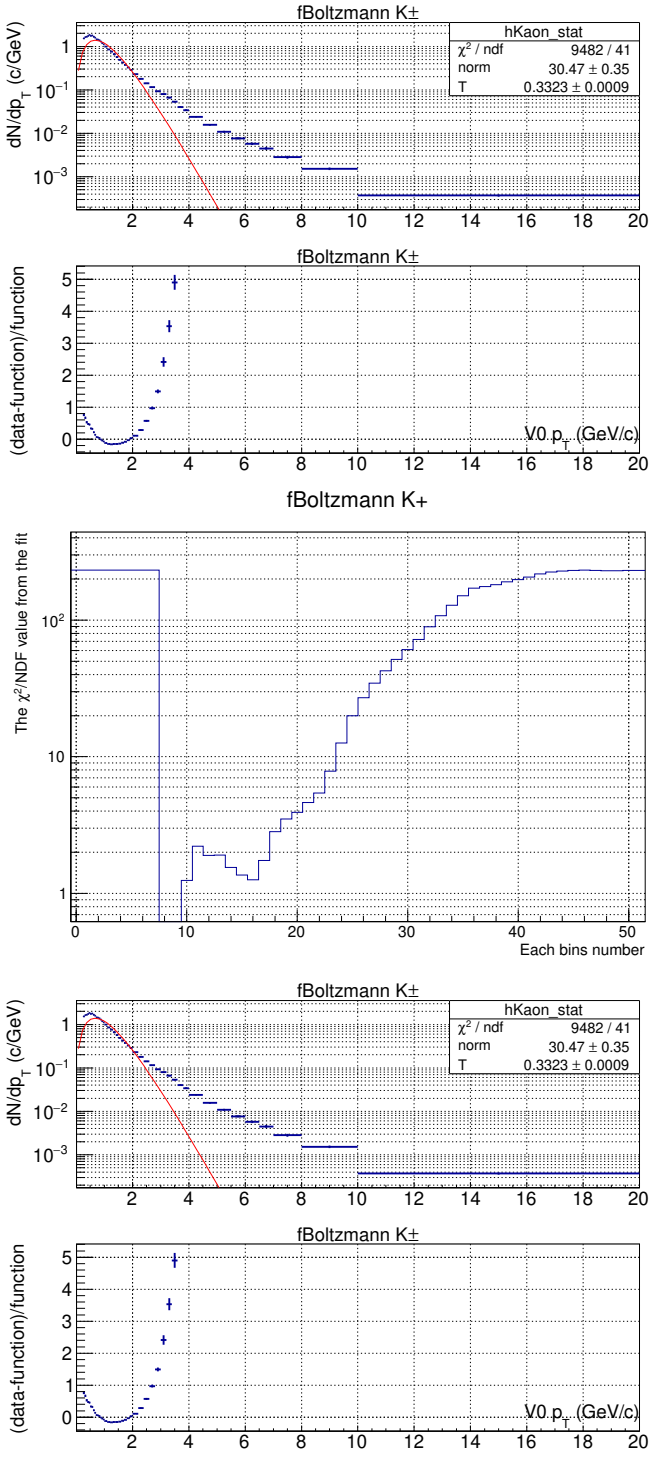

Figure 37: The upper histogram with its fit shows the spectra for the full range. The figure in the middle shows a plot with the number of the upper bin included in a fit, on the x-axis and the χ^2/NDF-value from the fit on the y-axis. The lower histogram shows the histogram for the range in which the fit could be deemed valid from the middle figure.

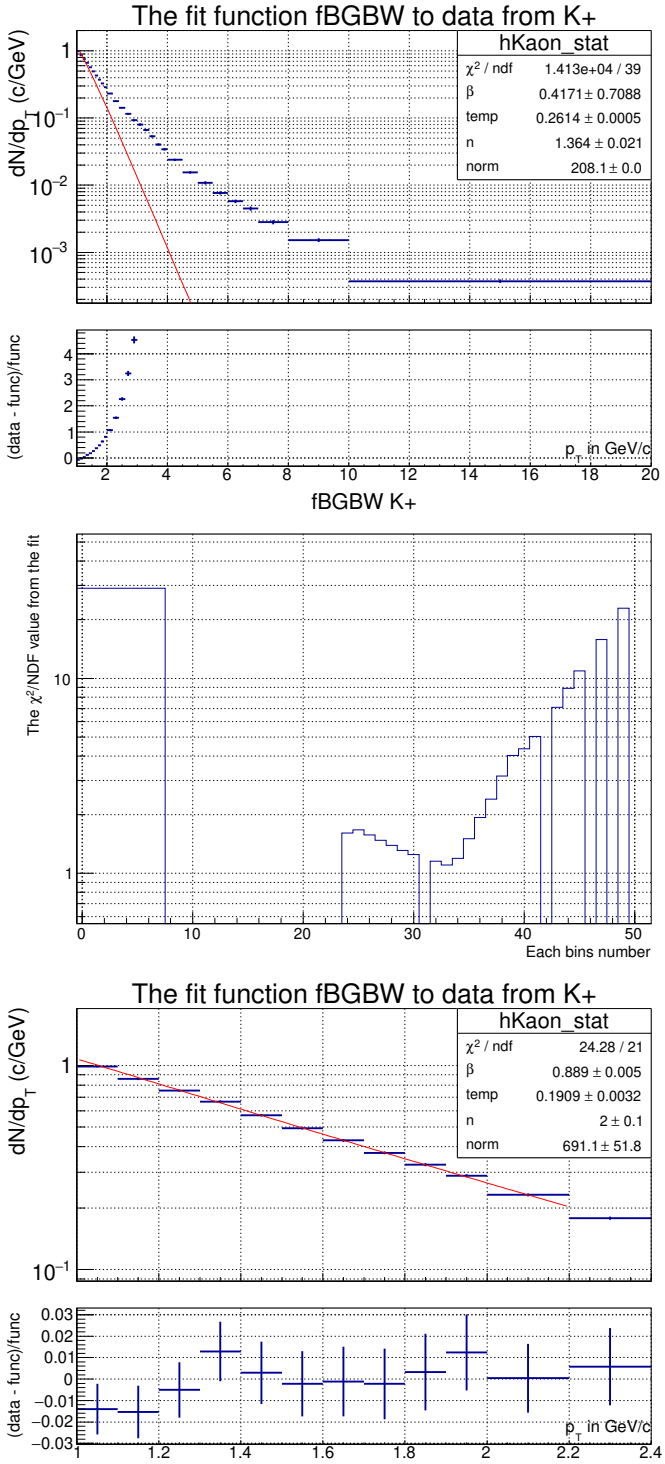

Figure 38: The upper histogram with its fit shows the spectra for the full range. The figure in the middle shows a plot with the number of the upper bin included in a fit, on the x-axis and the χ^2/NDF-value from the fit on the y-axis. The lower histogram shows the histogram for the range in which the fit could be deemed valid from the middle figure.

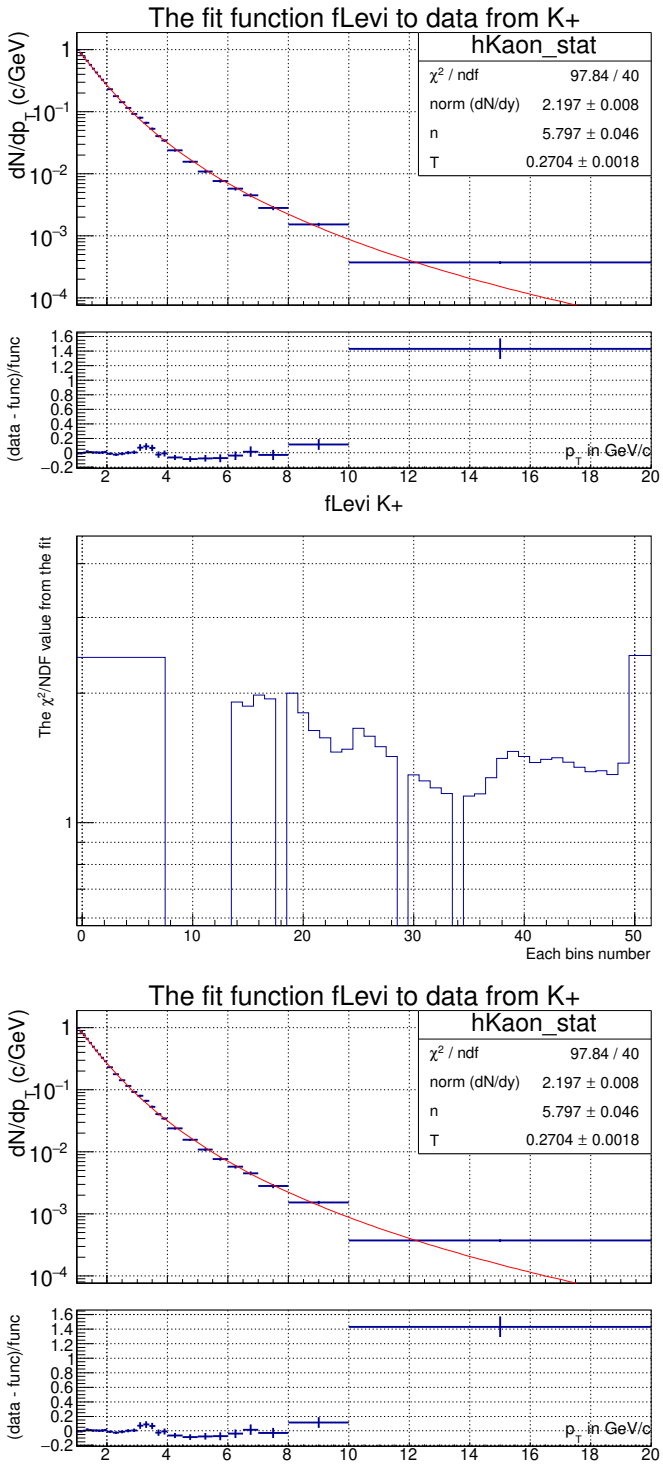

Figure 39: The upper histogram with its fit shows the spectra for the full range. The figure in the middle shows a plot with the number of the upper bin included in a fit, on the x-axis and the χ^2/NDF-value from the fit on the y-axis. The lower histogram shows the histogram for the range in which the fit could be deemed valid from the middle figure.

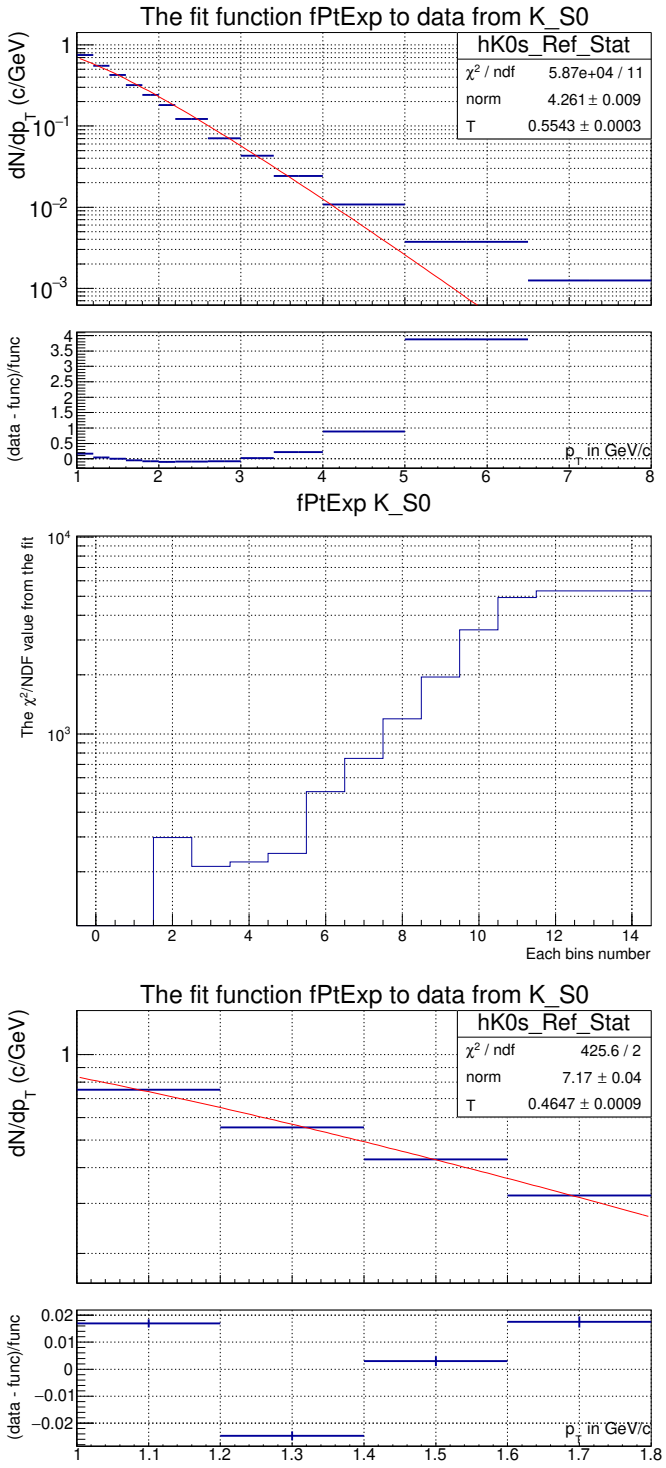

Figure 40: The upper histogram with its fit shows the spectra for the full range. The figure in the middle shows a plot with the number of the upper bin included in a fit, on the x-axis and the χ^2/NDF-value from the fit on the y-axis. The lower histogram shows the histogram for the range in which the fit could be deemed valid from the middle figure.

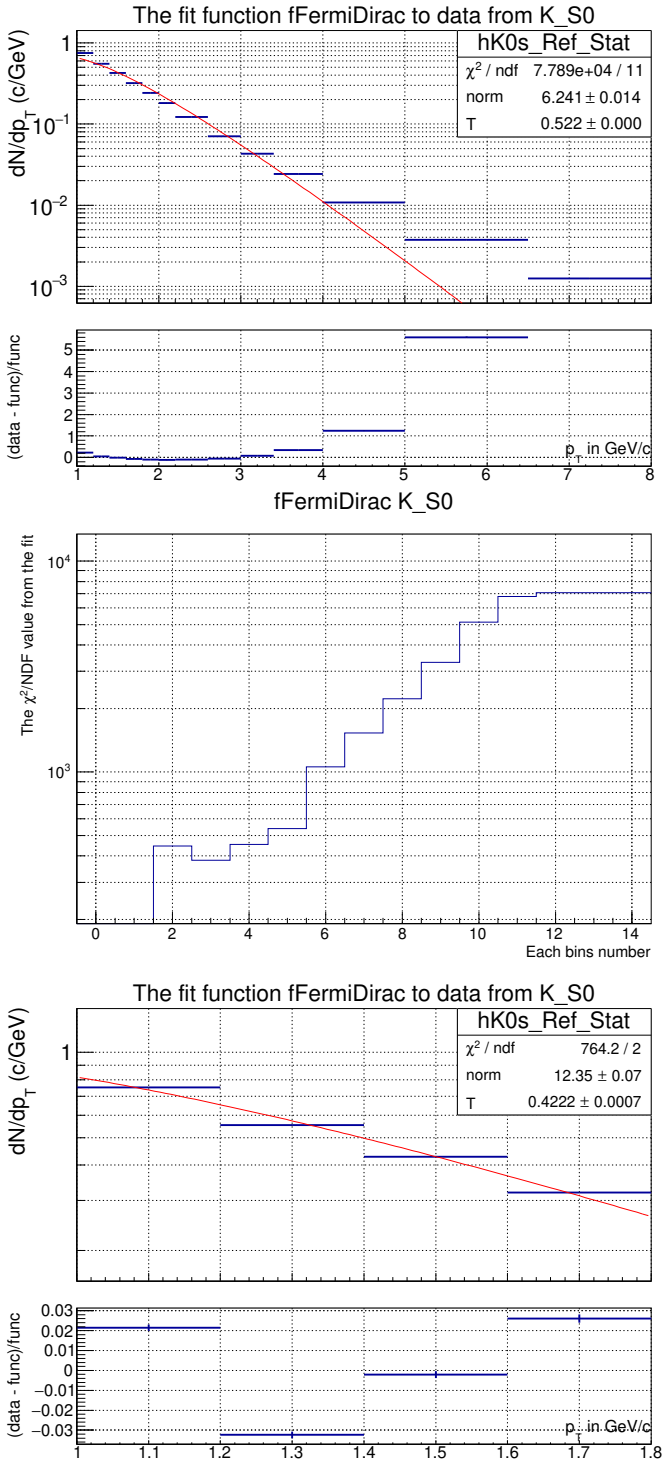

Figure 41: The upper histogram with its fit shows the spectra for the full range. The figure in the middle shows a plot with the number of the upper bin included in a fit, on the x-axis and the χ^2/NDF-value from the fit on the y-axis. The lower histogram shows the histogram for the range in which the fit could be deemed valid from the middle figure.

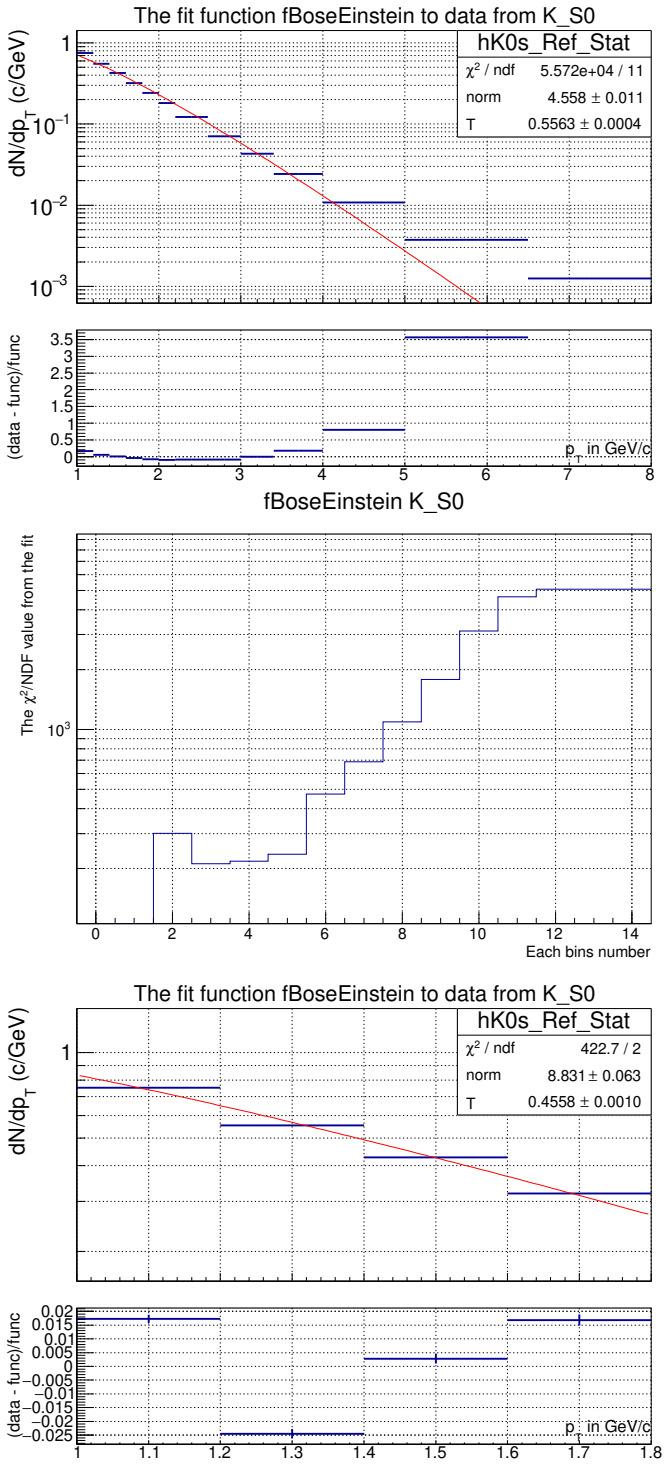

Figure 42: The upper histogram with its fit shows the spectra for the full range. The figure in the middle shows a plot with the number of the upper bin included in a fit, on the x-axis and the χ^2/NDF-value from the fit on the y-axis. The lower histogram shows the histogram for the range in which the fit could be deemed valid from the middle figure.

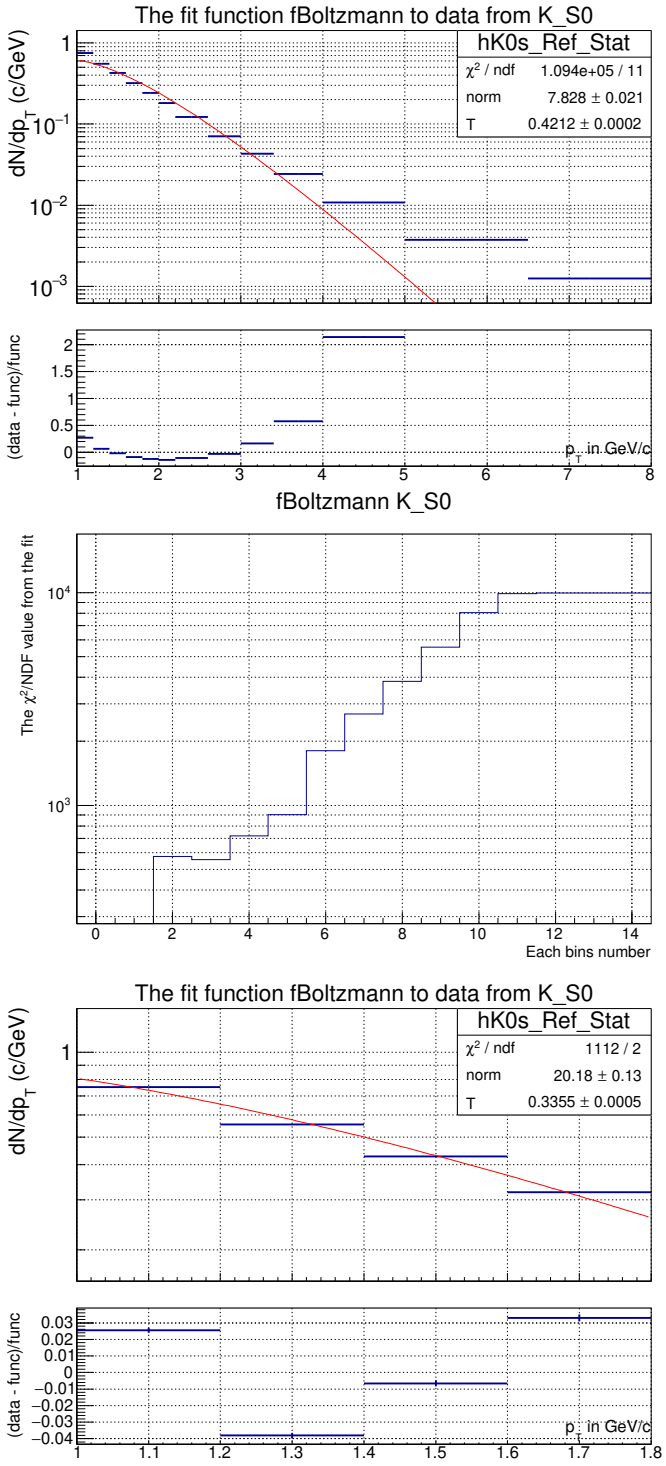

Figure 43: The upper histogram with its fit shows the spectra for the full range. The figure in the middle shows a plot with the number of the upper bin included in a fit, on the x-axis and the χ^2/NDF-value from the fit on the y-axis. The lower histogram shows the histogram for the range in which the fit could be deemed valid from the middle figure.

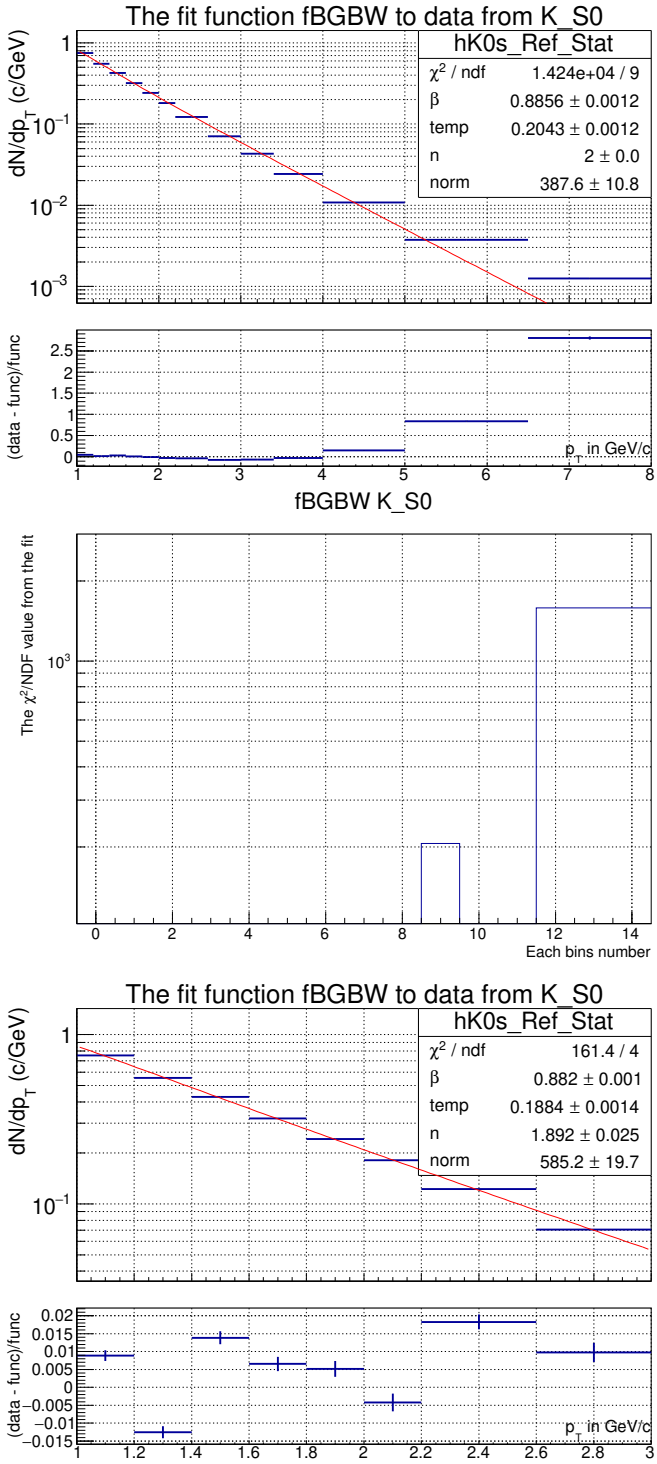

Figure 44: The upper histogram with its fit shows the spectra for the full range. The figure in the middle shows a plot with the number of the upper bin included in a fit, on the x-axis and the χ^2/NDF-value from the fit on the y-axis. The lower histogram shows the histogram for the range in which the fit could be deemed valid from the middle figure.

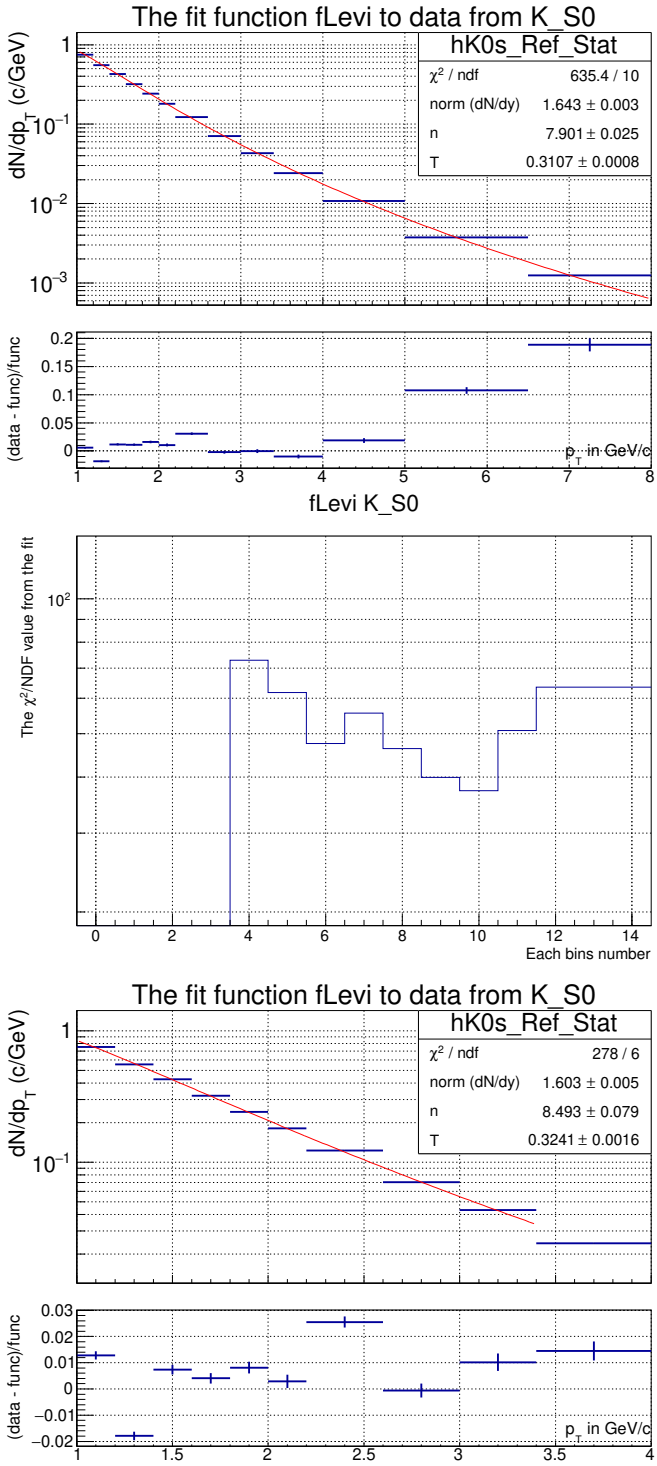

Figure 45: The upper histogram with its fit shows the spectra for the full range. The figure in the middle shows a plot with the number of the upper bin included in a fit, on the x-axis and the χ^2/NDF-value from the fit on the y-axis. The lower histogram shows the histogram for the range in which the fit could be deemed valid from the middle figure.

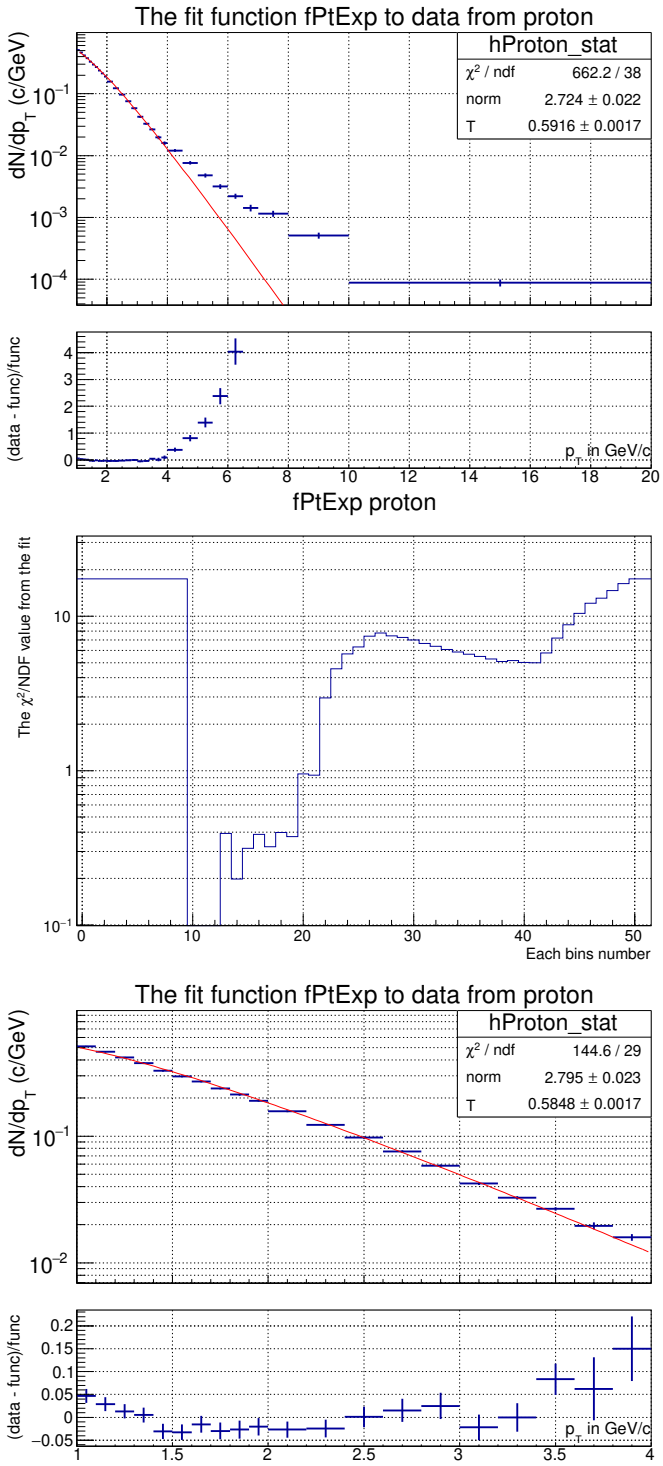

Figure 46: The upper histogram with its fit shows the spectra for the full range. The figure in the middle shows a plot with the number of the upper bin included in a fit, on the x-axis and the χ^2/NDF-value from the fit on the y-axis. The lower histogram shows the histogram for the range in which the fit could be deemed valid from the middle figure.

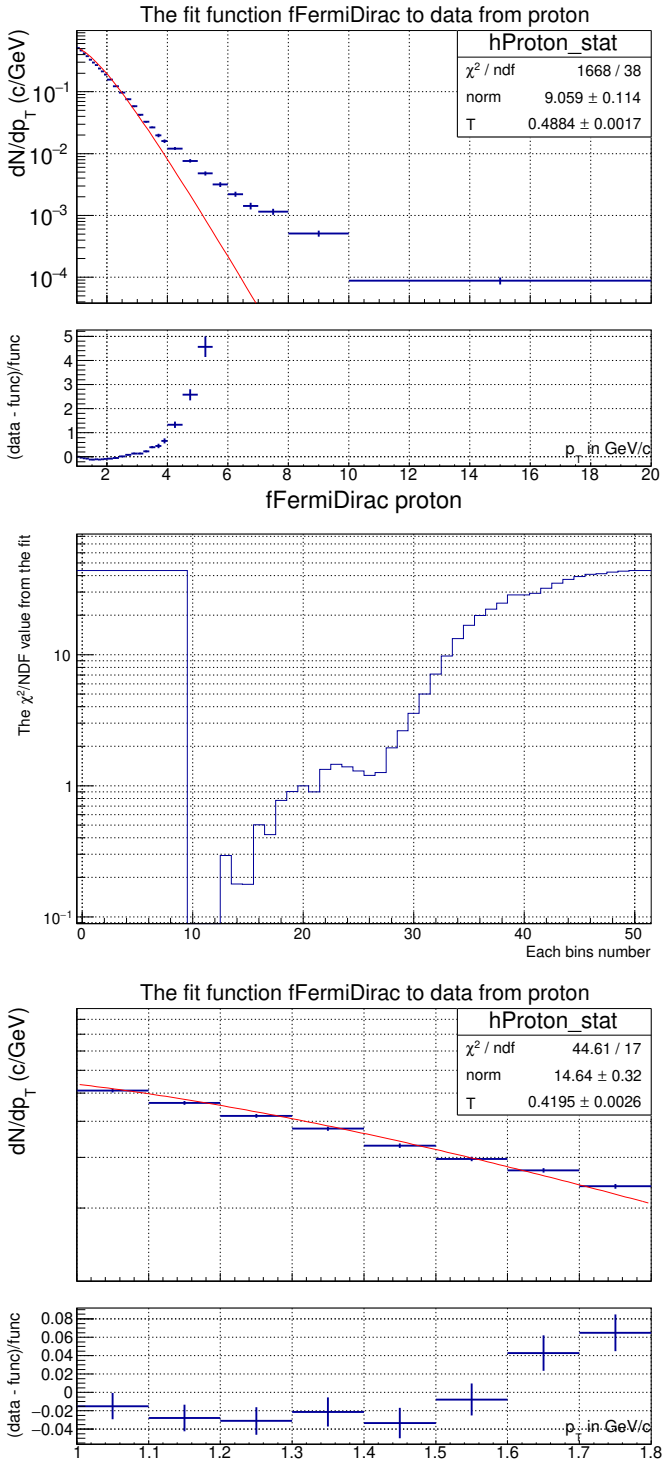

Figure 47: The upper histogram with its fit shows the spectra for the full range. The figure in the middle shows a plot with the number of the upper bin included in a fit, on the x-axis and the χ^2/NDF-value from the fit on the y-axis. The lower histogram shows the histogram for the range in which the fit could be deemed valid from the middle figure.

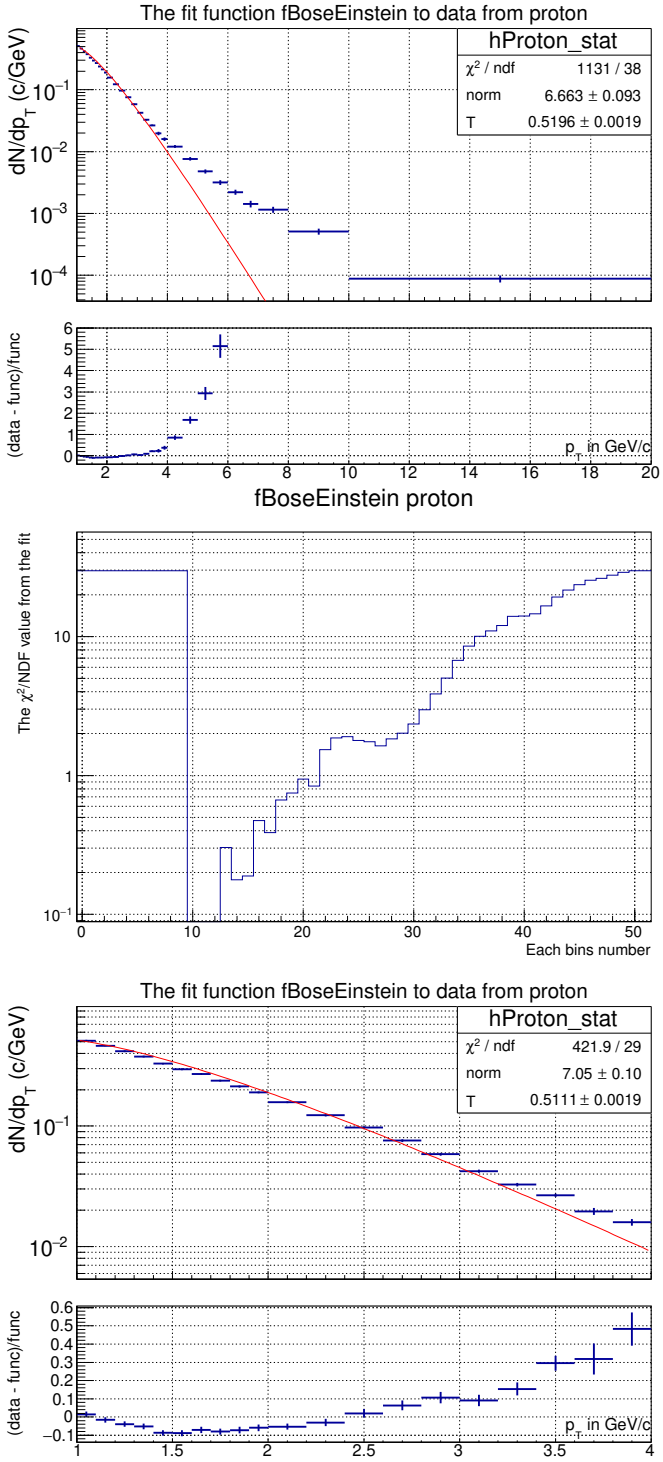

Figure 48: The upper histogram with its fit shows the spectra for the full range. The figure in the middle shows a plot with the number of the upper bin included in a fit, on the x-axis and the χ^2/NDF-value from the fit on the y-axis. The lower histogram shows the histogram for the range in which the fit could be deemed valid from the middle figure.

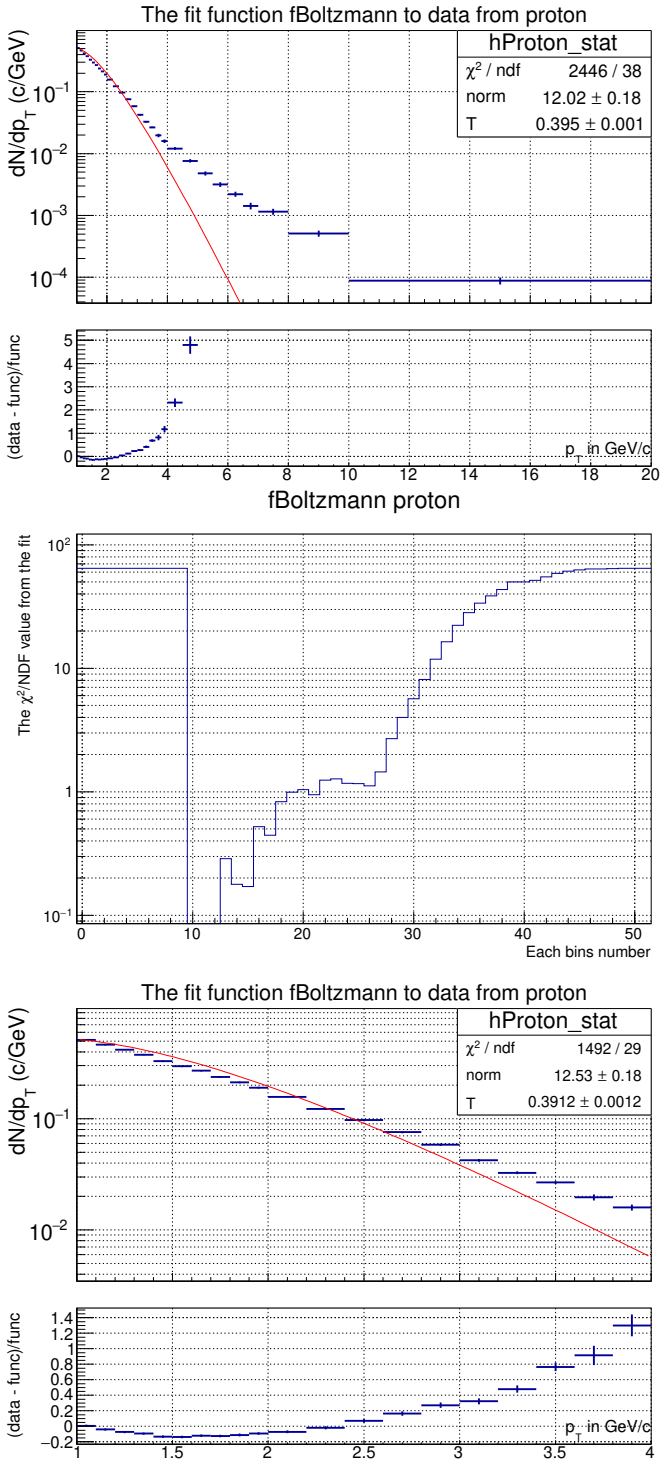

Figure 49: The upper histogram with its fit shows the spectra for the full range. The figure in the middle shows a plot with the number of the upper bin included in a fit, on the x-axis and the χ^2/NDF-value from the fit on the y-axis. The lower histogram shows the histogram for the range in which the fit could be deemed valid from the middle figure.

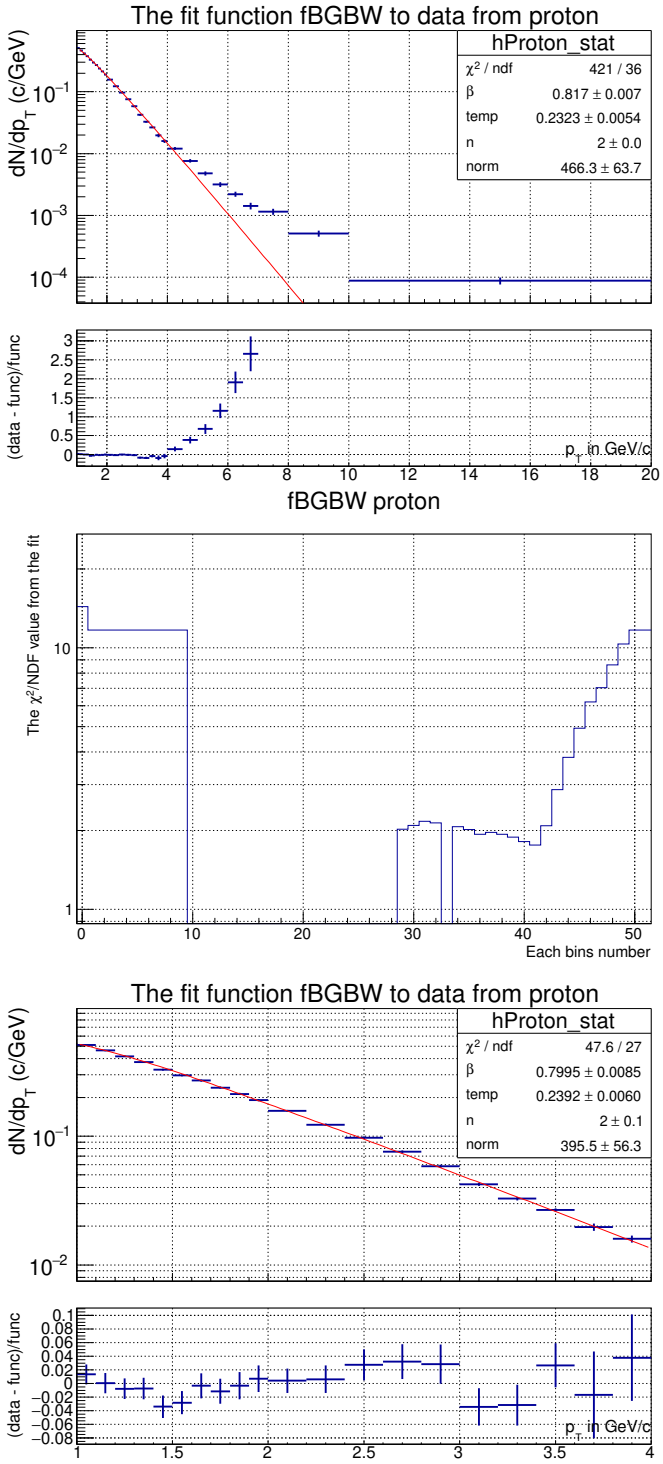

Figure 50: The upper histogram with its fit shows the spectra for the full range. The figure in the middle shows a plot with the number of the upper bin included in a fit, on the x-axis and the χ^2/NDF-value from the fit on the y-axis. The lower histogram shows the histogram for the range in which the fit could be deemed valid from the middle figure.

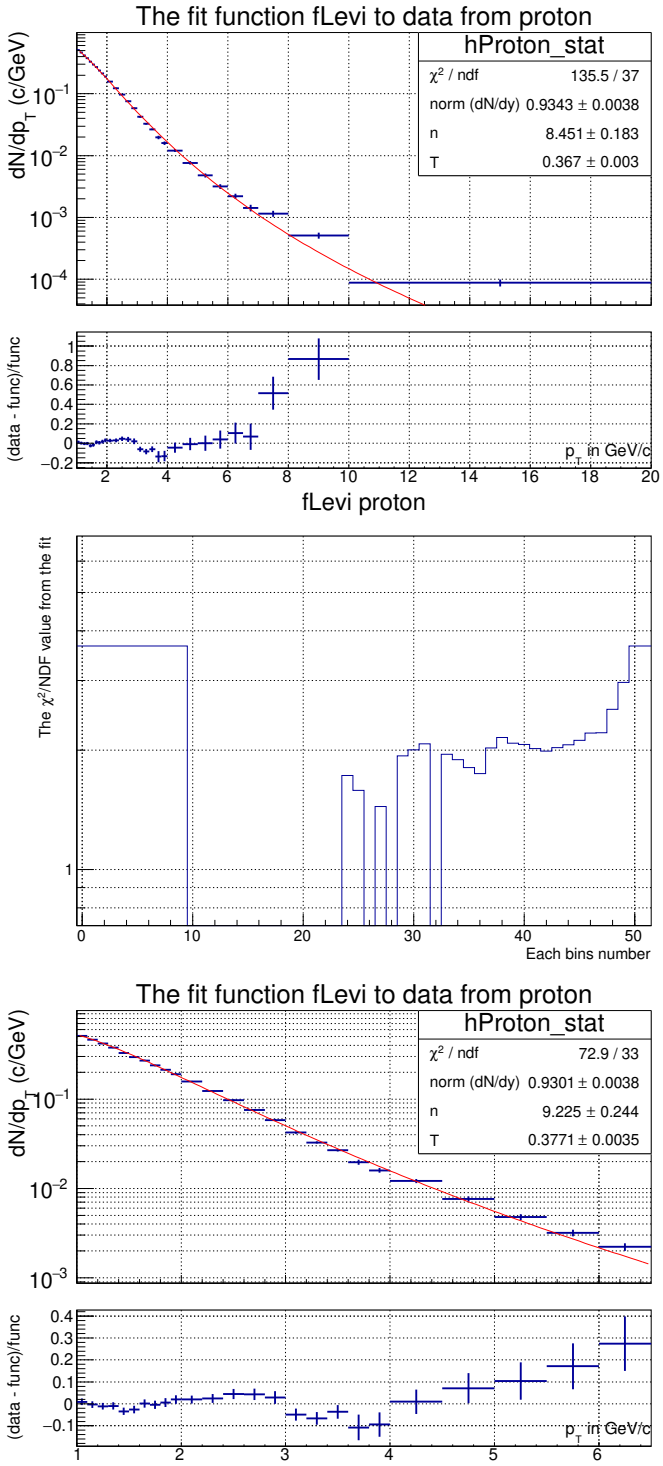

Figure 51: The upper histogram with its fit shows the spectra for the full range. The figure in the middle shows a plot with the number of the upper bin included in a fit, on the x-axis and the χ^2/NDF-value from the fit on the y-axis. The lower histogram shows the histogram for the range in which the fit could be deemed valid from the middle figure.

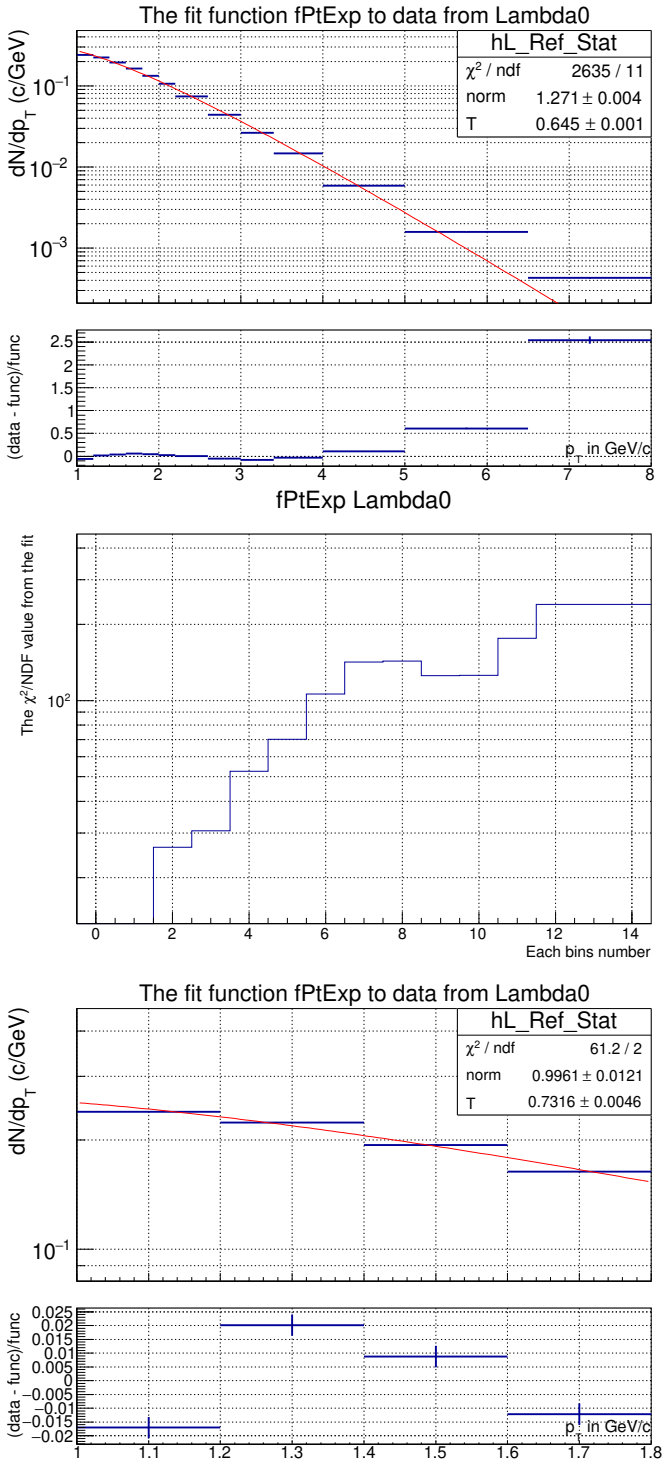

Figure 52: The upper histogram with its fit shows the spectra for the full range. The figure in the middle shows a plot with the number of the upper bin included in a fit, on the x-axis and the χ^2/NDF-value from the fit on the y-axis. The lower histogram shows the histogram for the range in which the fit could be deemed valid from the middle figure.

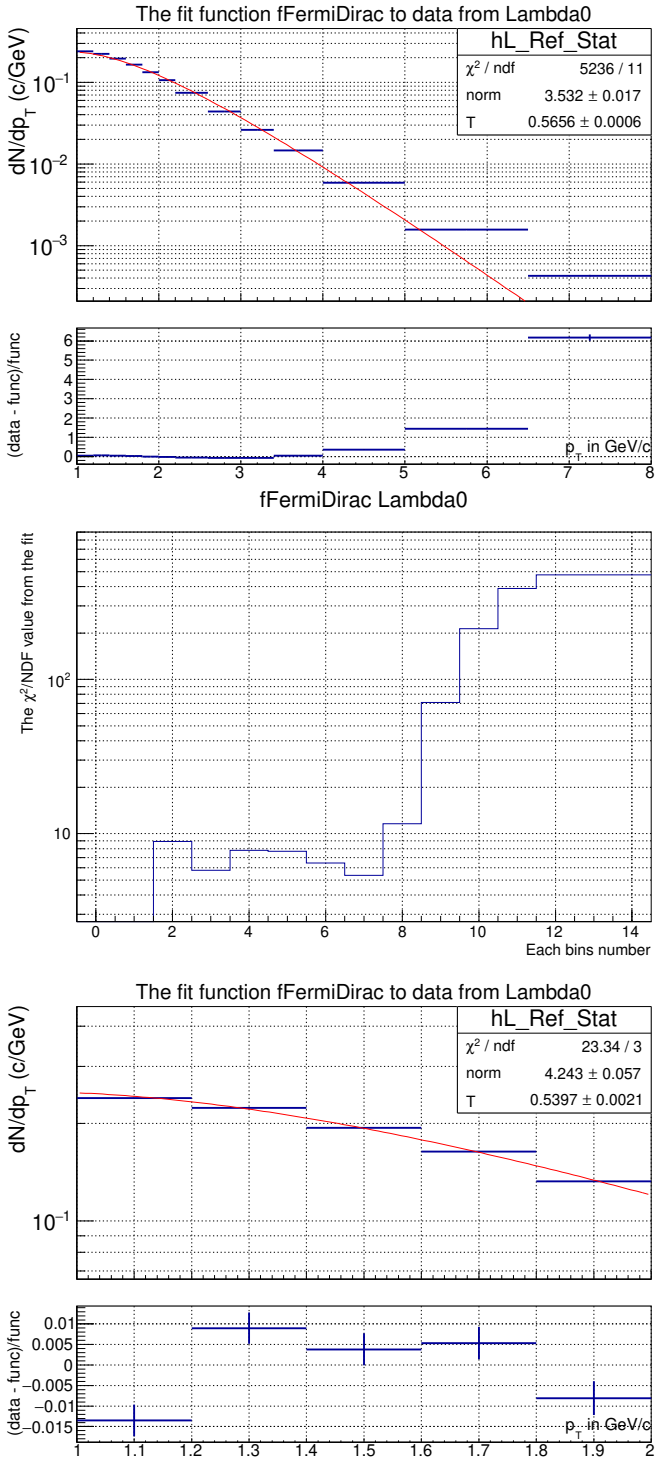

Figure 53: The upper histogram with its fit shows the spectra for the full range. The figure in the middle shows a plot with the number of the upper bin included in a fit, on the x-axis and the χ^2/NDF-value from the fit on the y-axis. The lower histogram shows the histogram for the range in which the fit could be deemed valid from the middle figure.

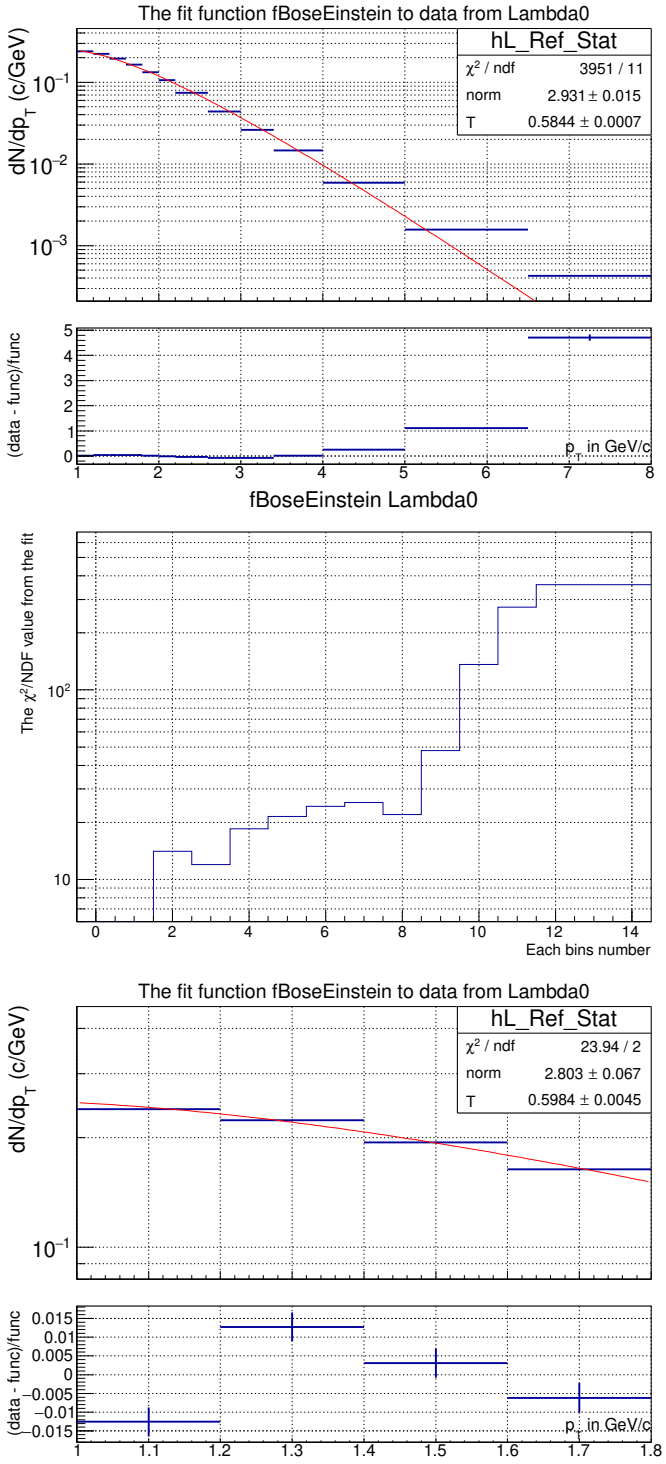

Figure 54: The upper histogram with its fit shows the spectra for the full range. The figure in the middle shows a plot with the number of the upper bin included in a fit, on the x-axis and the χ^2/NDF-value from the fit on the y-axis. The lower histogram shows the histogram for the range in which the fit could be deemed valid from the middle figure.

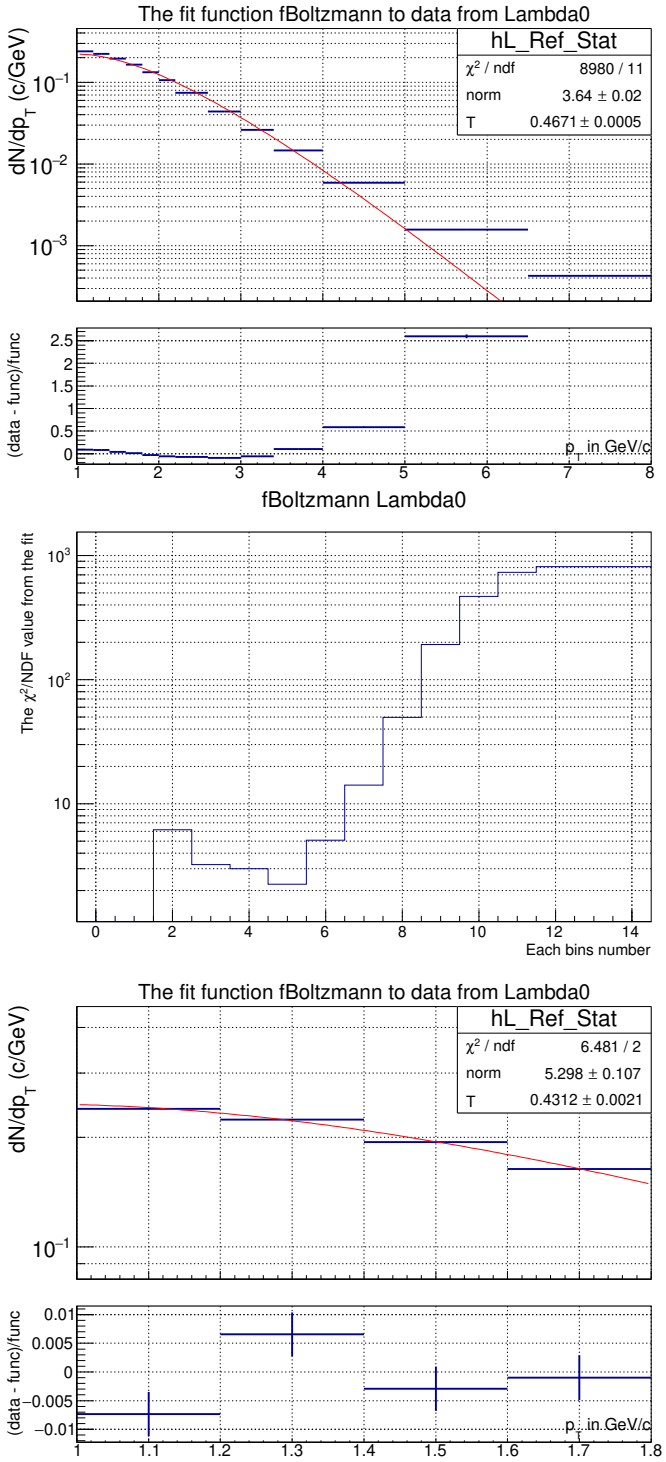

Figure 55: The upper histogram with its fit shows the spectra for the full range. The figure in the middle shows a plot with the number of the upper bin included in a fit, on the x-axis and the χ^2/NDF-value from the fit on the y-axis. The lower histogram shows the histogram for the range in which the fit could be deemed valid from the middle figure.

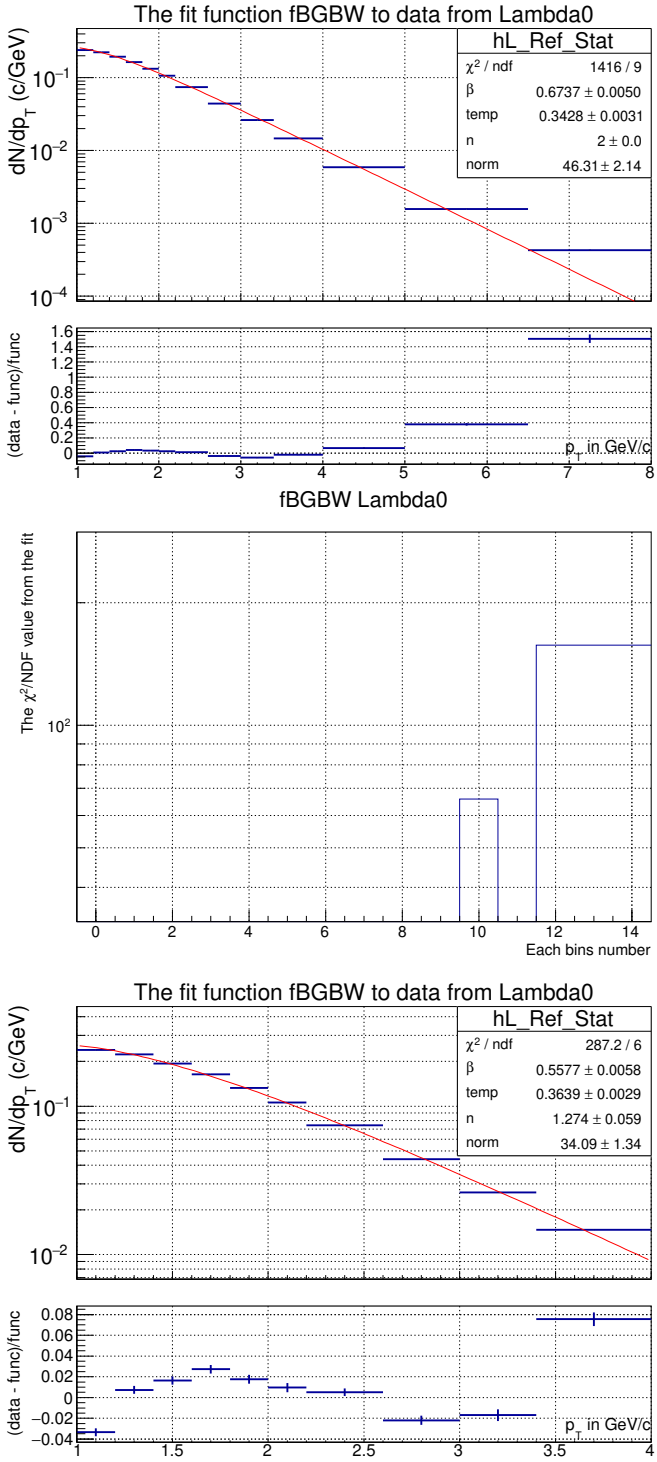

Figure 56: The upper histogram with its fit shows the spectra for the full range. The figure in the middle shows a plot with the number of the upper bin included in a fit, on the x-axis and the χ^2/NDF-value from the fit on the y-axis. The lower histogram shows the histogram for the range in which the fit could be deemed valid from the middle figure.

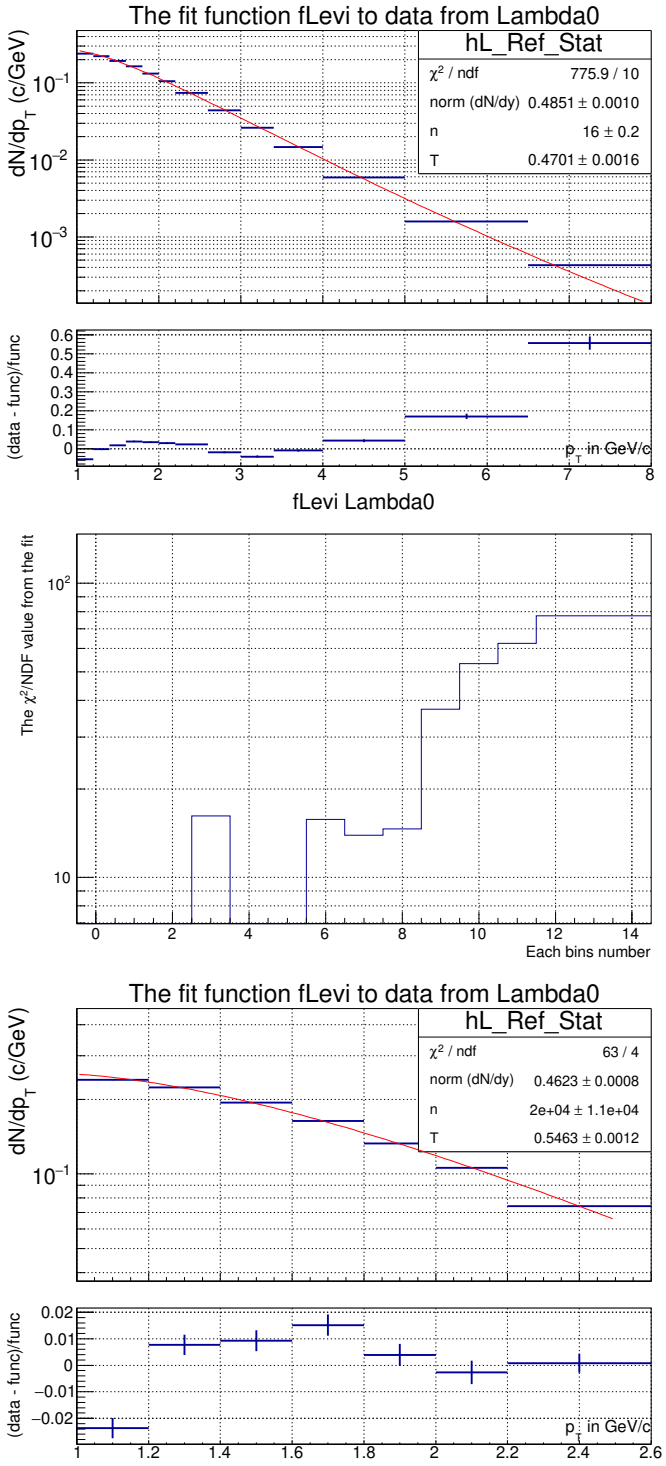

Figure 57: The upper histogram with its fit shows the spectra for the full range. The figure in the middle shows a plot with the number of the upper bin included in a fit, on the x-axis and the χ^2/NDF-value from the fit on the y-axis. The lower histogram shows the histogram for the range in which the fit could be deemed valid from the middle figure.

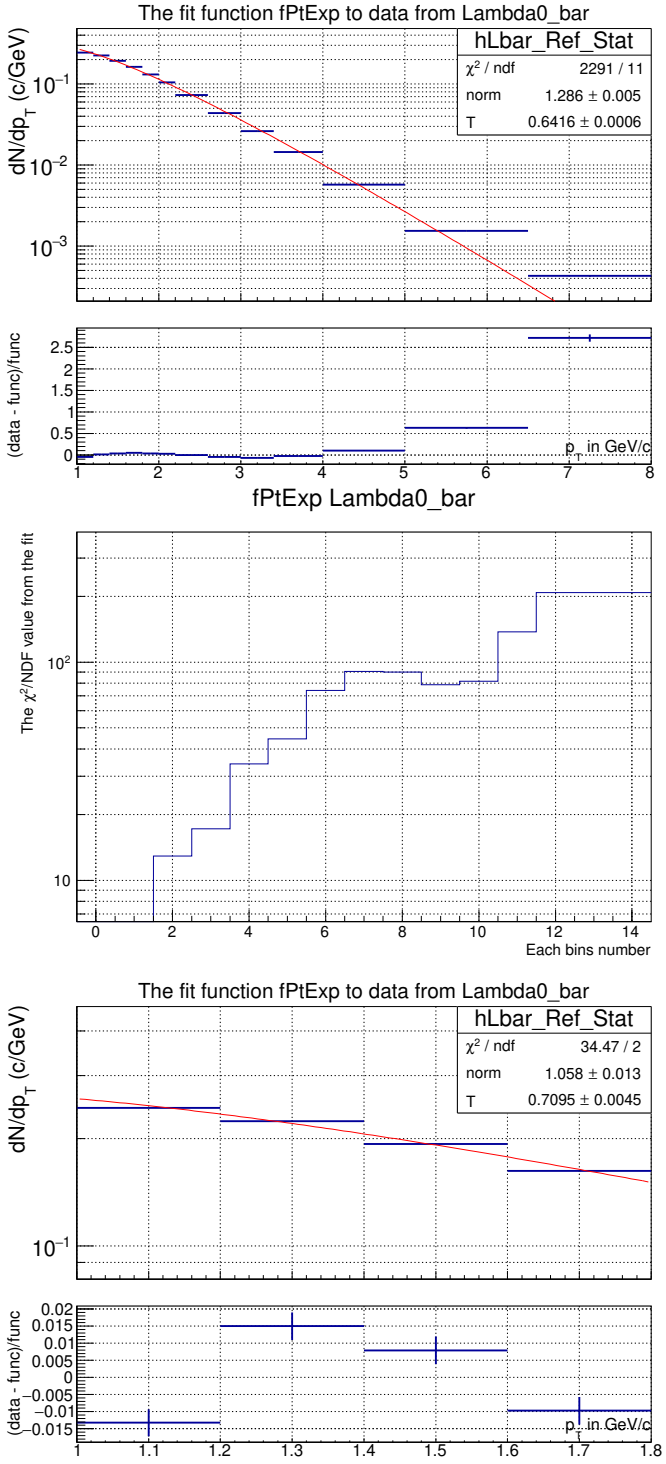

Figure 58: The upper histogram with its fit shows the spectra for the full range. The figure in the middle shows a plot with the number of the upper bin included in a fit, on the x-axis and the χ^2/NDF-value from the fit on the y-axis. The lower histogram shows the histogram for the range in which the fit could be deemed valid from the middle figure.

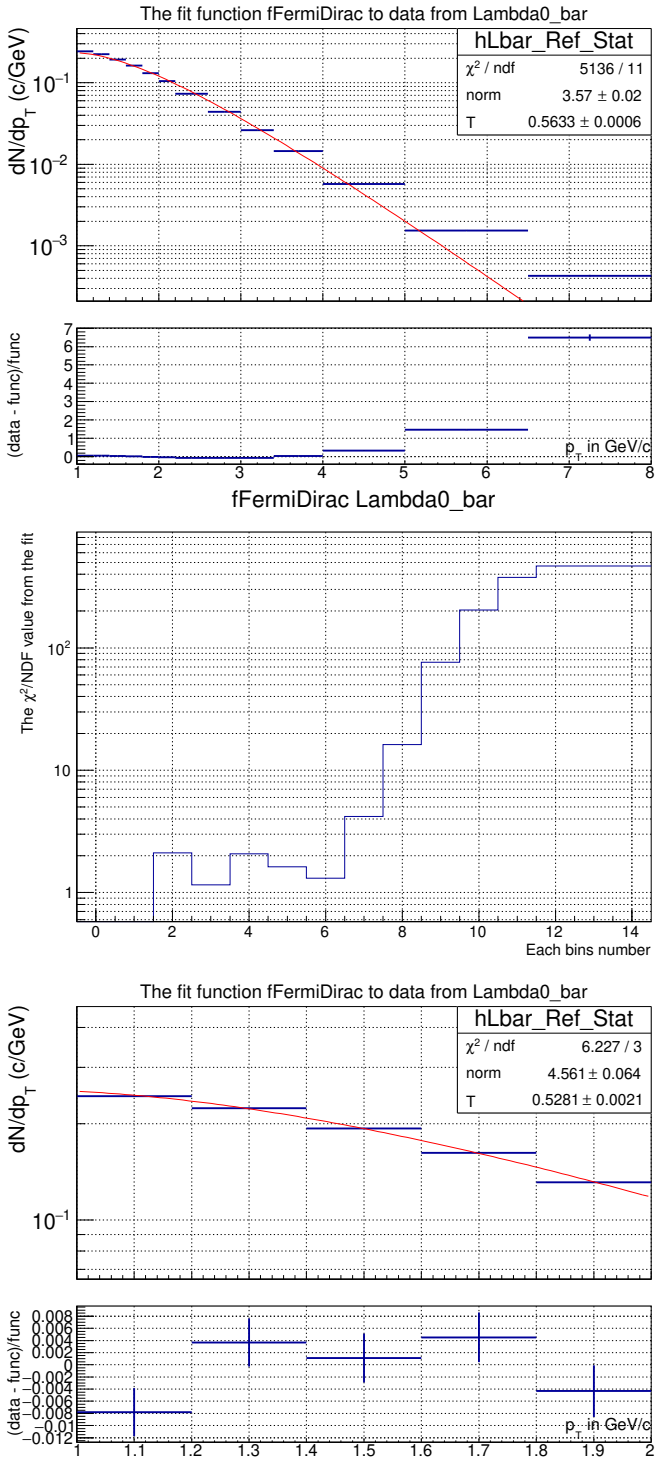

Figure 59: The upper histogram with its fit shows the spectra for the full range. The figure in the middle shows a plot with the number of the upper bin included in a fit, on the x-axis and the χ^2/NDF-value from the fit on the y-axis. The lower histogram shows the histogram for the range in which the fit could be deemed valid from the middle figure.

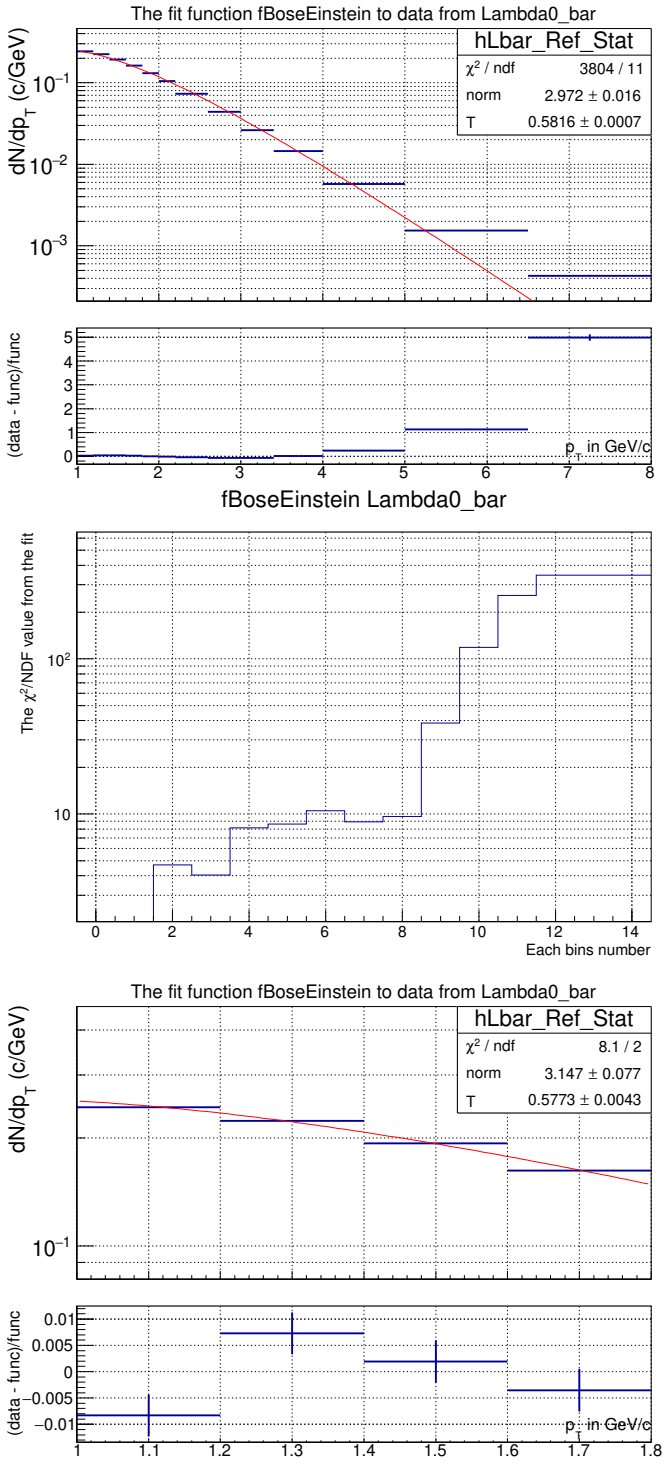

Figure 60: The upper histogram with its fit shows the spectra for the full range. The figure in the middle shows a plot with the number of the upper bin included in a fit, on the x-axis and the χ^2/NDF-value from the fit on the y-axis. The lower histogram shows the histogram for the range in which the fit could be deemed valid from the middle figure.

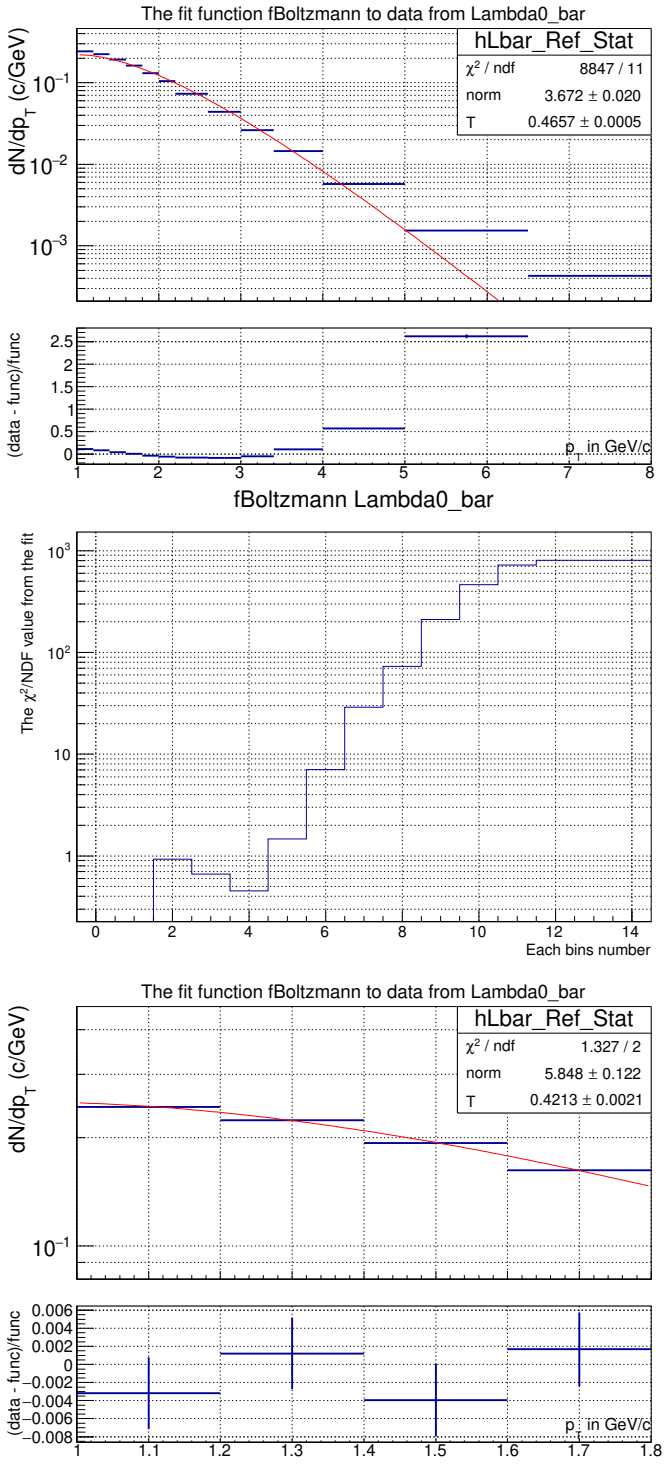

Figure 61: The upper histogram with its fit shows the spectra for the full range. The figure in the middle shows a plot with the number of the upper bin included in a fit, on the x-axis and the χ^2/NDF-value from the fit on the y-axis. The lower histogram shows the histogram for the range in which the fit could be deemed valid from the middle figure.

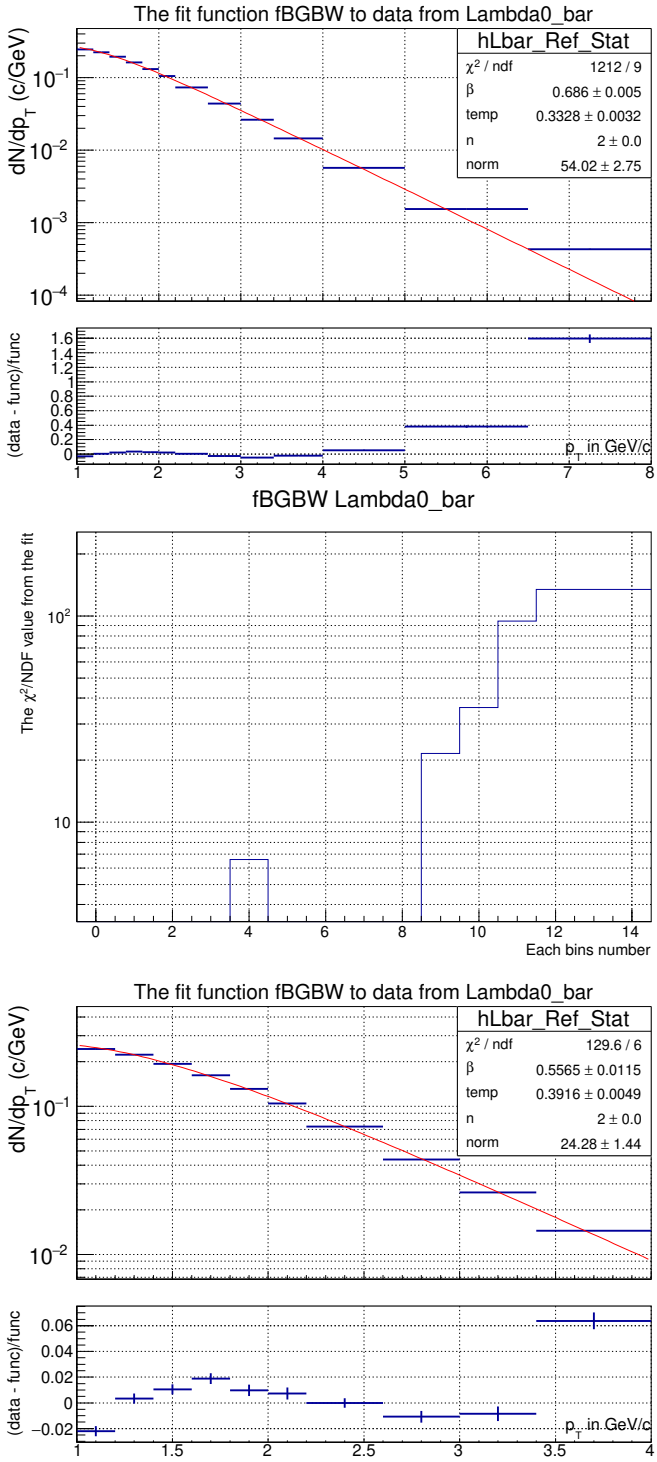

Figure 62: The upper histogram with its fit shows the spectra for the full range. The figure in the middle shows a plot with the number of the upper bin included in a fit, on the x-axis and the χ^2/NDF-value from the fit on the y-axis. The lower histogram shows the histogram for the range in which the fit could be deemed valid from the middle figure.

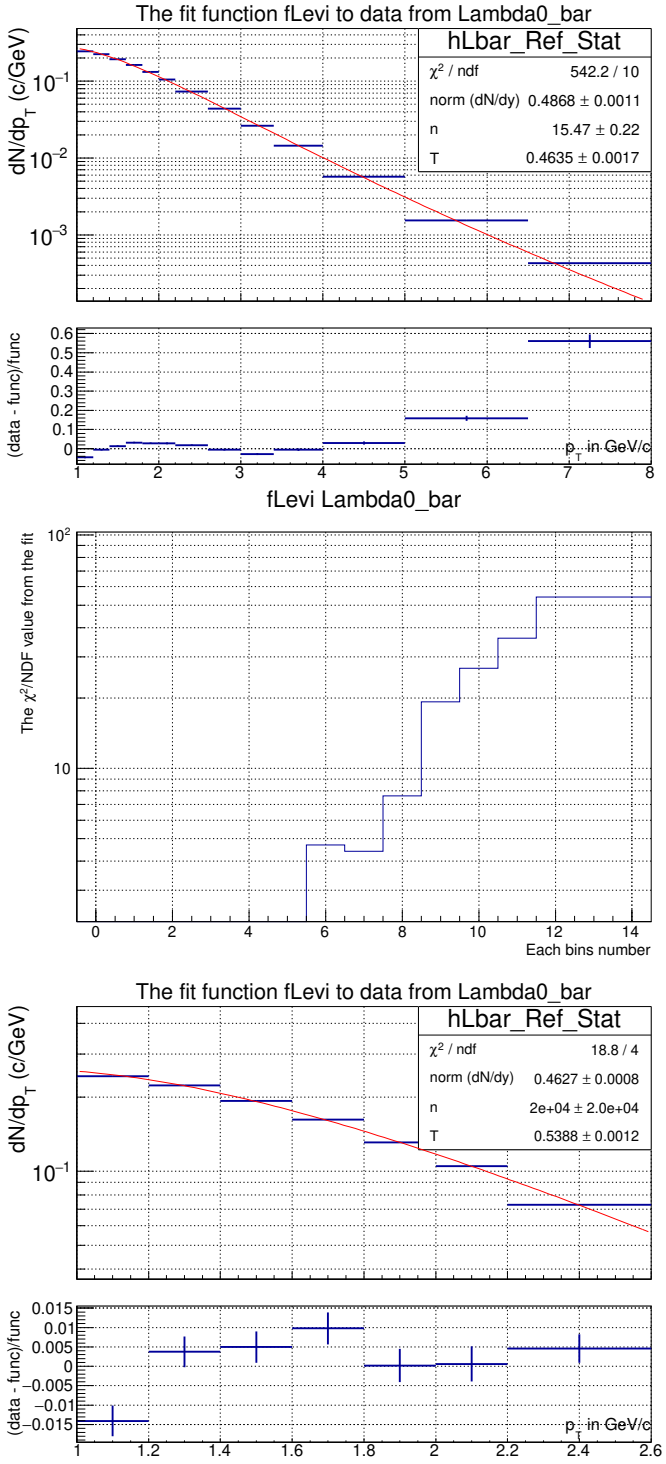

Figure 63: The upper histogram with its fit shows the spectra for the full range. The figure in the middle shows a plot with the number of the upper bin included in a fit, on the x-axis and the χ^2/NDF-value from the fit on the y-axis. The lower histogram shows the histogram for the range in which the fit could be deemed valid from the middle figure.